

**Fabrication and Testing of Inkjet Printed Electrodes for Anion Exchange
Membrane Water Electrolysis**

by

Scott Storbakken

A thesis submitted in partial fulfillment of the requirements for the degree of

Master of Science

Department of Mechanical Engineering

University of Alberta

©Scott Storbakken, 2022

Abstract

To study the relatively novel technology of anion exchange membrane (AEM) water electrolysis in a scientific manner, a controllable and repeatable electrode fabrication method is needed. While inkjet printing has been successfully used to fabricate electrodes for proton exchange membrane (PEM) water electrolyzers, it has not been used for fabricating AEM-based water electrolyzer electrodes. The drop-on-demand nature of inkjet printing allows for the precise control of the electrode fabrication process such that the electrode loadings may be precisely controlled. This work investigates the suitability of the inkjet printing method for fabricating electrodes for AEM-based water electrolysis.

Catalyst inks based upon Pt|C and IrO_x were developed containing a commercially available anion conducting ionomer. The suitability of the catalyst inks for use with the inkjet printing method was analyzed using dynamic light scattering (DLS) and glass kinematic viscometers. The consistency of the inks, as determined from DLS, was improved by decreasing the wt.% of the ionomer solution used to produce the inks, and by adding a viscosity increasing additive (propylene glycol) to the catalyst ink slurry after the addition of the ionomer.

The developed catalyst inks were successfully used to produce and test AEM-based water electrolyzers with catalyst coated membrane (CCM) and catalyst coated substrate (CCS) cell architectures. While the loading normalized performance for the cells was found to be similar to those from literature at low operational currents, it was notably poorer at elevated currents. Using electrochemical impedance spectrometry (EIS) it was found that the cell resistances were similar to or even lower than

those from literature. The lower cell performance was therefore hypothesized to be due to the relatively high anodic ionomer content used (15 wt.% compared to 7 wt.% used in literature). While it was found that the inkjet printing method is suitable for producing electrodes for AEM-based water electrolysis, further testing is required with anion conducting materials (membrane and ionomer) that are less prone to dimensional swelling due to water uptake to obtain cell-to-cell repeatability.

Keywords: anion exchange membrane water electrolysis, electrode fabrication, inkjet printing, dynamic light scattering, catalyst coated membrane, catalyst coated substrate, glass kinematic viscometer

Acknowledgements

First and foremost, I would like to thank my supervisor Dr. Marc Secanell for his unwavering personal, professional, and financial support during my Master's degree—without which, this work would have truly been impossible. To my colleagues in the Energy System Design Laboratory, thank you for the many work and non-work related conversations—they helped me through the tough times and made the good times all the more enjoyable.

To my Mother and Father, it can not be said enough times, in enough ways, or loud enough, but thank you both for all of your loving support—it means the world to me and I am incredibly privileged to have you both as parents.

I would like to specifically thank the following members of the Energy System Design Laboratory: To Manas, I like to think that we were able to learn from one-another over the years, but truthfully, our relationship was far more commensal than it was mutual—thank you for answering my *many* questions. Thank you Manas as well for providing me the PEM-based CCMs that I used to validate my test-station setup. To Michael and Aslan, although I'd come to each of you for help on different topics, you would both drop whatever you were doing to assist me—perhaps I wasn't very good at offering a choice on that front, but thank you nonetheless. To Luis, I fear that at times I forgot that you had your own work to do and that you are not only a procurement specialist—thank you for helping me get all the materials I needed to conduct my research.

Lastly, I would like to thank everyone who supported me in a personal way during my degree. There are too many of you to name, and I do not want to risk leaving someone out, but if our paths crossed during this period of my life, either for a long while or a short while, thank you, thank you, *thank you*.

Table of Contents

1	Introduction	1
1.1	Background and Motivation	1
1.2	AEM Electrolyzer Cell Structure, Operation, and Performance	5
1.3	Literature Review	9
1.3.1	AEM Water Electrolyzer Components	9
1.3.2	AEM Electrolyzer Assembly and Fabrication Methods	22
1.3.3	AEM Electrolyzer Operation	26
1.4	Objectives	30
2	Catalyst Ink Development and Characterization	31
2.1	Methodologies for Characterizing Catalyst Inks	32
2.1.1	Viscosity Measurements	32
2.1.2	Density Measurements	35
2.1.3	Particle Size Measurements	37
2.1.4	Refractive Indices of Solvent Solutions	42
2.2	Results and Discussion for Catalyst Ink Development	44
2.2.1	Aemion-Based Pt C Catalyst Ink	46
2.2.2	Aemion-Based IrO _x Catalyst Ink	53
2.2.3	Summary of Developed Catalyst Inks	59
3	Electrode Fabrication and Electrolyzer Testing	61
3.1	Methodologies for Electrode Fabrication and Electrolyzer Testing	61
3.1.1	Electrolyzer Test-Station Hardware	61
3.1.2	Electrolyzer Test-Station Software	64
3.1.3	Catalyst Coated Membrane Fabrication	66
3.1.4	Electrolyzer Cell Assembly	69
3.1.5	Polarization Curves and Stability Testing	73
3.1.6	Electrochemical Impedance Spectrometry	74
3.2	Results and Discussion for Electrode Fabrication and Cell Testing	76

3.2.1	Electrode Fabrication	76
3.2.2	Validation of Test-Station Equipment & Cell Hardware	82
3.2.3	Repeatability of CCM Cell Performance	94
3.2.4	Proof-of-Concept CCM & CSS Cell Performance	95
3.2.5	Comparison of Cell Performance to Literature	97
3.2.6	Cell Stability	101
4	Conclusions & Future Work	105
4.1	Conclusions	105
4.2	Future Work	107
	References	108
A	Equipment Information	119
A.1	Temperature Control Box Design	119
A.2	Zeitfuchs Cross-Arm Calibration Documentation	120
A.3	Gas Disengagement Unit Design	121
A.4	Extended Parallel Channel Flow Field Bipolar Plate Drawings	124
B	Uncertainty Analysis	128
B.1	Viscometer Calibration	129
B.2	Solvent and Catalyst Ink Density	130
B.3	Litesizer 500 Bias Uncertainty Validation	133
B.4	Solvent and Catalyst Ink Viscosity	135
B.5	Test-Station Pump Flow Rate	135
C	Linear System of Equations for Calculating Catalyst Ink Recipes	138

List of Tables

1.1	Summary of companies providing commercially available AEMs and ionomers.	16
1.2	Performance data obtained by Fortin et al. for AEM electrolyzers using Aemion membranes of varying IECs and thicknesses using 1 mol/L KOH at 50°C [57].	20
1.3	Stability data obtained by Fortin et al. for AEM electrolyzers using Aemion membranes of varying IECs and thicknesses using 1 mol/L KOH at 50°C [57].	20
1.4	Summary of Aemion AP1-based catalyst inks used in literature.	25
1.5	Summary of variable temperature studies conducted with electrolyzers with commercially available AEMs.	27
1.6	Summary of studies performed on the different feed methods for an AEM-based electrolyzer.	28
1.7	Summary of conclusions for studies performed on the different feed methods for an AEM-based electrolyzer.	29
2.1	Summary of ink characterization results obtained for baseline Nafion-based Pt C catalyst ink.	45
2.2	Summary of density and viscosity data obtained for Aemion Pt C inks and solvent solutions. Each sample is unique, with the exception of Aemion CB Ink 0.1 which was tested at two temperatures. For the viscometer used, CF = Cannon-Fenske and ZC = Zeitfuchs Cross-arm.	52
2.3	Final Pt C and IrO _x catalyst ink recipes and their corresponding characteristics.	60
3.1	Cell materials used for assembling AEM-based electrolyzers.	71
3.2	Description of galvanostatic current densities used for performing a polarization curve experiment. Each step held for two minutes.	73
3.3	Primary parameters used for EIS experiments.	75

3.4	Summary of PEM-based CCM properties tested to validate the functionality of the AEM-based water electrolyzer test-station.	82
3.5	Summary of CCMs tested for comparing PTFE and Kapton polyimide gasket materials.	86
3.6	Summary of CCMs tested for comparing 6 mil and 7 mil gasket thicknesses.	87
3.7	Summary of PTL thicknesses and estimated porosities with 6 and 7 mil thick gaskets.	88
3.8	Comparative summary of AEM-based electrolyzers containing similar materials to the cells tested herein.	99
3.9	Comparison of HFR values for the cells from this work and those from literature.	101
A.1	Bill of materials for temperature control boxes used for AEM electrolyzer test-station.	119
A.2	Bill of materials for GDU corresponding to Figure A.2.	123
B.1	Data obtained for measuring the density of water at room temperature.	131
B.2	Physical data for CRM used to test bias uncertainty of Anton Paar Litesizer 500.	133
B.3	Experimental DLS results for CRM obtained from Anton Paar Litesizer 500.	134
C.1	Description of variables for a system of linear equations for converting generalized catalyst ink recipes based upon relative wt.%s to absolute gravimetric-based recipes.	138

List of Figures

1.1	Total global demand for hydrogen in both its pure and non-pure forms. Data sourced from Reference [2].	2
1.2	Structure and electrochemical operation of a single AEM electrolysis cell.	6
1.3	Schematic of a water electrolyzer polarization curve depicting the effect of various voltage loss mechanisms.	8
1.4	Comparison of in-situ cell performance (tested with loadings of 3 mg/cm ² and pure water cell feed), activation overpotentials (tested in 1 mol/L KOH with loadings of 10 µg/cm ²), and electronic conductivities for different OER electrocatalysts. Data sourced from Xu et al. [32]. . .	12
1.5	Schematic of experimental setup (740 Membrane Test System with Pt electrodes by Scribner Associates Inc. [39]) used by Ziv and Dekel to determine the true hydroxide conductivity of an AEM [38]. R.H. = relative humidity.	15
1.6	Polarization curves for AEM cells utilizing various AEMs available commercially from Tokuyama Corporation (A-201), Dioxide Materials (Sustainion), FuMA-Tech (Fumapem FAA-3), and Ionomr Innovations (Aemion).	17
2.1	Annotated image of setup containing a glass capillary viscometer used to determine experimental kinematic viscosity values of catalyst inks.	33
2.2	Sample input parameters set for the Kalliope software when performing a DLS particle size series test with the Anton Paar Litesizer 500. . . .	42
2.3	Simplified optical setup of the Anton Paar Litesizer 500 (adapted from [87]).	43
2.4	Intensity-weighted particle size distributions obtained from DLS for baseline Nafion-based Pt C catalyst ink. Note that R1 through R10 refers to repetition one through ten, respectively, in the chronological order tests were conducted.	45

2.5	Intensity-weighted particle size distributions obtained from DLS for Aemion Pt C Ink 0.1. The viscosities for the ink solvent solutions without solid-content were obtained using the Cannon-Fenske viscometer.	47
2.6	Intensity-weighted particle size distributions obtained from DLS for Aemion CB Ink 0.1. Viscosities for ink samples with solid-content obtained using Zeitfuchs Cross-Arm viscometer.	49
2.7	Intensity-weighted particle size distributions obtained from DLS for Aemion Pt C Ink 0.2. DLS test performed with a viscosity of 2.17 ± 0.04 mPa·s for the ink solvent solution without solid content.	50
2.8	Intensity-weighted particle size distributions obtained from DLS for Aemion Pt C Ink 0.3. Viscosities of ink samples with solid-content (ionomer only) obtained using Zeitfuchs Cross-Arm viscometer ($\eta = 9.47 \pm 0.15$ mPa·s).	51
2.9	Various DLS results obtained for Aemion IrO _x Ink 0.1 over a period of 452 hours. Data obtained using $\eta = 2.17$ mPa·s for a solvent solution containing a 3:1 wt.% ratio of water:methanol with 40 wt.% PG.	54
2.10	Comparison of intensity-weighted particle distributions of IrO _x and Aemion ionomer in a 3:1 wt.% ratio of methanol:water ($\eta = 0.995$ mPa·s used for both tests).	55
2.11	Comparison of DLS results obtained for Aemion AP1-HNN8 ionomer solutions with varying solid content.	56
2.12	Intensity-weighted particle size distributions obtained from DLS for Aemion IrO _x Ink 0.2. DLS test performed with a viscosity of 2.17 ± 0.04 mPa·s for the ink solvent solution without solid content.	57
2.13	Intensity-weighted particle size distributions for Aemion IrO _x Ink 0.3 ($\eta = 9.47$ mPa·s used for both tests).	59
3.1	Test-station developed for conducting experiments with AEM-based electrolyzers. GDU = gas disengagement unit used for two-phase gas-liquid separation.	63
3.2	Flow diagram illustrating how the test-station software performs an experiment. Note that the softwares main GUI thread runs simultaneously as the process above but is not pictured.	65
3.3	Equipment used for inkjet printing CCMs.	66
3.4	Exploded schematic illustrating how AEMs were held flat during the conversion process. Note that the lid contained built in clips that clamped it to the base (not shown in schematic).	68

3.5	Schematic of a single CCM with an oversized cathode.	69
3.6	Exploded schematics illustrating the assembly of AEM-based electrolyzer.	70
3.7	Cross-sectional schematic of gasketed MEA demonstrating the concept of pinch. Note that the pinch calculation, as per Eq. (3.2), does not include the membrane thickness since the membrane is present in both calculated thicknesses.	72
3.8	Pressure film measurement demonstrating proper compression of the MEA and sealant of the cell.	73
3.9	Equivalent circuit used for interpreting Nyquist plots obtained from EIS [7].	76
3.10	Images of a sample CCM produced using inkjet printing. Membrane = Aemion AF1-HNN8-50.	77
3.11	Comparison of cathodes fabricated using Aemion AF1-HNN8 and Nafion ionomers. The Nafion-based electrode was produced using Pt C Ink 0.3 with Nafion ionomer in place of Aemion AF1-HNN8 (15 wt.% ionomer within the solid-phase of the ink). Both electrodes were printed onto Aemion AF1-HNN8-50 membrane.	78
3.12	Microscopy images demonstrating the difference between a cathode contacted by the printer head and a regular electrode from the same CCM batch.	78
3.13	Microscopy images demonstrating the difference between a partially reacted CCM and a regular electrode from the same CCM batch.	79
3.14	Microscopy images of holes formed during anode fabrication for three separate CCMs from a single batch.	79
3.15	Images of a sample CCM produced using inkjet printing. Membrane = Aemion AF2-HNN8-50.	81
3.16	Polarization curves obtained for a PEM-based water electrolysis cell using an existing test-station setup used in Ref. [33] and the test-station developed for this work. Cell was operated at 80°C with deionized water fed to the anode at 8.4 ml/min (AEM Test-Station) or 12.6 mL/min (PEM Test-Station).	83
3.17	Demonstration of steady state operation at each galvanostatic step used to produce a polarization curve for a sample AEM-based water electrolyzer. Further details for the tested cell provided in Table 3.5 as ‘FAA-3 CCM’.	85

3.18	Polarization curves comparing cells assembled with Kapton polyimide and PTFE gaskets (7 mil thickness per electrode). Cells operated at 60°C with 0.85 mol/L KOH fed to both electrodes.	86
3.19	Polarization curves and Nyquist plots for Aemion-based cells assembled with 6 and 7 mil thick gaskets (per electrode). EIS data for Nyquist plots obtained at 20 mA/cm ²	88
3.20	Nyquist plots for CCMs produced using Fumapem FAA-3 and Aemion AF1-HNN8-50 membranes. EIS data obtained at 20 mA/cm ²	90
3.21	Image demonstrating a CCM swelled out-of-plane following conversion to hydroxide form and rinsed with deionized water.	91
3.22	Images of different flow patterns used for cell testing. The graphite plates shown were used for the cathode and respectively complimented by titanium plates with the same flow pattern for the anode.	92
3.23	Polarization curves and Nyquist plots (EIS obtained at 20 mA/cm ²) for Aemion-based cells assembled with extended parallel and serpentine channel flow patterns. Cells operated at 60°C with 0.85 mol/L KOH fed to both electrodes.	93
3.24	Polarization curves and Nyquist plots (EIS obtained at 20 mA/cm ²) for CCM-based cells with similar performances. Unless stated otherwise, all cell electrodes (anode & cathode) contained 15 wt.% ionomer (AP1-HNN8 ionomer). Cells operated at 60°C with 0.85 mol/L KOH fed to both electrodes.	95
3.25	Polarization curves and Nyquist plots for proof-of-concept CCM- and CCS-based Aemion AF1-HNN8-50 cells. Cells operated at 60°C with 0.85 mol/L KOH fed to both electrodes. Note that the EIS data for the CCM-based cell is not provided due to issues with the cell sealing.	97
3.26	Polarization curves comparing the best proof-of-concept results obtained herein to those from literature using similar materials and operating conditions. For a complete comparison of the materials and operating conditions refer to Table 3.8.	100
3.27	Current densities obtained during potentiostatic testing for select Aemion-based cells. EIS performed every 60 minutes for the CCS-based cell and every 30 minutes for the CCM-based cell.	102
3.28	Nyquist impedance plots for CCM- and CCS-based cells during two hours of potentiostatic stability testing. EIS data obtained at 20 mA/cm ²	103
3.29	Microscopy images of an Aemion AF1-HNN8-50 CCM before and after water electrolysis operation.	104

4.1	Comparison of AEM-based electrolyzer current densities achieved at 1.8 V. Data for distributions obtained from Miller et al. [28] with 30 citations for CCS data and 17 for CCM data. Distribution values do not incorporate data from Fortin et al. [57], Koch et al. [59], or the results obtained from this work.	106
A.1	General schematic of PID temperature control box. Based upon the temperature obtained from the thermocouple, the PID triggers the heater on or off via the solid-state relay.	120
A.2	Isometric exploded view of GDU design used for AEM electrolyzer test station. Component numbers correspond to bill of materials in Table A.2. All solidmodel components obtained from McMaster-Carr with the exception of the thermocouple and HDPE plastic jar obtained from Refs. [121, 122], respectively.	122
B.1	Experimentally determined relationship between peristaltic pump head speed and resulting flow rate for AEM-based electrolyzer test-station. Results obtained for a single pump stream.	136

Chapter 1

Introduction

1.1 Background and Motivation

As stated by John Rigden in his book on the hydrogen element, a world without hydrogen would be a world without water, a world without carbohydrates, a world without proteins—and ultimately, a world without life. In fact, it is the 600 million tonnes of hydrogen fused into helium releasing energy every second in the sun that provides the heat required for life on Earth [1]. For comparison, the current demand for pure hydrogen on Earth *per year* is approximately 70 million tonnes [2]. As seen in Figure 1.1, the primary uses for pure hydrogen are for the production of ammonia via the Haber-Bosch process, and thereby fertilizers used to produce food for the World’s ever growing population¹, and for oil and gas refining². Although the current demand is only roughly half that of pure hydrogen, mixtures containing hydrogen gas are also required in an increasing amount for producing methanol and for the direct reduction of iron (DRI). In the case of the latter, the use of hydrogen presents an opportunity for which the CO₂ emissions associated with the production of steel may be greatly reduced [5]. Such reductions are required if global CO₂ emissions are to reach net zero by 2050 as required to limit global warming to 1.5°C above pre-industrial levels [6].

The potential for hydrogen to reduce emissions, however, is far greater than that associated with reduced greenhouse gas emissions from DRI alone. Beyond the current uses of hydrogen presented in Figure 1.1, hydrogen may be used as an energy carrier in sectors such as transportation, building heating, and power generation. For transportation, hydrogen used in fuel cell electric vehicles (FCEVs) offers potentially

¹The current production of ammonia is greater than 160 million tonnes per year (using more than 31 million tonnes of hydrogen per year [2]) and it has been estimated that only half of today’s agricultural production would be possible without the Haber-Bosch process [3].

²Hydrogen is used for both hydrotreatment, in which hydrogen is used to remove impurities (such as nitrogen, sulfur, and oxygen) from crude oil [4], and for hydrocracking, in which hydrogen is used to upgrade heavy residual oils into higher value oil products [2].

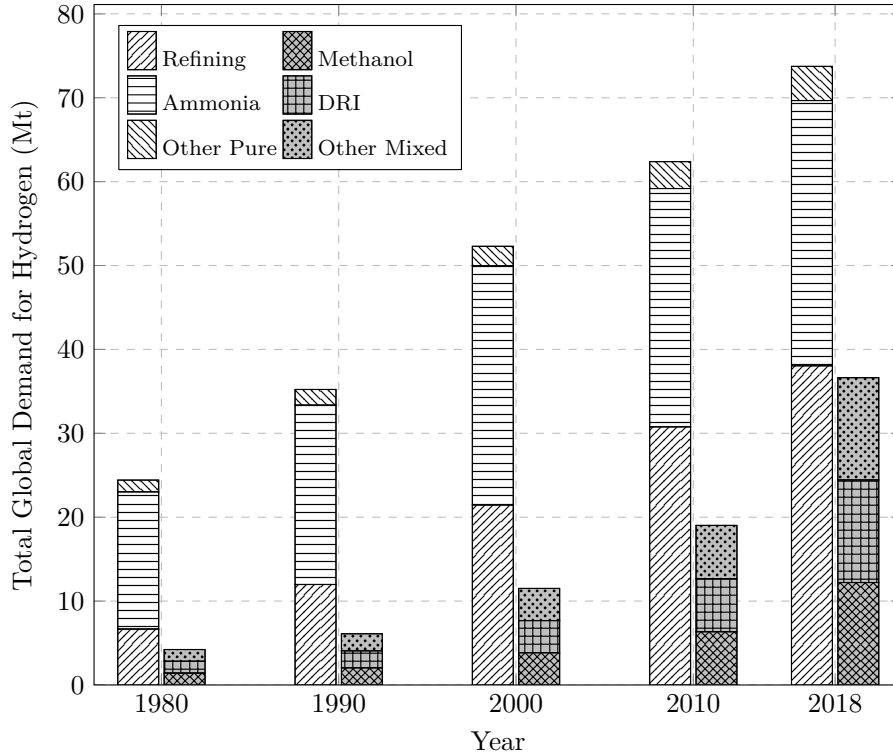


Figure 1.1 – Total global demand for hydrogen in both its pure and non-pure forms. Data sourced from Reference [2].

higher gravimetric power densities³ and faster refueling rates compared to battery electric vehicles (BEVs). Moreover, compared to internal combustion engines, hydrogen fuel cells offer higher efficiencies, silent operation, and virtually no undesirable emissions such as NO_x , SO_x , or particulate matter [7]. Heat generation currently accounts for a third of global energy-related CO_2 emissions, but may be reduced by utilizing hydrogen in fuel cell combined heat and power (CHP⁴) applications, direct flame combustion boilers, catalytic boilers, or gas-powered heat pumps [8]. Lastly, hydrogen may be used in power generation in a number of ways: co-firing of ammonia (produced from hydrogen) in coal power plants, blended into feedstock for gas turbines (although eventually used in its pure form), used in stationary fuel cells, or as a means for large-scale long-term energy storage [2, 9].

As promising as hydrogen is as an alternative energy carrier, its ability to reduce emissions is strongly linked to the method in which it is produced since it does not

³Fuel cells have a similar gravimetric power density as internal combustion engines, but have a lower volumetric power density compared to internal combustion engines and lithium-ion batteries owing primarily to the low volumetric energy density of hydrogen gas.

⁴Stationary CHP is currently the largest and most established market for fuel cells thanks strongly to high deployment in Japan [8].

naturally occur in its molecular form. Hydrogen in its molecular form may be produced in a number of ways, but the majority of hydrogen currently produced requires hydrocarbon feedstocks such as natural gas and coal [2]. As a result, roughly 2.5% of the World’s current CO₂ emissions directly come from the use of hydrocarbons for the production of hydrogen⁵. For reference, Canada’s current greenhouse gas emissions are equivalent to 2.2% of the World’s total CO₂ emissions [10, 11]. If current trends for the growth of chemical products such as ammonia and methanol are projected forward, then CO₂ emissions from the corresponding growth in hydrogen production would rise by around 20% between 2018 and 2030 [2]. This estimated growth in CO₂ emissions from hydrogen production does not include emissions linked to additional hydrogen demand from sectors such as transportation or steel production. It has been estimated, however, that CO₂ emissions from natural gas used for steam methane reforming (SMR) may be reduced by up to 90% if carbon capture, utilization, and storage is used [2]. Nonetheless, the long term utilization of hydrocarbons, such as natural gas and coal, for the production of hydrogen, may be limited by the fact that they are non-renewable resources.

An alternative production method for molecular hydrogen that need not depend upon non-renewable fossil fuels is water electrolysis. Water electrolysis is the process whereby water is split into hydrogen and oxygen within an electrochemical cell through the application of electrical energy [12]. Although less than 0.1% of the World’s dedicated hydrogen production currently comes from water electrolysis, it has been cited as the cleanest method to produce hydrogen if the electricity required comes from renewable energy sources such as solar or wind [2, 12].

Technologies for water electrolysis are commonly classified by the electrolyte that they utilize. This classification is often distinguished by the state of the electrolyte (liquid, solid polymer, or solid oxide), and by the pH of the electrolyte (alkaline or acidic) [13]. From a historical perspective, electrolyzers utilizing liquid alkaline electrolytes were commercialized industrially in the early 20th century for hydrogen to be used in the Haber-Bosch process. Such industrial facilities were primarily powered by low cost hydroelectricity in countries such as Norway and Canada, but have since primarily closed due to an inability to economically compete with cheaper production methods based upon fossil fuels [14]. Conventional alkaline electrolysis is characterized by having the anode and cathode electrodes immersed within a liquid alkaline electrolyte and separated by a porous diaphragm that is permeable to the hydroxide and water molecules, but prevents the produced hydrogen and oxygen bubbles from

⁵The production of hydrogen from hydrocarbons currently produces around 820 Mt of CO₂ per year [2] while the total World produces roughly 33 200 Mt per year [10].

mixing [14, 15]. The electrolyte utilized is typically aqueous potassium hydroxide (KOH) with a concentration ≥ 5.3 mol/L [16, 17]. The primary advantage of alkaline water electrolysis over similar technologies under acidic conditions is that materials for cell components, especially electrocatalysts [18], may be broadened to include earth-abundant materials [14].

In the 1960s a solid-state polymer electrolyte, known as Nafion, that is capable of conducting hydrogen ions, or simply protons, was invented by the DuPont de Nemours company. Owing strongly to its high ionic conductivity, Nafion is currently the most commonly used material for proton exchange membranes (PEMs) used in PEM-based water electrolysis [14, 19]. The advantages exhibited by PEM electrolyzers over existing alkaline technologies stem directly from Nafion's acidic nature, structural properties, and solid polymer state. Nafion being a thin solid-phase polymer allows for PEM-based electrolyzers to be constructed in a compact configuration that leads to elevated efficiencies at high current densities [14, 15]. Furthermore, the structure of Nafion allows for the conductivity of protons without the need for a liquid electrolyte. As such, PEM-based water electrolyzers are commonly operated with pure water and are considered safer than their conventional alkaline counterparts that must utilize a highly caustic liquid electrolyte [12]. PEM-based electrolyzers are also considered safer for the electrochemical compression of hydrogen thanks to the reduced hydrogen permeability in Nafion compared to materials used for the diaphragm in alkaline water electrolysis [20]. The reduced hydrogen permeability in Nafion means that the electrodes in PEM-based water electrolysis may be operated with a differential pressure such that the produced hydrogen is compressed and the oxygen is not [12, 14, 15]. Lastly, PEM-based water electrolyzers respond rapidly to the amount of power supplied, and operate over a large domain of partial loads [15].

The corrosive acidic environment present in PEM-based water electrolyzers, however, requires the use of distinct materials. The cell components, including the catalysts and bipolar plates, must resist the highly acidic environment ($\text{pH} \approx 2$) and high overpotentials (≈ 2 V with respect to the hydrogen reference electrode) [15]. Although there has been some progress in decreasing the cost of cell components such as the bipolar plates, the cost of catalysts is expected to become increasingly important as a completely non-noble metal-based catalyst has yet to be identified for PEM-based water electrolysis [21, 22].

An emerging technology that aims to combine the benefits of both PEM-based water electrolysis and conventional alkaline water electrolysis is anion exchange membrane (AEM) water electrolysis. The utilization of a solid-state polymer electrolyte capable of conducting anions (commonly hydroxide) results in a technology that op-

erates in an alkaline environment with a cell structure similar to that used in PEM-based electrolysis. Since AEM-based water electrolysis is conducted within an alkaline environment, it is possible to utilize catalysts used in conventional alkaline water electrolysis that are relatively abundant and cheaper compared to those utilized for PEM water electrolysis [22]. Moreover, since the cell structure utilized for AEM-based water electrolysis is similar to PEM-based water electrolysis, AEM electrolysis may be more efficient and considered safer than conventional alkaline electrolysis. That is, the compact cell design and electrodes may reduce inefficiencies regarding ion transport within the cell while simultaneously offering the ability to operate with a relatively low concentration of alkaline solution, or even distilled water [14, 23, 24]. Similarly, the cell structure and utilization of a membrane electrolyte allows AEM-based water electrolyzers to operate with a differential pressure between its electrodes, as is done in PEM-based water electrolysis [14, 25].

AEM-based water electrolysis, however, is a relatively new technology that has only been under investigation since circa 2010 [24, 26, 27], and as such, is only at the laboratory stage of development [23]. Thus, the commercial viability of AEM water electrolysis as a low-cost production method for green hydrogen is not yet realizable until further developments have been made. Recent review papers on the topic of AEM water electrolysis by Vincent et al. [23] and Miller et al. [28] indicate that the performance of the technology must be increased while concurrently keeping cost low by utilizing earth-abundant materials. In addition to increasing the performance, the stability of AEM-based water electrolyzers, especially when operating with pure water, must also be further investigated. Since aspects related to low-costs, high and stable performance, as well as operation with pure water, are often at odds with one-another (i.e., the utilization of expensive materials often increases performance and durability), continued research efforts are required for AEM water electrolysis.

1.2 AEM Electrolyzer Cell Structure, Operation, and Performance

Figure 1.2 illustrates the structure, as well as the electrochemical operation, of a single AEM-based electrolysis cell. Water introduced to the cathodic bipolar plate is transported through a flow field of channels to the porous transport layer (PTL). The PTL evenly distributes water, heat, and electrons to the cathode catalyst layer (CL) and simultaneously allows for the flow of produced hydrogen out of the cell. Within the cathode CL, electrons (e^-) and water (H_2O), in the presence of a catalyst, are reduced into hydrogen gas (H_2) and hydroxide ions (OH^-) via the hydrogen evolution

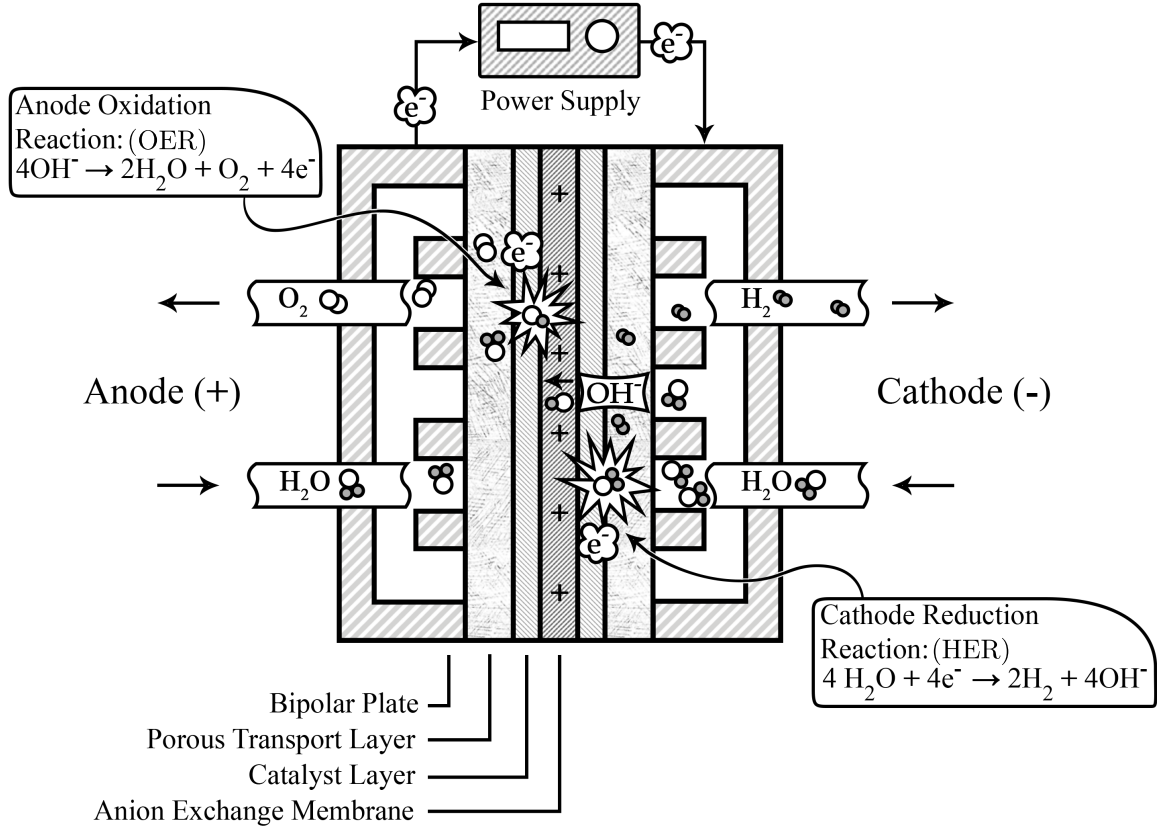


Figure 1.2 – Structure and electrochemical operation of a single AEM electrolysis cell.

reaction (HER). Hydroxide ions diffuse through ionomer or liquid within the CL and across the AEM to the anode CL where, in the presence of a catalyst, they form oxygen and water while releasing electrons in the oxygen evolution reaction (OER). The electrons then transfer through the anode PTL and into the bipolar plate where they are connected back to the external electronic circuit while the produced water either leaves the system with the oxygen or diffuses back to the cathode to react in the HER. Of note is that since water may diffuse through the AEM, water may be fed into both, or either, of the electrodes during operation.

Combining the cathode and anode half-cell reactions, respectively provided in Eqs. (1.1) and (1.2), yields the overall cell reaction provided in Eq. (1.3),



where the E^0 value is the standard-state reversible voltage⁶. Applying a current to the cell causes equilibrium to be lost such that the reversible voltage no longer applies. The performance of a water electrolyzer is often summarized in the form of a polarization curve in which the voltage of the cell is plotted against the current. The current plotted in a polarization curve is commonly normalized by the cell geometric area, and referred to as current density, so that cells of varying sizes may be directly compared. An ideal electrolyzer would maintain a constant voltage, referred to as the reversible cell voltage (E_{thermo}), for any amount of current. The reversible cell voltage is a thermodynamic value calculated using the Nernst equation that varies from the standard-state reversible voltage of 1.23 V depending upon the systems operational temperature and pressure, as well as the concentrations of the products and reactants. In practice, however, the cell voltage does not remain equal to the reversible cell voltage, and instead increases due to three non-thermodynamic sources of irreversibilities; namely, activation losses (η_{act}), ohmic losses (η_{ohmic}), and mass transport losses (η_{mass}). The actual voltage of the cell, or cell performance, at a given current density is the superposition of the reversible cell voltage and the three sources of irreversibilities,

$$V = E_{thermo} + \eta_{act} + \eta_{ohmic} + \eta_{mass}. \quad (1.4)$$

A sample polarization curve demonstrating the relationship presented in Eq. (1.4) is provided in Figure 1.3. Depending upon the current density domain, i.e., low, medium, or high, the overall cell performance is respectively dominated by the activation losses, ohmic losses, or mass transport losses.

Activation losses are due to reaction kinetics which are rooted in the mechanisms with which electron transfer occurs in an electrochemical reaction. An activation potential, or loss, is required to manipulate the reaction activation barrier such that a given electrochemical reaction proceeds in the oxidation or reduction direction. Since activation losses are associated with the electron transfer occurring at the interface between an electrode and electrolyte, there is in fact two distinct losses, one for the HER and one for the OER, that are superimposed to create the corresponding activation curve shown in Figure 1.3. The exponential relationship between the current density and activation losses is commonly described by the Butler-Volmer equation. The Butler-Volmer equation indicates that the activation losses may be reduced by increasing the availability of reactants, increasing the reaction temperature, utilizing different catalysts, or by altering the electrode fabrication method [7, 15].

⁶A standard-state reversible voltage is the voltage produced at thermodynamic equilibrium under standard conditions (298.15 K and atmospheric pressure) [7].

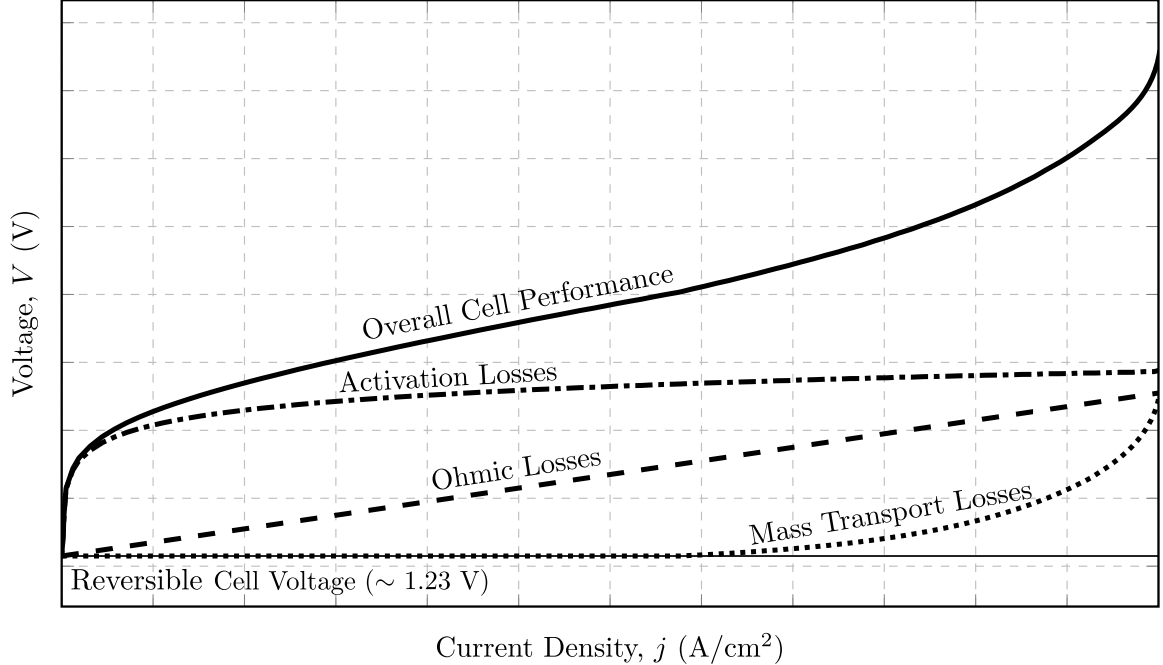


Figure 1.3 – Schematic of a water electrolyzer polarization curve depicting the effect of various voltage loss mechanisms.

Whereas activation losses stem from electron transfer within a given electrochemical half-cell reaction, ohmic losses stem from charge transport within the materials that make up the electrochemical system. As the name indicates, ohmic losses are governed by Ohm’s law,

$$\eta_{ohmic} = jR_{cell}, \quad (1.5)$$

where j is the operational current density and R_{cell} represents the cell’s total area specific resistance⁷. Although the cell resistance is comprised of both electronic and ionic resistances, it is often dominated by the ionic portion since the transport of ions tends to be inherently more complex than the transport of electrons⁸ [7]. Moreover, the ohmic resistance of a cell is dependant upon the cumulative resistance of the cell components such as the electrodes, PTLs, and membrane. Since the resistance of these components scales with thickness, and inversely with conductivity, the ohmic losses may be reduced by decreasing component thicknesses and increasing their conductivities by utilizing alternative materials.

Whereas the activation and ohmic losses are rooted in the transfer of charged species, the mass transport losses shown in Figure 1.3 are rooted in the transfer of

⁷Since resistance scales with area, the area-specific resistance is utilized in order to compare cells of differing size [7].

⁸The ionic conductivity of so-called good electrolytes still remains orders of magnitude lower than that in electron conducting metals.

uncharged species. Uncharged species are unaffected by voltage gradients, which are the primary driving force for moving species related to ohmic losses, and therefore must be driven by concentration and pressure gradients. Diffusion, by way of concentration gradients, is the primary mechanism with which uncharged species are transported within porous media such as the CLs and PTLs within the cell. Conversely, transport within flow fields in the bipolar plates is primarily due to convective flow driven by pressure gradients. At elevated current densities, voltage losses occur when gas bubbles block the network with which reactants and products transfer to and from the CLs. As such, mass transport losses may be reduced by altering porous media through alternative manufacturing methods or changing the flow field pattern utilized in the bipolar plates.

1.3 Literature Review

With the number of publications related to AEM-based water electrolysis being approximately two-times lower than the number of PEM-based water electrolysis publications in 2020⁹, it is clear that PEM water electrolysis is currently receiving more research attention. Nonetheless, the number of publications related to AEM-based water electrolysis has been steadily increasing (26 in 2017, 40 in 2018, 49 in 2019, and 67 in 2020) and the following introduces published work related to materials, fabrication methods, and operational parameters for AEM water electrolysis. Note that an emphasis is placed upon cell fabrication, operation, and commercially available materials since the development of alternative materials for membranes, catalysts, and other cell components is beyond the scope of this work.

1.3.1 AEM Water Electrolyzer Components

Primary components that are required for an AEM-based water electrolysis cell include the membrane, CLs, PTLs, and bipolar plates. The following aims to discuss materials that have been commonly utilized in literature for these components, and outline their advantages and disadvantages.

HER and OER Electrocatalysts

As stated in Section 1.2, activation losses dominate cell performance at low current densities and are dependant upon the electrocatalyst that is utilized. For an elec-

⁹Data based upon Web of Science results for proton exchange membrane water electrolysis (142 publications) and anion exchange membrane water electrolysis (67 publications).

trocatalyst to be effective for a given half-cell reaction, such as the HER or OER, it must have high activity, high electronic conductivity, and high stability. The requirement for high activity, assuming a constant Tafel slope, may be discussed in terms of the exchange current density which further describes the rate with which the forward and reverse reactions occur for an electrochemical reaction at thermodynamic equilibrium. Although the exchange current density is dependant upon operational parameters such as temperature, it is also highly affected by the catalyst material as it may alter the activation barrier as well as the number of possible reaction sites [7]. Thus, increasing catalyst activity and/or decreasing the Tafel slope, byway of utilizing an appropriate catalyst, directly decreases the activation losses. The requirement for electrocatalysts to have high electronic conductivity stems from the fact that electron transport within the CLs is through the catalyst themselves. Whereas the first requirement involving activity affects the activation losses, the second requirement involving electron conductivity mainly affects the ohmic losses. Lastly, the third requirement regarding stability specifically requires thermal, mechanical, and chemical stability within the respective electrode environment such that the electrocatalyst does not dissolve, aggregate, or passivate during operation or on/off cycling of the cell.

Due to the intermediate steps that occur in a given electrochemical half-cell reaction, there is a trade off between the catalytic activity and binding energy of the catalyst [7]. That is, if the binding strength of a given catalyst is too strong, then the reacting species may remain bound to the catalyst and inhibit the binding of additional reactants. Conversely, if the binding strength is too low, then the catalyst cannot function as required, and fewer reactions will occur. Stemming from this, the Sabatier principle states that there is an optimum catalytic performance depending on the strength of adhesion between a catalyst and the reacting chemical species [7]. Plotting catalytic activity against binding energy commonly results in a so-called volcano type curve where the optimal material sits atop the volcano. For the HER under alkaline conditions, Pt-based materials are on top of the volcano curve [29] and as such, Pt and Pt|C have commonly been used as the HER catalyst in AEM-based electrolysis [28].

In a screening of potential HER catalysts under alkaline conditions, McCrory et al. used a rotating disk electrode (RDE) assembly to demonstrate that there are several materials that show similar activity to Pt [30]. Furthermore, it was demonstrated that the stability of the alternative catalyst materials was reasonable under constant operation. Recent review papers for electrochemical catalysts for electrolysis by Khan et al. [22] and Hu et al. [18] have both discussed the high amount of attention that

transition metal phosphides are receiving as an HER catalyst. Of note is the work conducted by Zhang et al. in which a bimetallic-structured phosphide electrocatalyst, NiCo_2P_x , required an overpotential of 58 mV to reach 10 mA/cm² in 1 mol/L KOH compared to an unnamed commercially available Pt which had an overpotential of 70 mV under the same conditions. Although catalysts of this nature show promise for the HER in AEM water electrolysis, it is not clear that they have been tested in-situ within an AEM-based cell. Since alternative catalyst such as NiCo_2P_x have not been sufficiently tested within an AEM-based cell and other non-platinum group metal (PGM) catalysts such as Ni–Mo require high loadings due to their reduced activity with respect to Pt (40 mg/cm² [27]), and subsequently, are not ideal for inkjet printing electrode fabrication methods, the work conducted herein utilizes Pt|C as the HER catalyst.

The OER under both alkaline and acidic conditions is the rate-limiting step for water electrolysis since it is a sluggish four-electron reaction under both environments [18, 28, 31]. Under acidic conditions for PEM-based water electrolysis, it is likely impossible that PGMs will be completely eliminated since there are no alternatives that do not dissolve, oxidize, or insulate under OER conditions [22, 30, 31]. As a result, the use of PGMs such as Ir in PEM-based electrolyzers is a limitation since Ir is one of the rarest elements in the Earth’s crust [15]. Conversely, McCrory et al. demonstrated that there are a number of non-PGM based catalysts (> 10) that have equivalent activity to Ir under alkaline conditions [30]. Further, seven of the tested non-PGM catalysts showed excellent longer-term stability as the overpotential required to maintain a current density of 10 mA/cm² was either constant or even decreased over the 24 hour test period. The relatively high availability of non-PGMs for use as the OER catalyst in AEM-based electrolyzers is a notable advantage over PEM-based electrolyzers.

To further validate the use of non-PGM catalysts for the OER in AEM-based electrolysis beyond RDE results, Xu et al. tested cobalt oxide (Co_3O_4), two spinel oxides (NiCoO_x and CoFeO_x), Ni-based oxyhydroxide (NiFeO_xH_y), and other Ni–Co oxide catalysts (NiCoFeO_x and $\text{NiCoO}_x:\text{Fe}$) within an electrolysis cell while holding all other parameters regarding cell components, fabrication, and operation constant [32]. Note that the Ni–Co oxide catalysts containing Fe were produced using two different methods to try and produce a catalyst with Fe in the bulk of the material (NiCoFeO_x) and a catalyst with Fe on the surface of the material ($\text{NiCoO}_x:\text{Fe}$). In addition to the non-PGM catalysts tested, Xu et al. also tested IrO_x to be used as a baseline with which to compare the other catalysts against. The results obtained by Xu et al. are provided in Figure 1.4 where Figure 1.4a shows the resulting cell polarization

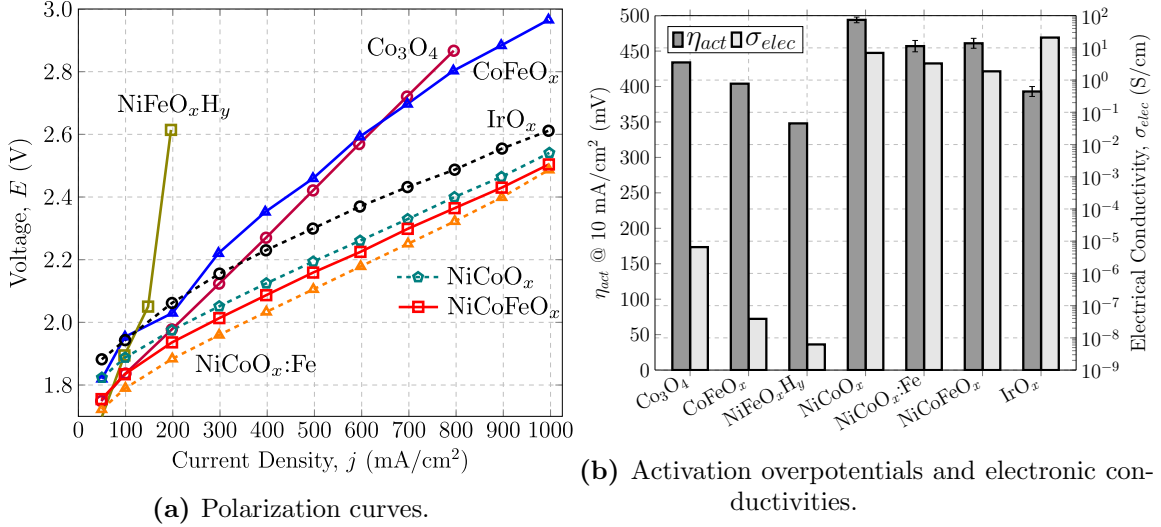


Figure 1.4 – Comparison of in-situ cell performance (tested with loadings of 3 mg/cm² and pure water cell feed), activation overpotentials (tested in 1 mol/L KOH with loadings of 10 $\mu\text{g}/\text{cm}^2$), and electronic conductivities for different OER electrocatalysts. Data sourced from Xu et al. [32].

curves for the different catalysts and Figure 1.4b shows the activation overpotential for 10 mA/cm² in 1 mol/L KOH as well as the dry catalyst electronic conductivities. Considering both Figure 1.4a and Figure 1.4b in tandem, the importance of a high electronically conductive catalyst is apparent. That is, the objectively lowest in-situ cell performance obtained for any of the catalyst was for NiFeO_xH_y , even though it had the lowest activation overpotential amongst all of the catalysts. The steep linear increase of voltage as a function of current density is explained by way of the very low electronic conductivity of NiFeO_xH_y . Although it is not to the same extent, the same relationship is shown for cobalt oxide and CoFeO_x . Conversely, the increased performance shown in Figure 1.4a for NiCoO_x , NiCoFeO_x , and $\text{NiCoO}_x\text{:Fe}$ over IrO_x cannot be readily explained by the ex-situ data provided in Figure 1.4b since IrO_x has a comparably lower activation overpotential and greater electronic conductivity. Xu et al. suggests that the increased performance may be due to an improved interface between the non-PGM catalysts and the polymer electrolyte compared to the IrO_x catalyst [32].

Although Xu et al. [32] has successfully demonstrated that non-PGM catalysts may be used as the OER catalyst for AEM-based water electrolyzers, IrO_x was used as a baseline material with which to compare the alternative catalyst materials to. Since the current work is to also stand as a baseline reference with which to compare additional catalysts against, IrO_x is utilized as the OER catalyst. Additionally, as discussed further in Section 1.3.2, a primary objective of this work was to produce

electrodes via the inkjet printing method, and Mandal et al. has already successfully demonstrated the use of a Nafion-based IrO_x catalyst ink for inkjet printing electrodes for PEM-based electrolyzers [33].

Anion Exchange Membrane and Ionomers

The AEM within an electrolyzer is one of the primary components and is responsible for conducting anions from the cathode to the anode, separating produced gases, and sufficiently insulating against electron conductivity. The main requirements for an AEM are high stability (thermal, mechanical, and chemical), high ionic conductivity, low electronic conductivity, and low permeability of produced gases [14]. However, as stated by Hegesteijn et al. in a recent review on AEMs focusing specifically on fuel cell and electrolyzer applications, the current principal objective for AEM research is to improve AEM chemical and mechanical stability in high-pH and high-temperature¹⁰ environments [34]. Not only is high mechanical stability required to ensure the longevity of the membrane under harsh conditions, but a membrane with high mechanical stability may also be cast in relatively thinner forms that in turn increases electrolyzer performance by reducing ohmic losses [35].

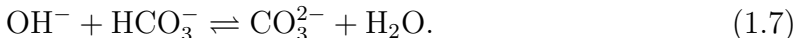
AEMs may be generally classified into three categories: heterogeneous membranes, interpenetrating polymer networks (IPNs), or homogenous membranes [36]. Heterogeneous membranes contain an anion exchange material embedded within an inert compound such that they typically have high mechanical stability, but suffer from low ionic conductivity. IPNs contain two polymer networks which do not have covalent bonds between them. IPNs are composed of a hydrophobic polymer (water repelling) which exhibits good thermal, chemical, and mechanical properties, as well as a conductive polymer responsible for the transport of ions. The separate polymers within IPNs are not bound to one another, which adversely affects the conductivity as the ionically conductive polymer diffuses within the hydrophobic polymer. Lastly, homogenous membranes contain an ionically conductive functional group covalently bonded to a polymer backbone resulting in a single phase polymer. Most AEMs are of the homogenous category and are produced by polymerization and cross-linking or by chemically modifying polymers through various methods [34]. The chemical degradation of homogenous AEMs is caused by the instability of the cationic functional groups, of the polymer backbone, and/or of the functional group-backbone bond [35]. More specifically, many AEMs utilize commercial and traditional polymers as the

¹⁰The average operating temperature for AEM water electrolysis is 56°C [28] versus 80°C for PEM electrolysis [15]. Operating at higher temperatures not only increases catalyst activity, but also increases ionic conductivity, and contributes to higher cell performance [23].

backbone due to their ease of preparation and availability, but the backbone functionalities are also susceptible to degradation [37].

The polymer utilized for the AEM may be utilized as the ionomer as well. The ionomer is commonly included within the cell’s CLs during fabrication and is responsible for ionic conductivity within the CL. An ionomer must have high stability, high ionic conductivity, and good contact with catalyst particles. Although it is not strictly required, an ionomer should be soluble in organic solvents and provide adhesion with catalyst particles. The ionomer commonly plays a role in binding the catalyst particles in the CL such that they remain fixed during cell operation. As noted, it is not a strict requirement for the ionomer to function as the binder since other polymer materials may be used instead. However, it is beneficial to simultaneously utilize the ionomer as the binder since an inert binder will inherently yield any coated active sites of the catalyst as non-active and will reduce CL porosity which is required for mass transport. The ionomer is commonly impregnated within the CL during fabrication by dissolving it in an organic solvent and including it within the catalyst ink that is used for CL fabrication. If the ionomer is not soluble within an organic solvent, then less user- and environmentally-friendly solvents may be required or alternative CL fabrication methods.

Though achieving high AEM stability is currently the principal goal of related research, obtaining AEMs with high ionic conductivities is also important. A recent analysis of ionic conductivity in AEMs and PEMs by Gottesfeld et al. found that the hydroxide conductivity in AEMs is 2–8 times lower than the proton conductivity in PEMs [35]. Beyond the fact that the specific conductivity of the hydroxide ion in a diluted aqueous solution is two times lower than that of a proton, Gottesfeld et al. also states that the large gap in conductivities between AEMs and PEMs is in-part because the conductivity reported for AEMs may often be for the carbonate ion and not the hydroxide ion. Hydroxide ions readily react with carbon dioxide within the atmosphere to form bicarbonate (HCO_3^-) and carbonate (CO_3^{2-}) ions via the following reactions,



The carbonization process has been shown to decrease membrane conductivities by 60–70% in only 40–60 minutes when membranes are exposed to ambient air [38].

Ziv and Dekel have shown that the conductivity of a commercially available AEM (Aemion AF1-HNN8-50 by Ionomr Innovations Inc.) increases six times when converted from a mixed carbonate form to hydroxide form [38]. A schematic of the

electrolyzer-based experimental setup utilized by Ziv and Dekel to convert the membrane from a mixed carbonate form to hydroxide form is provided in Figure 1.5. Water vapor is reduced to form hydrogen and hydroxide at the cathode as per the HER under alkaline conditions. Anions within the membrane, which includes bicarbonate and carbonate initially in the membrane due to its exposure to ambient atmospheric conditions and hydroxide produced as a result of the HER, migrate to the anode. At the anode, the reversed form of the reactions provided in Eqs. (1.6) and (1.7) convert bicarbonate and carbonate to carbon dioxide. Moreover, hydroxide present at the anode is oxidized to produce water and oxygen through the OER. As hydroxide is continuously produced and the bicarbonate/carbonate is consumed, the membrane is converted from its mixed carbonate form to hydroxide form. Ziv and Dekel measured the ionic resistance of the membrane every 10–30 minutes while applying a current of 100 μA until the resistance stabilized. The stabilized resistance, R , is then converted to a conductivity, σ , by using the following relationship,

$$\sigma = \frac{L}{RA}, \quad (1.8)$$

where L and A are respectively the thickness and cross-sectional area of the membrane. As a result, Ziv and Dekel found the true hydroxide conductivity of the Aemion membrane to be 103 mS/cm at 40°C and 90% relative humidity. Although reported values vary greatly, the average proton conductivity reported for Nafion under the same conditions is approximately 70.5 mS/cm [40].

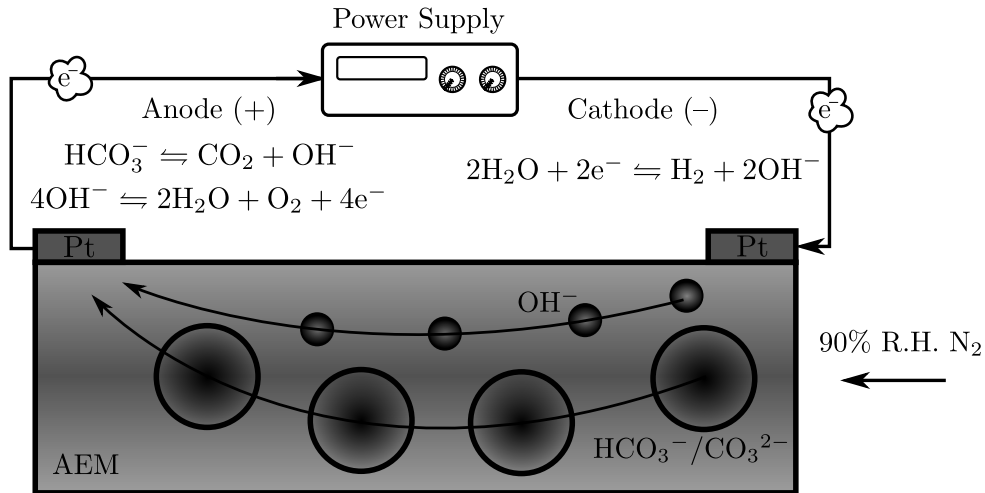


Figure 1.5 – Schematic of experimental setup (740 Membrane Test System with Pt electrodes by Scribner Associates Inc. [39]) used by Ziv and Dekel to determine the true hydroxide conductivity of an AEM [38]. R.H. = relative humidity.

Although reviews on AEMs such as those by Hagesteijn et al. [34] and Gottesfeld et al. [35] have discussed the development of many alternative anion exchange materials (> 20) within literature, there exists a relatively small range of commercially available AEMs and ionomers that are commonly utilized for AEM-based electrolyzer research. A summary of commercially available anion conducting materials is provided in Table 1.1. As seen in Table 1.1, the A-201 membrane and AS-4 ionomer produced by Tokuyama Corporation are currently the most utilized commercially available anion conducting materials. However, direct communication with a representative from Tokuyama Corporation has revealed that the A-201 and AS-4 products have been discontinued and no alternative materials are currently being offered by the company.

Fortunately, two of the last publications utilizing the A-201 membrane by Vincent et al. [44] and Pushkareva et al. [46] have directly compared the in-situ performance of the A-201 membrane to other commercially produced membranes. Figure 1.6 shows the in-situ performance of the A-201 membrane compared to the Fumapem FAA membranes (Figure 1.6a) as well as the Aemion and Sustainion membranes (Figure 1.6b). The polarization curves provided in Figure 1.6a show that the performance of the A-201 and Fumapem FAA-3 membranes are very similar. FAA-3-PK, a PEEK reinforced Fumapem FAA-3 membrane, is shown to suffer from increased ohmic losses compared to the other AEMs [44]. The poorer performance of the FAA-3-PK membrane is likely due to its increased thickness (80 μm) compared to the relatively thinner A-201 and FAA-3 membranes (28 and 40 μm , respectively). Vincent et al. also investigated the stability of the AEM electrolyzer cells fabricated with

Table 1.1 – Summary of companies providing commercially available AEMs and ionomers.

Company	Membrane Designation	Ionomer Designation	References ^a
Tokuyama Corporation	A-201	AS-4	[24, 41–49]
Dioxide Materials	Sustainion	— ^b	[46, 50, 51]
FuMA-Tech	Fumapem FAA-3 ^{c,d}	Fumion FAA-3	[32, 52–57]
Ionomr Innovations	Aemion AF	Aemion AP ^e	[37, 46, 51, 57–59]

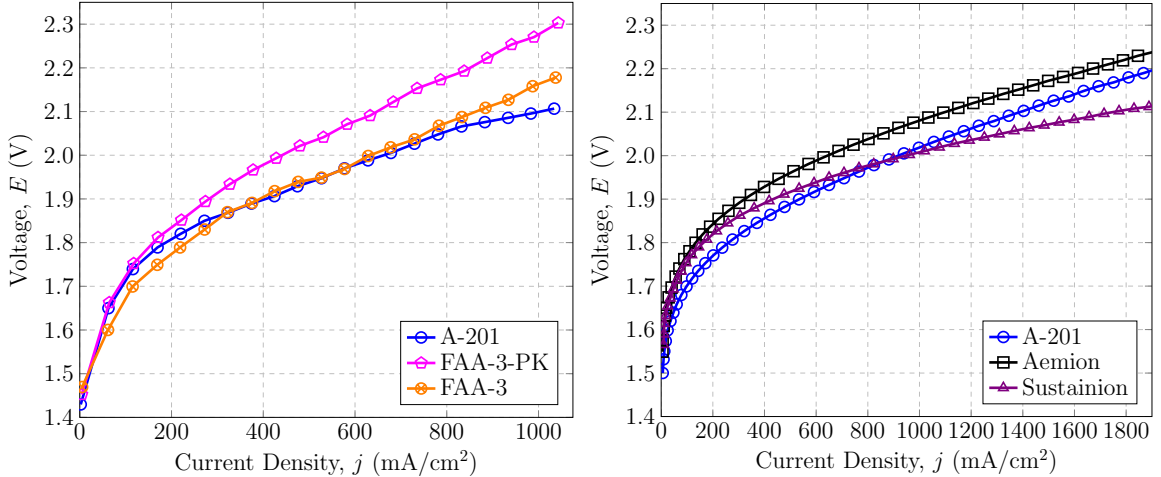
^a References within literature for which the respective membrane or ionomer has been utilized

^b Dioxide Materials produces an alkaline ionomer solution denoted as Sustainion XB-7 for alkaline fuel cells, but it is not clear that it has ever been tested in an AEM electrolyzer

^c Available in a variant containing a polyether ether ketone (PEEK) reinforced backbone denoted as FAA-3-PK

^d FuMA-Tech has recently renamed their ‘Fumapem’ line of products as ‘Fumasep’, but it is referred to as Fumapem throughout this work

^e Ionomr Innovations provides the Aemion polymer material in a powdered form



(a) AEM cells fed with 1 wt.% aqueous K_2CO_3 at 60°C to the anode electrode. Data sourced from Vincent et al. [44]. (b) AEM cells fed with 1 mol/L KOH at 60°C to both electrodes. Data sourced from Pushkareva et al. [46].

Figure 1.6 – Polarization curves for AEM cells utilizing various AEMs available commercially from Tokuyama Corporation (A-201), Dioxide Materials (Sustainion), FuMA-Tech (Fumapem FAA-3), and Ionomr Innovations (Aemion).

the A-201 and FAA-3 membrane variants by operating the cells at 500 mA/cm² for 200 hours with a feed of aqueous K_2CO_3 to the anode at a temperature of 60°C. Vincent et al. found that after 31 hours of operation, the FAA-3 membrane degraded to the extent that the AEM cell was no longer operable and a postmortem investigation revealed holes in the membrane. Conversely, the FAA-3-PK and A-201 membranes remained operable for the full 200 hours and had a net degradation rate of 0.50 and 2.38 mV per hour, respectively. Vincent et al. concluded from the results of their work that if the mechanical strength of the FAA-3 membrane could be improved, that it may be considered as a better option than the A-201 membrane in an AEM-based electrolyzer because the FAA-3 membrane has a similar performance, but is roughly 40% thicker. Since membrane resistance is proportional to thickness [7], the performance of the FAA-3 membrane may become better than the A-201 membrane if it is cast in a thinner form. Lastly, it is of note that the AS-4 ionomer formerly produced by Tokuyama Corporation and the Fumapem ionomer by FuMA-Tech were not compared in the work by Vincent et al. as they utilized an ionomer produced by Enapter (formerly Acta SpA¹¹).

Wright et al. developed a proof-of-concept cell for using the Aemion membrane in an electrolyzer by combining it with Pt|C-based electrodes and operating the cell

¹¹Acta SpA commercially produced an ionomer, HER catalyst, and OER catalyst for AEM electrolyzers, but became Enapter in 2017 and subsequently focused on producing a modular AEM electrolyzer unit, and not individual AEM electrolyzer components [60].

with 1 mol/L KOH feed [37]. However, since AEM-based water electrolysis was not the sole focus of the work conducted by Wright et al., the proof-of-concept cell containing the Aemion membrane was only operated at a modest current density of 25 mA/cm². Nonetheless, the successful operation of the cell with an Aemion membrane was demonstrated for greater than 100 hours. For comparison purposes, Wright et al. also utilized an FAA-3 membrane to operate an electrolyzer under the same conditions, but at a lower current density of 20 mA/cm². Wright et al. found that the FAA-3 membrane based cell became inoperable after 9.5 hours and hypothesized that it was due to membrane degradation resulting in electronic short-circuiting. From the work conducted by Vincent et al. [44] and Wright et al. [37], it is hypothesized that the unsupported FAA-3 membrane may not be suitable for AEM water electrolysis due to issues regarding material stability.

The in-situ performance of the A-201 membrane compared to the Aemion membrane produced by Ionomr Innovations and the Sustainion membrane produced by Dioxide Materials is shown in Figure 1.6b. The materials (other than the AEM), fabrication method, and operation of the cells remained the same for each test. Although the A-201 membrane yields the best cell performance at current densities < 800 mA/cm², it is clear that the AEM electrolyzer that utilizes the Sustainion membrane has lower ohmic losses, which results in a higher cell performance at elevated current densities. The performance of the cell utilizing the Aemion membrane is poorer than the cells utilizing the A-201 and Sustainion membranes at both low and high current densities. The lower ohmic losses associated with the AEM cell constructed with the Sustainion membrane are further highlighted by the fact that the thicknesses of the A-201, Aemion, and Sustainion membranes are reported as 28, 38, and 50 μm , respectively. Pushkareva et al. utilized NiFe₂O₄ on Ni fiber paper for the anode and NiFeCo on stainless steel fiber paper for the cathode and fed the AEM-based cells with 1 M KOH at 60°C. Rather uniquely, Pushkareva et al. utilized 5 wt.% Nafion solution as the ionomer within their CLs. However, because Nafion is a cationic ionomer, the Nafion within the CLs functions as a binder and is not responsible for conducting anions within the CLs. Pushkareva et al. suggests that the use of a cationic binder with anionic membranes results in the formation of bipolar junctions between the anionic and cationic materials. Moreover, the potentials of the bipolar junctions are affected by the specific AEM utilized and that this effect may yield the relatively better performance of A-201 at lower current densities. Lastly, Pushkareva et al. did not test the short-term or long-term degradation of the cells fabricated with the various membranes and therefore the relative in-situ stability of the A-201, Aemion, and Sustainion AEMs is unknown.

Although all of the materials discussed and summarized in Table 1.1 may be utilized to produce an operable AEM-based electrolyzer, Aemion was chosen as the primary material for the current work for the following reasons:

- ◇ The A-201 membrane and AS-4 ionomer materials can not be procured from Tokuyama Corporation.
- ◇ Work from Vincent et al. [44] and Wright et al. [37] has demonstrated that FAA-3 by FuMA-Tech may not be a suitable membrane material for AEM water electrolysis. Additionally, the Fumion FAA-3 ionomer solution by FuMA-Tech contains N-methyl-2-pyrrolidone (NMP), which is not to be sprayed in any manner outside of a fume hood due to its hazardous vapors [61].
- ◇ Although the performance of Sustainion by Dioxide Materials may be better than Aemion, Sustainion is currently the least used material in literature, and is therefore not well documented—this makes it difficult to compare and contrast initial experimental results.

Fortin et al. utilized the commercially available Aemion membrane to fabricate an AEM electrolyzer capable of achieving current densities of 2 A/cm² at potentials of approximately 1.8 V using 1 mol/L KOH at 60°C [57]. Fortin et al. utilized cells fabricated using Aemion membranes to test the effect of the membrane thickness and ion exchange capacity (IEC), ionomer type, operational temperature, and short-term cell stability. Noting that the IEC of a membrane is a measure of the number of exchangeable ions per membrane dry weight [34], Fortin et al. utilized two Aemion membranes with different IECs. To compensate for the lower conductivity of hydroxide ions compared to protons, a focus of AEM research is to increase the IEC [34]. Thus, Fortin et al. utilized the aforementioned methodology developed by Ziv and Dekel to compare the conductivities of Aemion membranes with IECs of 1.4–1.7 and 2.1–2.5 (respectively termed as AF1-HNN5 and AF1-HNN8). Fortin et al. found the ionic conductivity of the higher IEC AF1-HNN8 to be more than two-times greater than the conductivity of the lower IEC AF1-HNN5 (56 vs. 102 mS/cm).

The in-situ performance obtained by Fortin et al. for electrolyzers containing the AF1-HNN5 and AF1-HNN8 membranes with varying thicknesses is provided in Table 1.2. Since the jR -corrected potentials for all of the cells are the same, it is possible to directly attribute the differences in performance to the resistance of the membranes. As expected based upon the relative difference in conductivities between the AF1-HNN8 and AF1-HNN5 membranes, the performance of the AF1-HNN8 membrane, for a given membrane thickness, is better than that of the AF1-HNN5 membrane.

Table 1.2 – Performance data obtained by Fortin et al. for AEM electrolyzers using Aemion membranes of varying IECs and thicknesses using 1 mol/L KOH at 50°C [57].

Membrane	Thickness (μm)	Voltage ^a @ 1 A/cm ² (V)	HFR ^b ($\text{m}\Omega\cdot\text{cm}^2$)	$j\text{R}$ -corrected voltage ^c @ 1 A/cm ² (V)
AF1-HNN8-25	25	1.75	131	1.62
AF1-HNN8-50	50	1.80	174	1.62
AF1-HNN5-25	25	1.81	196	1.62
AF1-HNN5-50	50	1.92	300	1.62

^a From polarization curve data

^b The high frequency resistance (HFR) is taken from the intercept of the real impedance axis in the high-frequency region of the Nyquist plot

^c Determined by subtracting the voltage drop due to the HFR at 1 A/cm² from the overall cell voltage

Furthermore, it is observed that for a given IEC that the thinner 25 μm membranes result in better performance than the thicker 50 μm membranes. Lastly, it is of note that the thicker AF1-HNN8-50 membrane has a very similar performance to the thinner and lower IEC AF1-HNN5-25 membrane. This result is expected because as per Eq. (1.8), the resistance of the material is inversely proportional to conductivity and proportional to thickness. Since the conductivity of the AF1-HNN5 is half that of AF1-HNN8, but AF1-HNN5-25 is half the thickness of AF1-HNN8-50, the two materials produce similar results.

Regarding stability, Fortin et al. tested the various Aemion membrane materials at 500 mA/cm² in 0.1 M KOH at 50°C for approximately 750 minutes. The percentage change in voltage, high frequency resistance (HFR), and charge transfer resistance (CTR) over the test time is provided in Table 1.3. As seen from the data, the

Table 1.3 – Stability data obtained by Fortin et al. for AEM electrolyzers using Aemion membranes of varying IECs and thicknesses using 1 mol/L KOH at 50°C [57].

Membrane	Voltage Increase (%)	HFR Increase (%)	CTR ^a Increase (%)
AF1-HNN8-25	2.4	2	22
AF1-HNN8-50	3.5	-0.4	18
AF1-HNN5-25	4.5	4	29
AF1-HNN5-50	8.1	8	80

^a The charge transfer resistance (CTR) is determined from the difference in the intercept of the high and low-frequency region of the Nyquist plot

degradation of performance was less for the higher IEC AF1-HNN8 membranes than the lower IEC AF1-HNN5 membranes. Moreover, the notably higher increase in the CTR versus the HFR suggests that the degradation in performance for all of the tests was more substantially due to CL degradation than membrane degradation. Since the AF1-HNN8-50 membrane demonstrated relatively good performance and stability, as well as the fact that its increased thickness should make it easier to handle during the electrode fabrication process, the Aemion AF1-HNN8-50 membrane and ionomer (AP1-HNN8) is used as the primary membrane and ionomer material for the current work.

Porous Transport Layers

PTLs, which are also be referred to as current collectors or gas diffusion layers (GDLs) by some, are responsible for simultaneously transporting and distributing water, produced gases, and electrons between the CLs and the bipolar plates. Water provided to the cell through the flow channels within the bipolar plates must be transported through the PTLs and distributed to the CLs to be reacted. Conversely, the hydrogen and oxygen gases, produced at the cathode and anode CLs, respectively, must be transported through the PTLs to the flow channels within the bipolar plates. Lastly, electrons must transfer to the cathode, and from the anode, through the PTLs. As with other cell components, the PTLs must have high stability, as well as high electronic conductivity, sufficient transport properties, and provide mechanical support for the membrane [15].

As discussed by Carmo et al. in their comprehensive review of PEM-based water electrolyzers [15], there is an optimal porosity and pore size distribution for PTLs used in electrolysis. The porosity, defined as the ratio of void space to total volume of the material, may inhibit cell performance if it is too high or too low. That is, PTLs with relatively high porosities promote the facile supply and removal of water and produced gases. However, relatively high porosities also result in decreased electronic conductivity due to the reduced amount of electron conducting solid-phase content. Of course if the porosity is relatively low, then the transport of water and produced gases will be obstructed and result in increased mass transport losses.

Common materials utilized for the PTLs in AEM water electrolysis are carbon, stainless steel, Ni, and Ti [23]. Carbon fiber cloths and carbon fiber papers¹² are commonly utilized in PEM-based fuel cells due to their low-cost, good electronic con-

¹²Carbon cloths contain woven fiber filaments resulting in a fabric-like material while carbon papers contain randomly arranged fibers bonded together with a binder that results in a relatively stiffer and denser material [7].

ductivity, and high porosity [7], and have subsequently been commonly utilized for the cathode PTL in AEM-based electrolyzers [23, 28]. Commercially available Toray 90 carbon paper, with a porosity of 75% and a thickness of 280 μm [62], has been frequently utilized as the cathode PTL in AEM electrolysis [32, 43, 49, 57]. Conversely, the long-term utilization of carbon, or carbon-based materials, in the anode is ruled out due to its instability under the OER conditions [28]. As such, stainless steel, Ni, and Ti-based materials are utilized for the anode PTL in AEM water electrolysis with Ni as the standard. Stainless steel-based materials under the alkaline OER conditions typically have high stability due to the formation of a passivation layer, but are not commonly utilized due to the low interfacial electronic conductivity of the passivation layer [28]. Due to the acidic OER conditions, carbon-based materials also corrode and breakdown when used in the anode of a PEM-based electrolyzer and therefore Ti-based materials are the standard for PEM water electrolysis. This is likely why Leng et al. chose to utilize a Ti-based PTL in one of the first publications on AEM water electrolysis [24], and why others [32, 57, 59] have subsequently chosen to do the same as it is not clear that any formal comparison between Ni and Ti-based PTLs has been conducted. Although Ni foam PTLs are commonly utilized as the anode PTL in AEM water electrolysis [23, 28], no singular commercially available material has frequently been utilized in related literature. Thus, the current work utilizes Toray 90 as the cathode PTL and a Ni felt PTL by Bekaert as the anode PTL (Bekipor Nickel, 250 μm thickness, 60% porosity, 20 μm fibre diameter).

1.3.2 AEM Electrolyzer Assembly and Fabrication Methods

The membrane electrode assembly (MEA), which is comprised of the membrane, cathode CL, anode CL, and their respective PTLs, may be assembled using two primary methods. The first method, which has been primarily used for AEM water electrolysis, is the catalyst coated substrate (CCS) method. For the CCS method, the CLs are deposited onto the cell’s PTLs and then sandwiched against the membrane during cell assembly. As an alternative to the CCS method, the catalyst coated membrane (CCM) method has the CLs deposited onto the membrane with the PTLs sandwiched with the membrane during cell assembly. The CCM method has characteristically been utilized for preparing PEM-based electrolyzers. The CCM method reduces the ionic transport losses between the CLs and the membrane while simultaneously yielding an MEA that is less prone to dimensional changes when the membrane, which swells upon absorbing water, dries out within the cell [15]. Lastly, it is possible to create an MEA that contains one electrode fabricated using one of the methods and the

other electrode with the other method; e.g., a cell may contain a cathode produced with the CCM method and an anode produced with the CSS method, or vice-versa.

A recent review of CCS versus CCM MEA assembly methods conducted by Miller et al. concluded that, in general, the two methods lead to similar performing AEM-based electrolyzers [28]. Within their review, Miller et al. compared 28 instances in which published work utilized the CCS fabrication method to 15 instances in which the CCM method was utilized. Comparing the current densities required to reach a cell voltage of 1.8 V, Miller et al. found the average current density reported for AEM-based electrolyzers fabricated using the CCS method to be 226 mA/cm² vs. 239 mA/cm² for the CCM method¹³. However, comparing cell assembly methods based upon cell performances from many different AEM cell investigations, as stated by Miller et al., is not straightforward since standard materials and testing protocols do not exist. As such, Ito et al. [49] and Park et al. [63] have both investigated the relative performance of AEM-based electrolyzers assembled using the CCM and CCS MEA fabrication methods while attempting to hold all other aspects related to cell materials and operation the same. The work conducted by Ito et al. compared CCM and CCS anodes (all cathodes were CCM-based) and ultimately concluded that a cell fabricated with a CCS anode yielded higher cell performance and stability. However, due to inconsistencies in their electrode fabrication method (blade coating vs. spray coating), cell materials (PTFE binder used for CCS electrodes and AS-4 ionomer used for CCM electrodes), and catalyst loadings (varied as much as 50% cell-to-cell), the work conducted by Ito et al. is not a fair comparison between the two methods. Alternatively, Park et al. compared cells with both electrodes either being CCM- or CCS-based, and by using consistent cell materials and catalyst loadings, was able to demonstrate a higher cell performance and stability using the CCM method [63]. For this reason, and the fact that CCM versus CCS investigations for PEM fuel cells have demonstrated lower charge transfer resistances and higher performances with the CCM method [64, 65], the CCM method was utilized for the majority of the current work.

Regardless of whether the CCS or CCM MEA assembly method is utilized, the most popular electrode fabrication method used for coating the AEM, or PTLs, is spray coating using compressed air [24, 32, 41, 44–46, 48, 50, 55–57, 59, 63]. However, other unique electrode fabrication methods such as ultrasonic spray coating [37], electrodeposition of the catalysts [42, 43], and plasma spraying [58, 66], have also

¹³As an aside, a comprehensive review in 2013 by Carmo et al. found the average potential required for a PEM-based electrolyzer operating at a current density of 1000 mA/cm² to be 1.76 V based upon over 80 publications [15].

been utilized. The decal method, in which a substrate material, such as PTFE, is first coated with catalyst ink and then hot pressed on each side of the membrane at temperatures in excess of 100°C and pressures of roughly 4 MPa, is a common method utilized for producing PEM-based electrolyzer MEAs [15]. However, as stated by Miller et al. [28], the decal method with hot-pressing may not be suitable for AEM-based CCMs since anion conducting materials, such as those from Tokuyama Corporation and FuMA-Tech, have low heat-resistance and cannot tolerate the high temperatures required [49, 63].

An alternative electrode fabrication technique that has been used to fabricate PEM-based fuel cells [67–70] and electrolyzers [33] is inkjet printing. Mandal et al. produced PEM-based CCMs for electrolysis by depositing IrO_x and Pt|C inks in a drop-by-drop fashion onto a Nafion membrane with a commercially available inkjet material printer. Scanning electron microscopy (SEM) was used to show that the produced CLs were uniform and well adhered to the membrane. The drop-by-drop deposition of inkjet printing allows for the accurate control of electrode catalyst loadings since the loading is controlled by the number of layers of catalyst ink printed onto the membrane. Despite the benefits demonstrated for CCM MEAs fabricated using the inkjet printing method, it has not yet been used to produce an AEM-based CCM. Since the inkjet printing fabrication method allows for the accurate control of catalyst loadings, produces electrodes well adhered to the membrane, and has not been used for AEM water electrolysis, a primary goal of the current work is to utilize inkjet printing to fabricate an AEM-based CCM.

Catalyst Inks for Electrode Fabrication

Common electrode fabrication methods such as air and ultrasonic spray coating, and less common methods such as inkjet printing, require catalyst inks in which the catalyst material, and ionomer (if applicable), is suspended within a solvent solution. Regarding catalyst inks specifically utilizing Aemion ionomer, both Wright et al. [37] and Fortin et al. [57] have previously developed catalyst inks to fabricate AEM-based electrodes (Koch et al. [59] has subsequently used the same ink recipes developed by Fortin et al., but with a newer version of the Aemion ionomer denoted by AP2). A summary of the various catalyst inks containing Aemion AP1 is provided in Table 1.4. Wright et al., the developers of Aemion, produced a Pt-based catalyst ink using water and methanol as the ink solvent. The catalyst ink was produced by first adding water, followed by methanol, to the Pt|C catalyst. An Aemion ionomer dispersion, which was separately produced by dissolving the solid-form of Aemion AP1 in methanol to form a 10 wt.% ionomer solution, was then added to the catalyst slurry in a drop-

Table 1.4 – Summary of Aemion AP1-based catalyst inks used in literature.

Property	Wright et al. [37]	Fortin et al. [57]	
Catalyst Material	46.4 wt.% Pt C, TKK ^a	60 wt.% Pt C ^b	Ir black ^b
Ionomer Solution Solvent	Methanol (CH ₃ OH)	Ethanol:H ₂ O (10:1 wt.% ratio)	
Ionomer Solution Solid Content	10 wt.%	2.5 wt.%	
Ink Solvent (wt.% ratio)	Methanol:H ₂ O (3:1)	IPA:H ₂ O (1:1)	
Ink Solid Content (ionomer + catalyst)	1 wt.%	2 wt.%	
Ink Ionomer Content in Solid Phase	15 wt.%	25 wt.%	7 wt.%

^a Tanaka Kikinzoku Kogyo Co., Japan

^b The catalysts used by Fortin et al. were procured from Alfa Aesar

wise manner while the ink solution was rapidly stirred. The resulting catalyst ink contained 1 wt.% solids (ionomer + catalyst), which was further comprised of 15 wt.% Aemion (85 wt.% Pt|C) and the solvent was 3:1 (wt.% ratio) methanol:water. Fortin et al. produced Pt|C- and Ir black-based catalyst inks with Aemion AP1-HNN8 using ethanol and water as the solvent for the ionomer solution (10:1 wt.% ratio), and isopropanol (IPA) and water as the solvent for the ink (1:1 wt.% ratio). The solid wt.% of Aemion in the ionomer dispersion was 2.5 wt.%. To produce the inks, the 1:1 IPA-water solvent was first added to the catalyst and sonicated in an ice bath for 15 minutes. The ionomer dispersion was then added to the catalyst slurry in a drop-wise manner and the ink was sonicated for an additional 10 minutes in the ice bath. The solid wt.% content in both the Pt|C and Ir black inks was 2 wt.%, which contained 25 and 7 wt.% ionomer, respectively.

Since Wright et al. and Fortin et al. utilized ultrasonication spray-coating and traditional spray coating, respectively, to produce their electrodes, their ink requirements were different than for inks used for inkjet printing. Catalyst inks used for inkjet printing must fulfill requirements regarding viscosity, density, and surface tension (covered in more detail in Chapter 2). As such, Saha et al. utilized glycerol as an additive to increase the viscosity of their catalyst ink, which was also comprised of IPA, in one of the first publications in which inkjet printing was used to produce CCMs [68]. Consequently, Shukla et al. also initially utilized glycerol within their Nafion-based catalyst inks [69], but later used ethylene glycol (EG) as it has a lower boiling point [71]. Later yet, Shukla et al. compared results obtained from fuel cells fabricated with EG and propylene glycol (PG), and found that PG-based inks dried faster and resulted in a higher porosity within the CL than EG-based inks [72]. Shukla et al. demonstrated that fuel cells produced using PG-based inks had a higher performance than cells produced using the EG-based inks and suggested that it was due to improved mass transport due to the higher CL porosity. As such, the work

conducted herein utilizes PG as a catalyst ink additive to appropriately increase the viscosity of the catalyst inks for inkjet printing.

1.3.3 AEM Electrolyzer Operation

Using the components discussed in Section 1.3.1, along with the fabrication methods described in Section 1.3.2, it is possible to create an AEM-based water electrolyzer. However, said electrolyzer may be operated using a variety of different liquid alkaline electrolytes, or even water, and as stated in Section 1.2, may be fed to either, or both, of the cell's electrodes. The following discusses how different cell operation methods affect AEM-based water electrolyzer performance and stability.

Operating Temperature

A number of studies have been conducted to determine the optimal operational temperature for an AEM-based electrolyzer [24, 27, 41, 44, 46, 55, 57, 63], and the average operating temperature has been found to be 56°C [28]. Due primarily to kinetic advantages, electrolyzer performance is expected to increase with increasing operational temperature [14]. However, if the operating temperature is increased too high then the presence, as well as the rate, of cell degradation mechanisms may be increased as the anion conducting materials have limited thermal stability [28, 73]. Since the maximum allowable operating temperature for AEM-based electrolyzers is likely limited by the anion conducting material utilized, a summary of studies conducted for cell operating temperatures in which Aemion, Fumapem FAA-3, and Sustainion were utilized is provided in Table 1.5. Although long term cell stability has not been included in Table 1.5, all of the cells tested had the highest performance when operated at the highest temperature tested. Since the operation of AEM water electrolyzers using Aemion, Fumapem FAA-3, and Sustainion membranes has been demonstrated at 60°C, and this value is near the aforementioned average of 56°C, cells tested for the current work were operated at 60°C. Note that an operational temperature of 60°C indicates that both the cell endplates and liquid electrolyte fed to the cell were heated to, and maintained at, 60°C.

Liquid Electrolyte

Although one of the potential benefits of AEM-based electrolysis over conventional alkaline water electrolysis is the ability to operate with deionized water, as opposed to highly caustic solutions of KOH (≥ 5.3 mol/L [16, 17]), the operation of AEM

Table 1.5 – Summary of variable temperature studies conducted with electrolyzers with commercially available AEMs.

Author	Membrane Material	Temperatures Tested [°C]	Optimal Temperature ^a [°C]
Fortin et al. [57]	Aemion AF1	40, 50, & 60	60
Park et al. [63]	Fumapem FAA-3	50, 60, & 70	70
Carbone et al. [55]	Fumapem FAA-3	30, 40, 50, 60, & 80	80
Vincent et al. [44]	Fumapem FAA-3	40, 60, & 80	80
Pushkareva et al. ^b [46]	Aemion AF1, Fumapem FAA-3, and Sustainion	40, 50, & 60	60

^a Determined as the temperature at which the cell demonstrated the lowest polarization losses

^b Pushkareva et al. separately tested AEM-based cells based upon Aemion, Fumapem FAA-3, and Sustainion membranes at 40, 50, and 60°C

water electrolyzers with deionized water has not been widely demonstrated in literature [28]. Studies by Leng et al. [24] and Vincent et al. [44] have both investigated the operation of an AEM-based electrolyzer with deionized water and liquid electrolytes such as 1 mol/L KOH. Leng et al. determined the lifetime of their A-201-based CCM to be ≈ 27 hours when operated at 200 mA/cm² with deionized water fed to the cells cathode. Upon feeding 1 mol/L KOH to the cells anode (directly following the 27 hours of operation with water), Leng et al. observed that the cell recovered and slightly improved upon its initial performance. From their observation, Leng et al. concluded that the degradation of the cell was mainly due to the degradation of the ionomer and/or the membrane-electrode interface. Leng et al. utilized a liquid electrolyte to demonstrate that their cell lacked ionic conductivity within the electrodes and between the electrodes & the membrane when operated with deionized water. The work conducted by Leng et al. suggests that issues stemming from low ionic conductivities within or between cell components may be partially resolved by operating with a liquid electrolyte rather than DI water.

In their study of A-201, Aemion, and Sustainion membranes, Pushkareva et al. tested the in-situ performance of each of the membranes using solutions of 0.1, 0.5, and 1.0 mol/L KOH fed simultaneously to the cells anode and cathode electrodes [46]. Pushkareva et al. found that the HFR for each of the membrane types decreased as the KOH concentration increased from 0.1 to 1.0 mol/L KOH, but decreased most significantly for the A-201 membrane (446 to 133 mΩ·cm²), followed by the Aemion membrane (234 to 120 mΩ·cm²), and decreased the least for the Sustainion membrane (256 to 97 mΩ·cm²). Due to the significant differences in resistances for the different

membranes tested with the same electrolytes, Pushkareva et al. suggested that it was the CL-membrane interface that lead to the different resistances for the different membrane materials. In a similar fashion, Fortin et al. operated their Aemion-based cells with 0.1 and 1.0 mol/L KOH and found that operation with 1.0 mol/L KOH yielded a higher performance [57]. Through their analysis, Fortin et al. suggested the change in performance may be attributed to ionic transport limitations within the electrode, or at the electrode-membrane interface and/or diffusion of hydroxide species to the catalyst surface, but did not investigate the matter further. Due to the complexities involved in further studying how changing the electrolyte effects the cell performance or stability, the current work utilizes 0.85 mol/L KOH with a discussion on the relative difference between operating with 0.85 and 1.0 mol/L provided in Chapter 3.

Electrolyte Feed Method

It has been demonstrated in literature that the liquid electrolyte fed to an AEM-based electrolyzer may be fed to either the cathode, anode, or the cathode and anode [28]. Since the feed method may be changed, there have been a number of studies published that investigate the behavior of AEM-based electrolyzers under different feed methods. A summary of the feed methods tested by various authors is provided in Table 1.6 while a summary of the authors' conclusions are provided in Table 1.7.

From the conclusions presented in Table 1.7 for the work conducted by Park et al. [52] and Leng et al. [24], it is clear that anode or both anode and cathode feed is better than cathode only feed. The reason for this observation, however, is not known as neither Park et al. nor Leng et al. discuss the topic in any detail. The work done and conclusions made by Hnát et al. [74] suggests that cathode only feed leads to the degradation of nickel in the anode, but Leng et al. did not use nickel in the anode of their cell, yet still observed notable cell degradation using cathode only feed. From the work conducted by Cho et al. [48] and Hnát et al. [74], there

Table 1.6 – Summary of studies performed on the different feed methods for an AEM-based electrolyzer.

Author	Anode Only	Cathode Only	Anode and Cathode
Park et al. [52]		✓	✓
Cho et al. [48]	✓		✓
Hnát et al. [74]			✓
Leng et al. [24]	✓	✓	

Table 1.7 – Summary of conclusions for studies performed on the different feed methods for an AEM-based electrolyzer.

Author	Conclusion
Park et al. [52]	Feeding both electrodes with 1 mol/L KOH was the only feasible option. Feeding only the cathode or deionized water to both electrodes resulted in relatively straight vertical lines in the polarization curves (i.e., extremely poor performance).
Cho et al. [48]	Results are relatively hard to interpret because Cho et al. utilized PTFE as the binder in the electrodes and demonstrated that the performance of the cell drastically increased as the cell was cycled with cyclic voltammetry and the electrode morphologies were altered. Nonetheless, results show that anode only operation offers the highest performance, but it is difficult to make a conclusion regarding stability.
Hnát et al. [74]	Demonstrated that feeding both electrodes drastically increases and decreases the concentration of KOH in the cathode and anode, respectively. This observation is due to the production and diffusion of water to the anode that results in a bulk transfer of water from the cathode to the anode. This result was shown to have a negative impact on cell stability as nickel becomes unstable at pHs < 9. Hnát et al. suggests that anodic feed is the most preferential since it ensures that the water required at the cathode must diffuse from the anode and therefore stops the anode from becoming diluted by water. Further suggests that anodic feed has the added benefit of producing relatively dry hydrogen gas.
Leng et al. [24]	Results show that anode only feed results in stable cell performance for 50% longer than cathode only feed. Of note is that Leng et al. did not use any nickel-based components for their cells. I.e., cathode only feed led to some form of increased degradation not based on nickel as discussed by Hnát et al.

is evidence to suggest that anode only feed is better in terms of performance and possibly better in terms of cell degradation than operating with both anode and cathode feed. As such, a high-level comparison of the work conducted in literature suggests that feeding the anode of an AEM-based cell is the best feed method, but no one has produced a systematic analysis of the different feed methods to try and determine more specifically why anode feed may be the best. Simultaneous anode and cathode feed is used for the current work since it allows for a direct comparison with the results obtained by Fortin et al. [57] and Koch et al. [59] who have tested Aemion-based water electrolyzers.

1.4 Objectives

Given the information provided throughout Section 1.3, the primary objective of the current work is to study the suitability of inkjet printing as a fabrication method for AEM-based electrolyzers. To complete this primary goal, three secondary goals must also be completed:

1. Catalyst Ink Development:

Catalyst inks containing Pt|C and IrO_x, along with Aemion ionomer, must be developed for use for inkjet printing cell electrodes.

2. AEM-Based Test-Station Development:

A cell test-station, capable of operating with up to 1 mol/L KOH fed to either, or both, of the electrodes, and that safely handles the produced gases, must be produced.

3. CCM Fabrication and Cell Testing:

To assess the suitability of the inkjet printing fabrication method, CCMs must be fabricated and cells must be assembled and tested.

The catalyst ink development and characterization is the focus of Chapter 2 while the development of the test-station, as well as CCM fabrication and cell assembly/testing results, are covered in Chapter 3.

Chapter 2

Catalyst Ink Development and Characterization

As stated in Section 1.3.1 on electrocatalysts, Pt|C and IrO_x have commonly been utilized as the respective HER and OER catalysts in PEM- and AEM-based electrolysis. For this reason, and because the work conducted herein is to function as a reference baseline with which to compare alternative catalyst materials, Pt|C and IrO_x have been used as the HER and OER catalyst, respectively. To utilize the inkjet printing method to fabricate electrodes, the catalyst materials must be suspended in a catalyst ink solution.

For drop-on-demand inkjet material printers that utilize piezoelectric actuators to initiate drop formation, the drop behavior is commonly characterized by the Weber (We) and Ohnesorge (Oh) numbers [75, 76]:

$$We \equiv \frac{\text{inertial forces}}{\text{surface tension forces}} = \frac{v^2 \rho d}{\gamma}, \text{ and} \quad (2.1)$$

$$Oh \equiv \frac{\text{viscous forces}}{\text{surface and inertial forces}} = \frac{\sqrt{We}}{Re} = \frac{\eta}{\sqrt{\gamma \rho d}}, \quad (2.2)$$

where ρ , η , and γ are the density (kg/m³), dynamic viscosity (Pa·s), and surface tension (N/m) of the catalyst ink, respectively, while v is the velocity of the jetted ink (m/s), and d is the characteristic length (nozzle diameter (m) [76]). Derived from the Weber and Ohnesorge numbers, Fujifilm has provided a set of ink characterization requirements for use with their Dimatix Material Printer (DMP)-2800 series inkjet printer used for the current work [77]. That is, the viscosity should be between 10–12 mPa·s and the effective particle diameter within the inks must be less than 1/100th the size of the nozzle diameter (i.e., < 210 nm for the current work [77]) to avoid blocking the nozzles during the printing process. As evidenced from the definitions of the Weber and Ohnesorge numbers, there are also requirements regarding the surface

tension of the ink, but this has not been investigated for the current work.

2.1 Methodologies for Characterizing Catalyst Inks

To characterize developed catalyst inks, the density, dynamic viscosity, and the approximate particle sizes within the ink have been determined. Since the inkjet printing process is commonly done at temperatures above room temperature, the aforementioned properties must be determined at temperatures in the domain of $\approx 30^\circ\text{C}$. More specifically, for the DMP-2800 series inkjet printer used for the work herein, the minimum setpoint temperature for the cartridge head containing the nozzles is 32°C . As such, all experiments have been conducted at 32°C , unless stated otherwise.

2.1.1 Viscosity Measurements

Since the solvent solutions used for the catalyst inks are commonly binary or ternary mixtures of different chemicals, the required viscosity data is not readily available in literature. Additionally, the concentration of solid-content within the inks (ionomer and catalyst material) may be sufficient to have an effect on the viscosity of the ink. To add further complication, the minimum nozzle temperature of 32°C is not a common temperature used for tabulated data in literature. As such, the viscosity of the catalyst inks and their solvent solutions were determined experimentally using glass capillary kinematic viscometers. Glass capillary kinematic viscometers were used because the temperature of the experiment may be controlled using a water bath, low sample volumes may be used ($\leq 3\text{ mL}$), and they are relatively inexpensive compared to automated alternatives.

For this work, an uncalibrated size No. 100 Cannon-Fenske Routine viscometer ($2\text{--}10\text{ mm}^2/\text{s}$) and a calibrated size No. 2 Zeitfuchs Cross-Arm viscometer ($3\text{--}15\text{ mm}^2/\text{s}$) were used. The uncalibrated Cannon-Fenske Routine viscometer was procured initially and then the Zeitfuchs Cross-Arm viscometer was procured to test opaque liquids and to perform an approximate calibration for the uncalibrated viscometer. Since the Cannon-Fenske Routine viscometer does not have to be removed from the water bath and cleaned between consecutive tests of a given sample (as the Zeitfuchs Cross-Arm viscometer must be), it was used for testing transparent solvent solutions. Conversely, since the Zeitfuchs Cross-Arm viscometer is a reverse flow viscometer, it was used to test the viscosity of opaque catalyst inks.

To perform an approximate calibration of the Cannon-Fenske Routine viscome-

ter, a temperature controlled water bath was set up using a 4000 mL glass beaker (Pyrex No. 1000, Fischer Scientific), a 1.15 kW drop-in immersion heater (#3583K92, McMaster Carr), and an in-house built temperature control box (details provided in Appendix A.1). An annotated image demonstrating the setup of the Cannon-Fenske Routine viscometer in the water bath along with the heater and its thermocouple is provided in Figure 2.1. Note that the makeshift plumb bob pictured in Figure 2.1 is used to ensure that the thermocouple and viscometer are properly positioned within the water bath. The Cannon-Fenske Routine viscometer was charged with ethylene glycol (EG, Fischer Chemical) following the process detailed in ASTM Standard D446 [78] and set up in the temperature controlled water bath, which had a stabilized temperature of 32°C. The temperature of the water bath was verified to be 32°C using a glass thermometer (Kessler 76 mm partial immersion thermometer). After the EG sample and viscometer were equilibrated within the water bath for 20 minutes, the procedure outlined in ASTM Standard D446 was followed to measure the time required for the EG to flow from the upper timing line to the lower timing line twice. The two recorded flow times had an average of 765.2 seconds and agreed within the 1.5% determinability set by ASTM Standard D445 [79] for transparent liquids. The Cannon-Fenske Routine viscometer was then replaced by the Zeitfuchs Cross-Arm

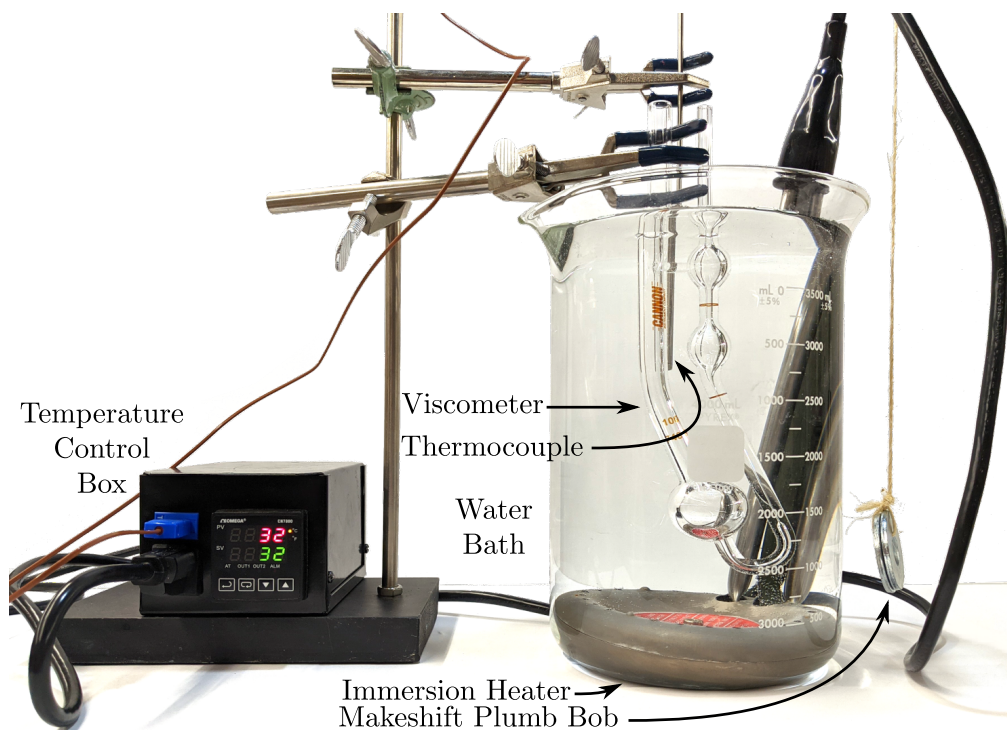


Figure 2.1 – Annotated image of setup containing a glass capillary viscometer used to determine experimental kinematic viscosity values of catalyst inks.

viscometer in the water bath and the process outlined in ASTM Standard D446 was used to measure the time required for the EG to flow from the bottom timing line to the top timing line (the viscometer and EG were again equilibrated for 20 minutes prior to performing the test). After removing the Zeitfuchs Cross-Arm viscometer from the water bath and thoroughly cleaning it, the experiment with EG was conducted a second time—the two measured flow times had an average of 1172.5 seconds and agreed within the 1.0% determinability set by ASTM Standard D445 [79] for opaque liquids.

As per ASTM Standard D446 [78], the constant for the Cannon-Fenske viscometer was then calculated using the following relationship,

$$C_{\text{CF}} = \frac{C_{\text{ZC}}t_{\text{ZC}}}{t_{\text{CF}}} \quad (2.3)$$

where:

C_{CF} is the calculated constant for the Cannon-Fenske viscometer, mm^2/s^2 ,

C_{ZC} is the known constant of the Zeitfuchs Cross-Arm viscometer, mm^2/s^2 ,

t_{CF} is the average flow time of EG for the Cannon-Fenske viscometer, s, and

t_{ZC} is the average flow time of EG for the Zeitfuchs Cross-Arm viscometer, s.

The calibration constant for the Zeitfuchs Cross-Arm viscometer taken from the calibration document provided in Appendix A.2 was adjusted for use at the University of Alberta using a gravitational acceleration constant of 9.813 m/s^2 [80]. Using the obtained data and the known calibration constant for the Zeitfuchs Cross-Arm viscometer, the calibration constant for the Cannon-Fenske Routine viscometer was found to be

$$C_{\text{CF}} = \frac{(0.009474 \text{ mm}^2/\text{s})(1172.5 \text{ s})}{765.2 \text{ s}} = 0.01452 \text{ mm}^2/\text{s}^2.$$

The same process was used to calculate a viscometer constant of $0.01468 \text{ mm}^2/\text{s}^2$ using silicone oil ($5 \text{ mm}^2/\text{s}$, Sigma-Aldrich). As per ASTM Standard D446 [78], the two experimentally determined calibration constants for the Cannon-Fenske viscometer should differ by less than 0.3%, however, in this case they differed by 1.1%. As such, the calibration of the viscometer is referred to as an approximate calibration. The final calibration constant of the Cannon-Fenske viscometer was taken as the average between the two obtained values, $0.01460 \pm 3.4(10^{-5}) \text{ mm}^2/\text{s}^2$, where the detailed uncertainty calculations are provided in Appendix B.1.

The experimental setup used to determine the viscosity of a given catalyst ink or solvent solution was the exact same as discussed for the calibration process shown

in Figure 2.1. As per ASTM D445 [79], the unknown kinematic viscosity of a given ink was determined using two time measurements that were either within 1.5% or 1.0% of one-another depending upon whether the solution was transparent or opaque, respectively. In the event that the two obtained time values were within the stated determinability, then the viscosity was found using the following relationship,

$$\nu = Ct_{avg.}, \quad (2.4)$$

where ν is the determined kinematic viscosity (mm^2/s), C is the calibration constant of the used viscometer (mm^2/s^2), and $t_{avg.}$ is the average of the two obtained times (s). Conversely, if the two time measurements were not within the required determinability, then the viscometer was thoroughly cleaned, dried, and the experiment was repeated.

2.1.2 Density Measurements

As with the viscosity, the rather complex composition of the solvent mixtures and the varying concentration of solid-content in the inks makes it difficult to estimate the density from literature. As such, a best estimate of the density has been determined experimentally by measuring the mass of the ink as the volume is systematically increased from 2–10 mL in 1 mL increments. This process was done using a 10 mL graduated cylinder (Kimax 20024, ± 0.1 mL uncertainty) and a mass balance (Entris 124i-1S by Sartorius, 0.1 mg resolution). The density of the fluid was then the resulting slope of the masses plotted against the volumes. Determining the slope of the plot using a linear regression has provided the lowest uncertainty in the determined density. To validate this method, the density of deionized water and methanol at room temperature were found to be 1.001 ± 0.013 g/mL and 0.796 ± 0.010 g/mL, respectively. Detailed information on how the uncertainties were obtained for the density values is provided in Appendix B.2. Both of the densities calculated using this method are in agreement with values reported in text (0.997 and 0.787 g/mL for water and methanol, respectively, at 25°C) [81].

The experimental methodology was further developed to only require 5 mL of the sample since the developed catalyst inks contain rare PGMs (a lower volume requires less of the expensive catalyst). Since the density is used to calculate the dynamic viscosity using the kinematic viscosity, and the dynamic viscosity must have an uncertainty of $< 2\%$ for dynamic light scattering experiments [82], the uncertainty in the density must also be $< 2\%$. To reduce the uncertainty in the experimentally determined density values, the sample volume was increased from 1–5 mL in 1 mL

increments as stated before, but the test was repeated four times. The density from each test was determined following the aforementioned process using the line of best fit, and then the final density was taken as the average of the four determined values. To validate this method, the density of water and methanol were again obtained ($0.986 \text{ g/mL} \pm 1.62\%$ and $0.784 \text{ g/mL} \pm 1.53\%$, respectively) and found to be within uncertainty of the known values reported in text (refer to Appendix B.2 for details on the uncertainty analysis). For reference, the uncertainty associated with a single test using only 5 mL was found to be $> 3\%$.

As an aside regarding the density measurements, to obtain densities that are in agreement with literature, the linear regression cannot be forced through zero. That is, if the linear regression was forced through zero, then the density of water was found to be $0.970 \pm 0.006 \text{ g/mL}$, which is not in agreement with values from literature. It appears that the graduated cylinder used had an offset such that the absolute volume being measured was notably incorrect, but that the relative change in volume was accurate. This hypothesis may be verified by using the resolved density, i.e., the slope of the line, to convert the zero-intercept of the linear regression, i.e., a negative mass, to a volume and then compare the calculated zero-intercept volume for multiple fluids. If the calculated zero volume for multiple fluids is the same, then it demonstrates that there is a valid offset for the graduated cylinder. However, because the zero-intercept determined by the linear regression is an extrapolation of the data, the corresponding uncertainty in the intercept itself, and consequently the calculated offset volume, is very large and this method cannot actually be used to validate the hypothesis. This is all to say that it was very important to validate the described experimental method by finding the densities of fluids with known values before attempting to measure unknown densities.

Although it may be possible to create a water bath on the mass balance in an effort to control the temperature of the sample during the experiment, the density of water decreases $\approx 0.003 \text{ g/mL}$ from 20 to 32°C [83], which is notably lower than the uncertainty in the experimentally determined density at room temperature (0.013 g/mL). Although more significant, the density of methanol decreases $\approx 0.012 \text{ g/mL}$ from 20 to 32°C [84], which is similar to the uncertainty in the experimentally determined density at room temperature (0.010 g/mL). Thus, since the density of the given chemicals vary approximately 1% from room temperature to the desired temperature of 32°C , there are diminishing returns on attempting to control the temperature of the experiment. I.e., the density measurements were conducted at room temperature because the accuracy of the experimental method would have to be improved to justify controlling the temperature.

2.1.3 Particle Size Measurements

Dynamic light scattering (DLS) may be used to analyze the stability and particle size distribution of the developed catalyst inks. In DLS, suspended particles are probed optically by a monochromatic light source (i.e. a known single wavelength). Particles suspended in the media scatter incident rays such that the rays obtain a time-dependent phase. Each individual ray that is scattered will have a time-dependent phase shift, or a spectral frequency shift from the central frequency of the light source, that is linked to the time-dependent position of the particle that scattered it [82]. At an angle θ from the incident light, this frequency shift may be observed or detected as a change in light intensity¹. Measured over time, random particle motion due to Brownian motion forms random fluctuations in observed light intensities. In DLS, the speed of the particles due to Brownian motion is indirectly measured by measuring the rate at which the intensity of the scattered light fluctuates [85]. The underlying principle of DLS is that the size of the particles is related to the rate with which the intensities fluctuate. That is, small and thereby faster moving particles will result in more rapid fluctuations in the observed intensities, while larger and thereby slower moving particles will result in less rapid fluctuations [86].

Practically, the random fluctuations in observed light intensities with respect to time are processed using an autocorrelation function, referred to as $G^{(2)}(\tau)$ [82, 87].

$$G^{(2)}(\tau) = \frac{1}{T} \sum_i^T I(t) I(t + \tau) \quad (2.5)$$

where

t is the absolute or arbitrary time,

τ is the time difference, or delay, between observed intensities,

$I(t)$ is the observed intensity at time t , and

T is the total measurement time.

For small time differences (i.e., low values of τ) particles are not given sufficient time to change from their initial state. As a result, intensity fluctuations for low values of τ are relatively similar to one another. This similarity in intensities yields larger values for the autocorrelation function, $G^{(2)}(\tau)$. Conversely, as the time difference between observed intensities increases (i.e., for larger values of τ), the initial and

¹The optical phase shifts, or spectral frequency shifts, may be compared with all scattered light (homodyne), or compared to a portion of the unaffected incident light (heterodyne).

final state of the particles causing the light to be scattered differ from one another. The result being that intensities observed for the two states are dissimilar and values of $G^{(2)}(\tau)$ decrease. Eventually, the two states compared to one another for sufficiently large values of τ will be completely dissimilar and $G^{(2)}(\tau)$ will remain constant for increasing values of τ . Thus, the normalized intensity autocorrelation function for particles in Brownian motion has the form of an exponential decay [82, 86]. As such, the normalized form of $G^{(2)}(\tau)$ may be written as follows,

$$G^{(2)}(\tau) = A [1 + B \exp(-\Gamma\tau)], \quad (2.6)$$

where

A is the baseline, or normalization factor,

B is the intercept of the correlation function that is an instrument dependent factor,
and

Γ is the exponential decay rate.

The decay rate may then be related to the diffusion coefficient, D , of homogeneous spherical particles via the following relationship,

$$\Gamma = Dq^2, \quad (2.7)$$

where q is the modulus of the scattering vector given by,

$$q = \frac{4\pi n}{\lambda} \sin\left(\frac{\theta}{2}\right), \quad (2.8)$$

wherein

n represents the real part of the refractive index of the media,

λ is the wavelength of the incident light, and

θ is again the angle with which the light intensity is detected relative to the incident light.

As stated in ISO 22412 [82] on particle size analysis with DLS, the particle size of the sample is not directly determined, but instead the diffusion coefficient is related to the particle size via the Stokes-Einstein equation,

$$D = \frac{k_B T}{3\pi\eta d}, \quad (2.9)$$

where

D is again the diffusion coefficient, m^2/s ,

k_B is the Boltzmann constant, J/K ,

T is the absolute temperature, K ,

η is the dynamic viscosity of the media, $\text{Pa}\cdot\text{s}$, and

d is the diameter of the non-interacting spherically shaped particles, m .

Thus, the chronological workflow for obtaining the size of particles suspended within a media from DLS is as follows:

1. Optically probe the suspended particles with a known single wavelength
2. Obtain the resulting intensity fluctuations of light scattered by the particles as a function of time
3. Apply an autocorrelation function to the light intensity fluctuations to obtain an expression for an exponential decay
4. Determine the decay rate of the exponential decay and relate it to the diffusion of the particles
5. Utilize the Stokes-Einstein equation (Eq. (2.9)) to estimate the diameter of the particles

Of course for practical cases of particle analyses, determining particle sizes is far more complex than the aforementioned workflow may indicate. That is, Eqs. (2.5) to (2.7) and (2.9) are applicable for homogeneous spherical particles that are monodispersed and only undergoing translation. However, as stated within ISO 22412, Eqs. (2.5) to (2.7) and (2.9) can be used to analyze measurements of non-spherical and non-homogeneous particles, where both translational and rotational diffusion are present, but then an apparent or hydrodynamic particle size is determined [82]. Further, as per ISO 22412, the polydispersity, i.e., a measure of the particle distribution broadness, of a sample is handled by statistically analyzing the varying decay rates (Γ). That is to say that different sized particles within a sample will result in differing diffusion coefficients that are proportional to the slope of the autocorrelation function. As such, the time autocorrelation function for the scattered light (Eq. (2.6)) is written in terms of the time autocorrelation function for the scattered electric field²,

²The autocorrelation function for the scattered electric field may be understood as a mathematical interpretation of the particle motion [87].

$g^{(1)}(\tau)$ [88],

$$G^{(2)}(\tau) = A \left[1 + B (g^{(1)}(\tau))^2 \right], \quad (2.10)$$

where $g^{(1)}(\tau)$ may further be written as a function of the normalized distribution of decay rates, $C(\Gamma)$,

$$g^{(1)}(\tau) = \int_0^\infty C(\Gamma) \exp(-\Gamma\tau) d\Gamma. \quad (2.11)$$

The so-called probability density function of $C(\Gamma)$ accounts for the effect that larger particles scatter more light and is strongly related to the particle size distribution [87]. As per the cumulants method defined in ISO 22412, the $\exp(-\Gamma\tau)$ term is then expanded about $\exp(\bar{\Gamma}\tau)$ where $\bar{\Gamma}$ is the average decay rate defined as follows,

$$\bar{\Gamma} = \int_0^\infty \Gamma C(\Gamma) d\Gamma. \quad (2.12)$$

However, the expansion is truncated after the second order term such that Eq. (2.10) becomes

$$G^{(2)}(\tau) \approx A \left[1 + B \exp(-2\bar{\Gamma}\tau + \mu_2\tau^2) \right], \quad (2.13)$$

where μ_2 is the second moment (variance) of $C(\Gamma)$. Fitting Eq. (2.13) to the experimentally determined autocorrelation function, the values of B , $\bar{\Gamma}$, and μ_2 are determined [87]. The value of $\bar{\Gamma}$ is then used in place of Γ in Eq. (2.7) to find the diffusion coefficient (D), which is then used in the Stokes-Einstein equation (Eq. (2.9)) to determine an average hydrodynamic particle size within the sample. Additionally, the polydispersity index of the sample, PI , which is a measure of the broadness of the distribution, is defined as [82]

$$PI = \frac{\mu_2}{\bar{\Gamma}^2}. \quad (2.14)$$

For the current work, a Litesizer 500 by Anton Paar was used for both conducting and obtaining data for DLS experiments. The aforementioned process required to obtain the average hydrodynamic particle size and the polydispersity index via the cumulants method is automatically completed for the user by the Kalliope software by Anton Paar. In the event that the experimental autocorrelation function contains multiple distinct decay rates, the advanced cumulant algorithm used by the Kalliope software fits the first decay to determine the hydrodynamic diameter of the sample [85].

Of more use than the results obtained by the cumulants method is the intensity-weighted particle distribution. To determine the particle distribution within the sample, the Kalliope software compares the experimental correlation function with a set

of calculated correlation functions and tries to find the combination which fits best to the experimental data. This is done in part by recognizing that solutions for $C(\Gamma)$ must be greater than zero (cannot have negative distributions), and that the integral of the distribution must be one. The process of reconstructing the particle size distribution is relatively complex and utilizes both a non-negative least squares matrix algorithm and a so-called Tikhonov regularization [87].

Prior to analyzing the developed catalyst inks, the bias uncertainty of the Litesizer 500 was validated using a certified reference material and the procedure outlined in ISO 22412 on particle size analysis using DLS [82]. The validation process and corresponding analysis is provided in Appendix B.3. The results obtained by the Litesizer for the reference standard met the requirements for bias stated within ISO 22412, and exceeded the requirements for repeatability. That is, the polydispersity index is required to be less than 10% while the standard deviation in the particle size for multiple measurements must be less than 2%. For the results obtained by the Litesizer, the largest polydispersity index was 7.34% and the standard deviation in the particle size was 0.9%.

To perform a particle size experiment, approximately 1 mL of a given catalyst ink was placed within a quartz cuvette, and the cuvette was inserted into the Anton Paar Litesizer 500. The Kalliope settings commonly used to perform an experiment are provided in Figure 2.2. Note that the developed catalyst inks were generally opaque such that no light was able to transmit through the samples, and for this reason, the measurement angle used was back scattering. When using back scattering, the angle at which the light intensity is detected (θ) is 175° . As shown in Figure 2.3, the Litesizer 500 is also capable of side scattering ($\theta = 90^\circ$) and forward scattering ($\theta = 15^\circ$). Regarding the input parameters for the material, platinum was selected for samples containing Pt|C or IrO_x because the refractive index and absorption of the scattering material is only required for Mie theory if the intensity size distribution is transformed into a volume- or number-weighted distribution [89]. To confirm that the material properties do not affect the reported DLS results, recalculations³ were performed using material properties for platinum, graphite, and iridium and the results (particle size distribution, hydrodynamic diameter, and polydispersity index) were all the exact same. Regarding the viscosity, it was assumed that the tested samples were Newtonian such that the data obtained using glass capillary kinematic viscometers was valid for use with DLS. Where applicable for particle size distributions, a sample print (> 10 printed layers) or attempted print (< 5 printed layers) of

³Obtained DLS results may be recalculated using the Kalliope software where the material and solvent properties may be changed.

the ink on aluminum foil has been included.

2.1.4 Refractive Indices of Solvent Solutions

As stated in Section 2.1.3, the refractive index of the solvent solution is required when performing a DLS experiment. A general interpretation of the refractive index is that light travels faster through materials with relatively low refractive indices, and slower through materials with relatively higher indices [87]. The refractive index of a given media, n_i , is defined as follows,

$$n_i = \frac{c}{v_i}, \quad (2.15)$$

where c is the speed of light in vacuum and v_i is the speed of light in the given medium. The Litesizer 500 by Anton Paar determines the light intensity through the cuvette and the sample at various lens positions, wherein the light passes through the lens prior to the cuvette as shown in Figure 2.3. Note that forward scattering is used when performing refractive index experiments. Adjusting the focus position of the lens over various lengths and measuring the intensity results in a curve with a maximum. At the maximum intensity, the light beam has been bent back to the detector window and the bending of the light by the sample has been compensated by adjusting the focussing lens. The lens position which corresponds to the maximum intensity is then an indirect measure of the sample's refractive index [87].

The screenshot displays the Kalliope software interface, divided into two main sections: 'Input parameters' and 'Series configuration'.

Input parameters:

- Comment:** Test of standardized PtC Nafion Ink, 1.25 wt.% solid-phase, 15.2 wt.% Nafion ionomer, 6 mL of ink, Gravimetric Recipe: 57.5 mg TKK PtC catalyst (46.6 wt.% Pt)
- General:** Measurement cell: Quartz; Measurement angle: Back scatter (175°); Target temperature: 32 °C; Equilibration time: 00:01:00; Analysis model: General; Cumulant model: Advanced
- Quality:** Mode: Manual; Number of runs: 10; Time for each run: 00:00:08
- Filter:** Mode: Automatic; Optical density: 0.0
- Focus:** Mode: Automatic; Position: 0.0 mm
- Material:** Material unknown: ; Name: Platinum; Refractive index: 2.4160; Absorbance coefficient: 5.4000 1/m
- Solvent:** Name: Nafion-PtC-Ink; Refractive index: 1.3861; Viscosity: 5.3053 mPa.s

Series configuration:

- Series:** Type: Repetition; Keep focus position: ; Keep filter:
- Parameter values:** A list of 10 'Repetition' entries, each with a trash icon and a refresh icon.

Figure 2.2 – Sample input parameters set for the Kalliope software when performing a DLS particle size series test with the Anton Paar Litesizer 500.

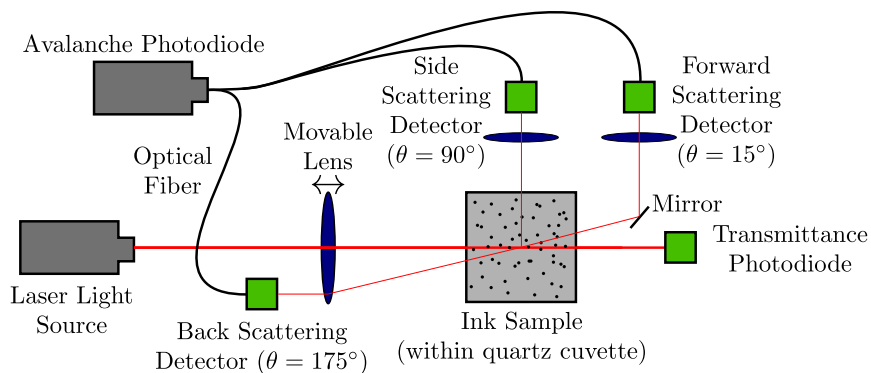


Figure 2.3 – Simplified optical setup of the Anton Paar Litesizer 500 (adapted from [87]).

In an effort to validate the refractive index results obtained by the Anton Paar Litesizer 500, two experiments were conducted to determine the refractive index of PG at 32°C. The first test yielded a refractive index of 0.979 while the second was 0.786; the errors associated with these values were 31.5% and 45.0%, respectively, compared to the known value of 1.429 [90]. Due to the inconsistency of the experimentally determined refractive index values, and their high errors compared to the known value, the refractive indices of the various solvent solutions were *not* determined experimentally. Further, due to the significant difference in the experimentally determined values (19.7%), it was hypothesized that the Litesizer 500 was highly sensitive to any contaminants in the sample or on the quartz cuvette and that a clean-lab absent of dust and other containments may be required to obtain accurate data.

In leu of the experimentally determined refractive index values, a sensitivity test was performed using a result obtained for the certified reference material discussed in Section 2.1.3. For the test, the DLS result for the reference material was recalculated using a refractive index of 1.3299 and 1.4290, which correspond to water and PG, respectively [90, 91]. These refractive index values were used as they are the lower and upper bounds for the various chemicals used for the current work (water, PG, IPA, and methanol). The recalculated hydrodynamic diameters varied 33.8 nm with the lower refractive index of water yielding a smaller particle size and vice versa for the value corresponding to PG. The change of 33.8 nm corresponds to 15.7% compared to the known certified mean diameter of the sample of 215 nm. As such, a refractive index value of 1.3861 corresponding to a 1:1 wt.% ratio of PG and water at 32°C [90] was used for DLS tests with an understanding that the resulting particle sizes may vary in excess of 15% due to the refractive index alone.

2.2 Results and Discussion for Catalyst Ink Development

Prior to beginning catalyst ink development using Aemion AF1-HNN8 ionomer, the standardized Nafion-based Pt|C catalyst ink developed by S. Shukla [72] that has commonly been used to produce inkjet printed electrodes was produced and characterized to serve as a baseline with which to compare developed inks to. The Pt|C ink contained 1.36 wt.% solids (catalyst and ionomer content), 15 wt.% ionomer in the solid-phase, and the solvent solution contained 47 wt.% PG, 48 wt.% IPA, and the remaining wt.% was comprised of the ionomer solution solvent. To create the catalyst ink, 57.5 mg of Pt|C catalyst (46.7 wt.% Pt, Tanaka Kikinzoku Kogyo (TKK) Company, Japan) was mixed with 1812 mg of PG and 1851 mg of IPA. All mass measurements were conducted using an Entris 124i-1S lab balance by Sartorius with a resolution of 0.1 mg. The ink was then sonicated for 30 minutes in a water bath (Branson 1800, 40 kHz), and the 202.9 mg of Nafion ionomer solution (Liquion solution LQ-1105 1100 EW, 5 wt.%, Ion Power) was added to the ink in a drop-wise fashion with a 15 second delay between drops. To further disperse the catalyst ink and break down agglomerates, the ink was probe sonicated at a frequency of 20 kHz (Qsonica S-4000, 2 minute on, 1 minute off, 15 minutes total, 20% amplitude). The ink was then degassed in the water bath for 30 minutes and left atop a magnetic stirrer platform (350 rpm) prior to the density, viscosity, and DLS tests being performed.

The results for the density, viscosity, and DLS experiments conducted with the Nafion-based Pt|C ink are summarized in Table 2.1 while the particle size distributions are provided in Figure 2.4. Note that the viscosity used to obtain the DLS results was for the complete catalyst ink found using the Zeitzfuchs Cross-Arm viscometer. Although the average hydrodynamic diameter of the catalyst ink (258 nm) is greater than the recommended maximum size of 210 nm, the catalyst ink has been successfully used for inkjet printing electrodes using the Dimatix printer many times (> 100). This result suggests that the recommended maximum particle size of 210 nm is either somewhat flexible and particles may be larger than this (the particle size distributions in Figure 2.4 show sizes up to 1 μm), or the absolute value of the particle sizes obtained from DLS are overpredicted. Given that the maximum particle size provided by Fujifilm is a recommendation and there are a number of inputs required for DLS (each with their own associated uncertainty), each of the above hypotheses could be correct. As such, the particle sizes obtained for developed inks will not be analyzed on an absolute basis, but relative to the baseline results obtained for the Nafion-based Pt|C ink.

Table 2.1 – Summary of ink characterization results obtained for baseline Nafion-based Pt|C catalyst ink.

Density, ρ (g/cm ³)	0.885 ± 0.014
Dynamic Viscosity ^a , η (mPa·s)	5.31 ± 0.09
Hydrodynamic Diameter ^b , d (nm)	258 ± 46
Polydispersity Index ^b , PI (%)	22.9 ± 4.7

^a The uncertainty in the dynamic viscosity has been obtained as per Appendix B.4

^b The plus-minus values for the hydrodynamic diameter and polydispersity index have been taken as the standard deviation in the 10 DLS repetitions conducted

Although the viscosity of the Nafion-based Pt|C catalyst ink was found to be lower than the minimum requirement provided by Fujifilm (5.31 vs. 10 mPa·s), it is likely that other properties such as the surface tension result in the ink having sufficient properties to be printable. This result again suggests that there is flexibility in the guidelines provided by Fujifilm.

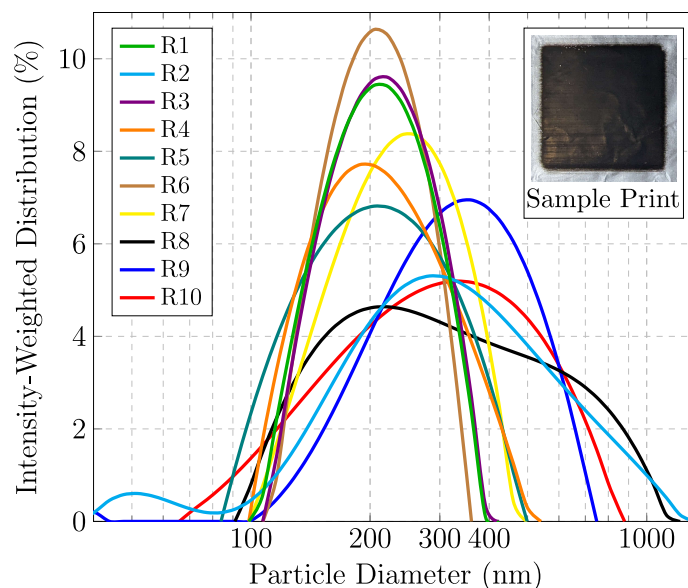


Figure 2.4 – Intensity-weighted particle size distributions obtained from DLS for baseline Nafion-based Pt|C catalyst ink. Note that R1 through R10 refers to repetition one through ten, respectively, in the chronological order tests were conducted.

2.2.1 Aemion-Based Pt|C Catalyst Ink

To begin catalyst ink development with Aemion AP1-HNN8 ionomer, the work by Wright et al. [37] was used as a starting point since the work by Fortin et al. [57] had not yet been published. The general catalyst ink recipe from Wright et al. contained three primary parameters:

1. the wt.% of solid-phase ionomer content⁴,
2. the wt.% of methanol to water in the solvent solution, and
3. the wt.% of the total solid content within the ink.

Note that the solid content within the ink is comprised of both the catalyst and the solid-phase portion of the ionomer solution. To utilize the generalized catalyst ink recipe based upon relative weight percentages by Wright et al., a system of linear equations was developed to convert the recipe to gravimetric form. Although Wright et al. did not include an additive to increase the viscosity of their catalyst ink, an additional variable for the wt.% of PG in the liquid-phase of the catalyst ink was included since it was anticipated it would be required for inkjet printing. Moreover, the methanol used by Wright et al. was generally referred to as an alcohol in the system of equations since other alcohols, such as IPA, may be used. The derivation of the system of linear equations is provided in Appendix C.

Aemion Pt|C Ink 0.1

The developed system of linear equations was used to produce a gravimetric Pt|C-based catalyst ink recipe following the recipe specified by Wright et al. [37] with 1 wt.% solid content comprised of 15 wt.% ionomer content, and a 3:1 wt.% ratio of methanol:water (PG content of 0%). Since the Aemion AF1-HNN8 ionomer was received in powdered form, as opposed to the previously discussed Nafion ionomer which comes in a 5 wt.% liquid solution, the first step for producing an ink was to dissolve the ionomer into a solution. The ionomer solution was produced using 1 g of Aemion AP1-HNN8 ionomer powder dissolved in 19 g of methanol ($\geq 99.9\%$, Sigma-Aldrich) using a magnetic stirrer to produce a 5 wt.% ionomer solution⁵. The Aemion ionomer solution was left atop the magnetic stirrer in a Nalgene bottle until its later

⁴Recall from Section 1.3.1 that the solid form of the ionomer is commonly dissolved into its own solution, and then added to the catalyst ink.

⁵Of course the resulting volume of ionomer solution was far greater than would be required for producing a single ink, but the intent was to produce an ionomer solution that may be used to produce multiple inks.

use. To create the catalyst ink, 1251 mg of deionized water (18.2 M Ω , Millipore Gradient Milli-Q) was added to 42.9 mg of 46.7 wt.% Pt|C catalyst (TKK Company, Japan), followed by 3611.1 mg of methanol. The 152.1 mg of previously prepared ionomer solution was then added in a drop-wise fashion to the vial during bath sonication (15 second delay between consecutive drops). Following the addition of the ionomer, the catalyst ink was left atop the magnetic stirrer overnight before being tested. The resulting ink was named Aemion Pt|C Ink 0.1. Note that the ink was only bath sonicated during the addition of the ionomer, which required approximately 20 minutes.

The viscosity of the 3:1 wt.% ratio of methanol:water used for Aemion Pt|C Ink 0.1 was obtained using the Cannon-Fenske viscometer and the approximate particle size of the ink was analyzed using DLS. Note that the viscosity used to obtain the DLS results was for the solvent solution only, and did not contain solid content (catalyst and ionomer). As seen in Figure 2.5a, the resulting particle distributions for the catalyst ink were unimodal and consistent, with the exception of repetition seven (R7). All repetitions (R1–R10) were conducted in chronological order with a one-minute delay between repetitions. The hydrodynamic diameter of the ink was determined to be 624 ± 10 nm with a polydispersity index of $17.2 \pm 4.9\%$. Since the DLS test required approximately one hour, the consistent particle size distributions indicated that the catalyst ink with Aemion ionomer is stable.

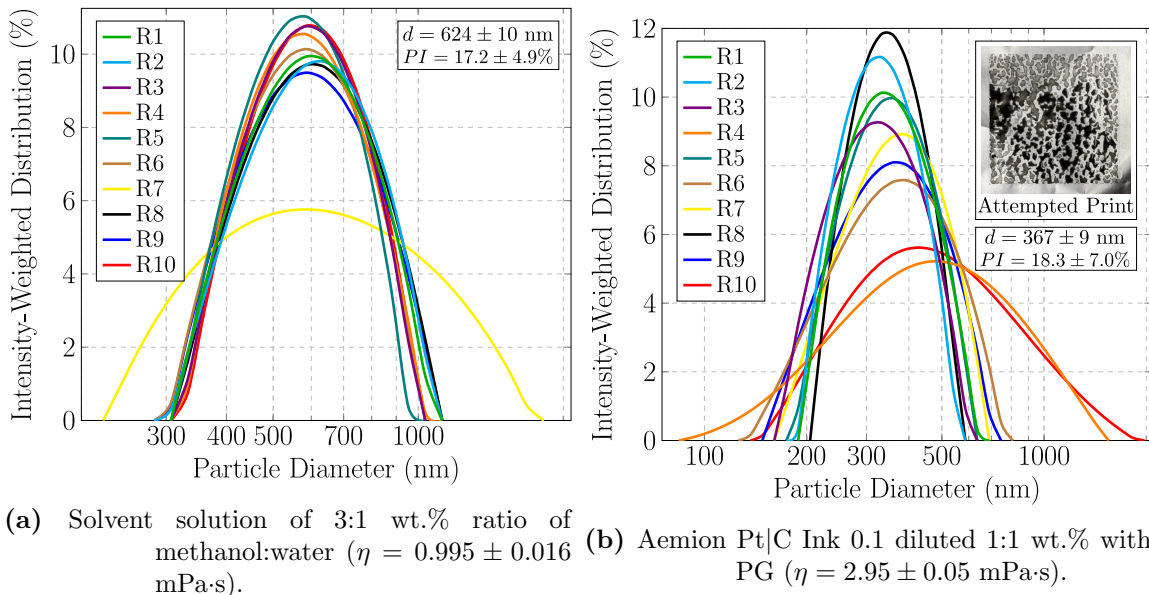


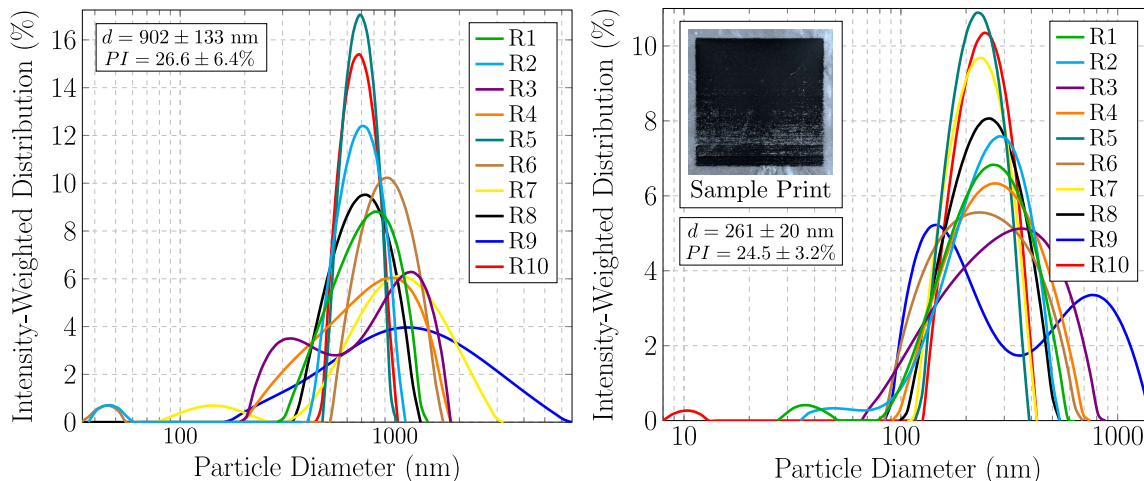
Figure 2.5 – Intensity-weighted particle size distributions obtained from DLS for Aemion Pt|C Ink 0.1. The viscosities for the ink solvent solutions without solid-content were obtained using the Cannon-Fenske viscometer.

Although the viscosity of the ink’s solvent solution was much lower than the Nafion-based baseline (0.995 vs. 5.31 mPa·s), a test print with the DMP-2800 printer verified that the ink was not jettable, presumably due to its low viscosity. To increase the viscosity of the ink it was diluted with PG resulting in a 1:1 wt.% ratio between the existing ink and PG—the resulting particle distributions for the PG-diluted ink are provided in Figure 2.5b. Although the particle distributions obtained for the diluted ink were not as consistent as the non-diluted ink, the ink was found to be jettable using the DMP-2800 printer. However, printing the diluted catalyst ink onto aluminum foil resulted in an apparent puddling of the ink, as seen in the subset of Figure 2.5b, not previously observed with the Nafion-based baseline ink. It was hypothesized that the observed puddling of the ink was due to an excessive amount of PG, and that the PG must be considered in the initial ink recipe as to not add too much. Of note from the results obtained for Aemion Pt|C Ink 0.1 was that a stable catalyst ink compatible with the DMP-2800 printer was produced without using probe sonication.

Aemion Carbon Black Ink 0.1

Due to the relatively high cost of Pt|C catalysts, further Aemion-based ink development was conducted using less expensive carbon black (CB). Using the aforementioned linear system of equations, a new ink recipe was produced with 1 wt.% solid content comprised of 15 wt.% ionomer content, a 3:1 wt.% ratio of methanol:water, and 40 wt.% PG in the solvent solution. The CB-based ink was produced in a similar manner as Aemion Pt|C Ink 0.1, but with CB (TKK Company, Japan) in place of the Pt|C, and PG was added to the ink. The previously produced solution of 5 wt.% Aemion AP1-HNN8 ionomer was again used for Aemion CB Ink 0.1.

As seen in the particle size distributions in Figure 2.6, producing Aemion CB Ink 0.1 with PG added before or after the addition of the Aemion ionomer produced starkly different particle distributions. That is, adding PG before the ionomer (Figure 2.6a) resulted in less consistent particle distributions ($PI = 26.6 \pm 6.4\%$) with a hydrodynamic diameter of 902 ± 133 nm. Conversely, adding PG after the ionomer (Figure 2.6b) yielded more consistent particle distributions ($PI = 24.5 \pm 3.2\%$) with a hydrodynamic diameter of 261 ± 20 nm. Note that each of these samples were tested at different temperatures as a final decision regarding the test temperature had not yet been decided, but that the viscosities were found at the respective DLS test temperatures. As with Aemion Pt|C Ink 0.1, the Aemion CB Ink 0.1 samples were produced without probe sonication, and the sample with PG added after the ionomer was successfully printed using the DMP-2800 printer (sample image provided



(a) PG added before ionomer. Sample tested at 25°C with $\eta = 5.18 \pm 0.09$ mPa·s. (b) PG added after ionomer. Sample tested at 30°C with $\eta = 4.67 \pm 0.08$ mPa·s.

Figure 2.6 – Intensity-weighted particle size distributions obtained from DLS for Aemion CB Ink 0.1. Viscosities for ink samples with solid-content obtained using Zeitzfuchs Cross-Arm viscometer.

in subset of Figure 2.6b). It is hypothesized that the sample produced with PG added after the ionomer produced more favorable DLS results as the ionomer is better able to disperse within a less viscous solution. For context, the viscosity of a 3:1 wt.% ratio of methanol:water was found to be 0.995 ± 0.016 mPa·s while the viscosity of a 3:1 wt.% ratio of methanol:water with 40 wt.% PG was found to be 2.17 ± 0.04 mPa·s at the same test temperature (32°C).

Aemion Pt|C Ink 0.2

Following the promising results obtained for Aemion CB Ink 0.1, a similar ink recipe was used to produce a Pt|C-based ink. As before, 46.7 wt.% Pt|C catalyst (TKK Company, Japan) was used to produce a catalyst ink with 1.25 wt.% solid content comprised of 15 wt.% ionomer content, a 3:1 wt.% ratio of methanol:water, and 40 wt.% PG in the solvent solution. The solvent solution of this ink remained the same as that used for Aemion CB Ink 0.1, but the solid content was increased to 1.25 wt.% as a higher solid content is preferential for producing printed electrodes in a more timely manner. That is, a higher solid content yields more catalyst and ionomer per printed layer, thus requiring less layers to achieve a given catalyst loading. From the learnings obtained from Aemion CB Ink 0.1, the PG was added to the ink after the addition of the Aemion ionomer (5 wt.% solution). As seen in Figure 2.7, the DLS results for the catalyst ink indicate that the ink is stable with a sufficient particle size

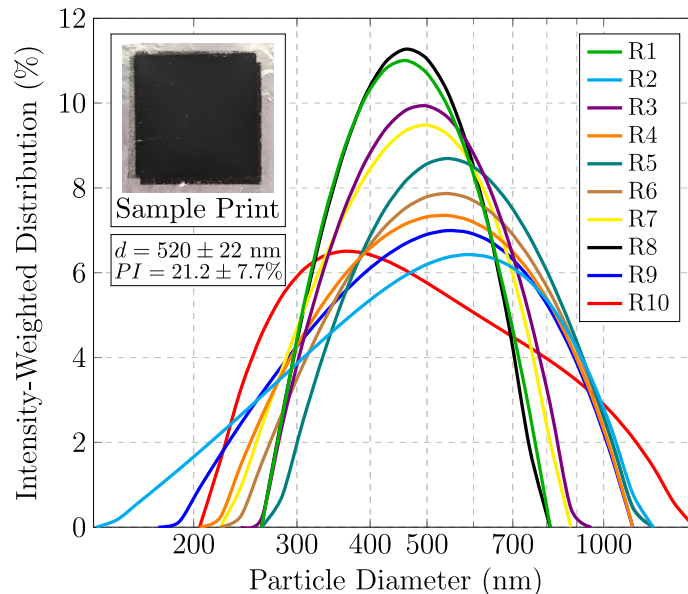


Figure 2.7 – Intensity-weighted particle size distributions obtained from DLS for Aemion Pt|C Ink 0.2. DLS test performed with a viscosity of 2.17 ± 0.04 mPa·s for the ink solvent solution without solid content.

for printing ($d = 520 \pm 22$ nm). This ink was also produced without the use of probe sonication and was successfully used to produce a number of Aemion-based CCMs (electrochemical results for the CCMs provided in Chapter 3).

Aemion Pt|C Ink 0.3

Although Aemion Pt|C Ink 0.2 was successfully used to produce a number of CCMs, the ink was further developed by using a higher wt.% Pt|C and a lower wt.% solution of Aemion ionomer. Moreover, the wt.% of PG in the ink’s solvent solution was increased to 54.2% (corresponding to a molar ratio of 0.3 within the solvent solution) and the methanol in the solvent solution was replaced by IPA. The justification for these changes are as follows:

1. Utilizing a higher wt.% Pt|C:
60 wt.% Pt|C catalyst with Ketjenblack CB (HyPlat, South Africa) was utilized instead of 46.7 wt.% Pt|C as cathodes with higher catalyst loadings were produced, and a higher Pt wt.% catalyst requires less layers to achieve a given catalyst loading.
2. Utilizing a lower wt.% Aemion AP1-HNN8 ionomer solution:
During concurrent catalyst ink development for an Aemion-based IrO_x ink, it was observed that the viscosity of the ionomer solution decreases as the ionomer

wt.% is decreased, which in-turn was favorable for producing consistent catalyst inks. As such, a transition was made to using 2 wt.% Aemion ionomer solutions instead of 5 wt.%. More detail on ionomer solutions is provided in Section 2.2.2.

3. Utilizing a 0.3 molar ratio of PG in the ink solvent solution:

To further increase the viscosity of the inks the PG content was increased to 54.2 wt.% corresponding to a molar ratio of 0.3 within the solvent solution. The molar ratio was chosen from the work of Khattab et al. [92].

4. Utilizing IPA in place of methanol in the ink solvent solution:

Although methanol was still used as the solvent for the ionomer solution, the methanol in the ink solvent solution was changed to IPA since Aemion-based materials (both AP1-HNN8 and AF2-HNN8) are insoluble in IPA. A 3:1 wt.% ratio of alcohol:water was maintained in the solvent solution where the alcohol content includes the IPA and the methanol from the Aemion ionomer solution.

Particle distributions obtained from DLS for Aemion Pt|C Ink 0.3 are provided in Figure 2.8 where Figs. 2.8a and 2.8b demonstrate the difference between a non-probe sonicated and a probe sonicated sample, respectively. For the probe sonicated sample, a lower amplitude was used compared to that used for the baseline Nafion ink (10 vs. 20%), but was sonicated for a longer period of time (30 minutes total vs. 15). Although the effect of probe sonication amplitude and time was not studied

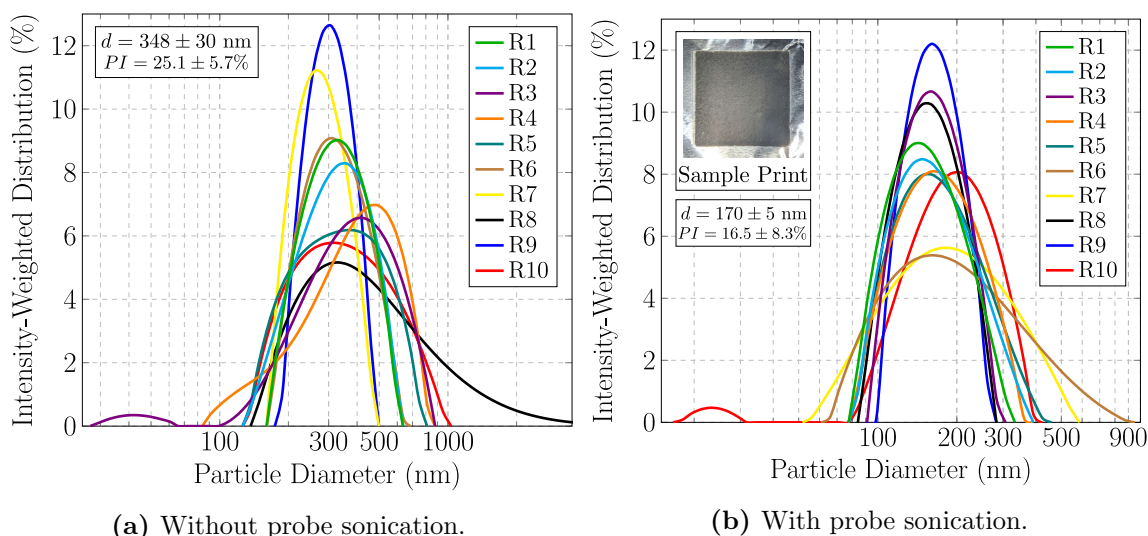


Figure 2.8 – Intensity-weighted particle size distributions obtained from DLS for Aemion Pt|C Ink 0.3. Viscosities of ink samples with solid-content (ionomer only) obtained using Zeitzfuchs Cross-Arm viscometer ($\eta = 9.47 \pm 0.15$ mPa·s).

in depth, it was hypothesized that a lower amplitude would be less impactful on the Pt|C catalyst as it has been demonstrated that higher probe sonication power can decrease the electrochemical surface area (ECSA) of Pt|C-based electrodes in fuel cells [93]. The apparent decrease in the average hydrodynamic diameter particle size from 348 ± 30 nm to 170 ± 5 nm before and after probe sonication, respectively, was qualitatively noted to improve the printability of the catalyst ink and reduce the frequency of nozzle blockages with the DMP-2800 printer.

Since Aemion Pt|C Ink 0.3 was the primary ink used to produce cathode electrodes, the viscosity of the ink was studied more in depth than the other inks. As seen from the summary of viscosity data provided in Table 2.2, the viscosity of the ink recipe without the catalyst, i.e., only the solvent solution and the ionomer, was notably greater than the viscosity of the solvent solution on its own (9.47 vs. 5.23 mPa·s, respectively). Further, the addition of the catalyst only resulted in a slight increase of the viscosity compared to the sample of the solvent solution and ionomer (9.84 vs. 9.47 mPa·s, respectively). Although there was a difference of 2°C between their tests, it was also observed that the viscosity of Aemion CB Ink 0.1 was notably larger than that of its solvent solution (4.67 vs. 2.17 mPa·s, respectively). As such, it may be concluded for the current work that although viscosity data for solvent solutions may be used for approximate DLS tests, viscosity data including the solid content, especially the ionomer, must be considered if more accurate DLS data is desired. Of course this conclusion is strongly contingent on the assumption that the samples exhibit Newtonian behavior and that the tested viscosity matches that of the sample when tested with DLS. As a final consideration regarding viscosity data, recent work by Adamski et al. has demonstrated that the viscosity of Aemion-based solutions may decrease by 15% or more over 30 minutes of bath sonication (42 kHz) [94]. Thus,

Table 2.2 – Summary of density and viscosity data obtained for Aemion Pt|C inks and solvent solutions. Each sample is unique, with the exception of Aemion CB Ink 0.1 which was tested at two temperatures. For the viscometer used, CF = Cannon-Fenske and ZC = Zeitfuchs Cross-arm.

Sample	Viscometer	Temperature (°C)	Density (g/cm ³)	Viscosity (mPa·s)
3:1 water:methanol	CF	32	0.853 ± 0.013	0.995 ± 0.016
3:1 water:methanol w/ 40 wt.% PG	CF	32	0.921 ± 0.015	2.17 ± 0.04
3:1 water:methanol w/ 54.2 wt.% PG	ZC	32	0.937 ± 0.015	5.23 ± 0.08
Aemion CB Ink 0.1	ZC	25 30	0.920 ± 0.015	5.18 ± 0.08 4.67 ± 0.08
Aemion Pt C Ink 0.3 (no catalyst)	ZC	32	0.937 ± 0.015	9.47 ± 0.15
Aemion Pt C Ink 0.3	ZC	32	0.936 ± 0.015	9.84 ± 0.16

small changes in the ink production process may yield notable differences in the ink's viscosity which further propagate to notable differences in DLS results.

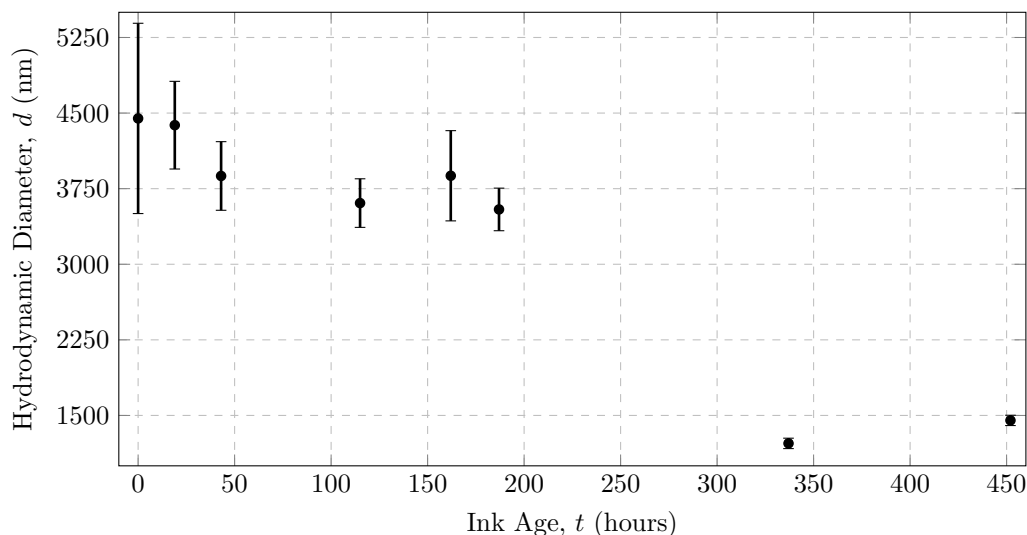
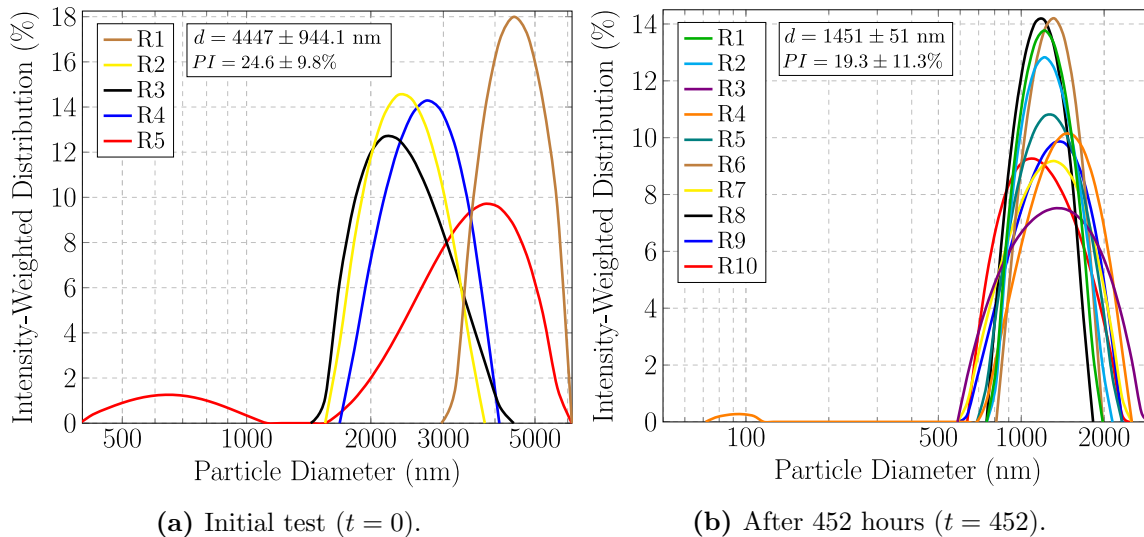
2.2.2 Aemion-Based IrO_x Catalyst Ink

The development of an Aemion-based IrO_x catalyst ink began once Aemion Pt|C Ink 0.2 had been developed since an IrO_x-based ink was then required to produce a complete CCM with a cathode and anode. As a result, learnings obtained from the development of an Aemion-based Pt|C catalyst ink were directly applied for the development of an Aemion-based IrO_x catalyst ink. Additionally, the same system of linear equations used for converting general ink recipes to gravimetric-based recipes was used for this work (refer to Appendix C).

Aemion IrO_x Ink 0.1

An initial Aemion-based IrO_x ink was produced with 6 wt.% solid content comprised of 15 wt.% ionomer content with a solvent solution containing a 3:1 wt.% ratio of methanol:water and 40 wt.% PG. The solid content of the ink was increased above that of the Pt|C-based inks as IrO_x has a higher density than Pt|C. That is, assuming the density of Pt|C to be similar to that of CB since its volume/content is primarily comprised of the CB [95], the density of IrO_x is approximately five-times higher [96, 97]. The catalyst ink was prepared in the same manner as Aemion Pt|C Ink 0.2 with the same 5 wt.% ionomer solution *added before* the PG, but with IrO_x catalyst (TKK Company, Japan) used in place of Pt|C. As with the initial Pt|C-based inks, no probe sonication was used for the initial IrO_x-based ink (only bath sonication during the addition of the ionomer).

Data for the particle size distributions for Aemion IrO_x Ink 0.1 over a period of 452 hours is provided in Figure 2.9. The initial test of the ink provided in Figure 2.9a only contains five DLS repetitions as the other five were rejected due to a poor fit to the experimental data (fit errors of 10⁻³ vs. 10⁻⁴–10⁻⁶ for adequate results). The ink was found to be initially inconsistent with a relatively large particle size ($PI = 24.6 \pm 9.8 \%$, $d = 4.45 \pm 0.94 \mu\text{m}$). However, as seen in Figure 2.9b, after 452 hours on the magnetic stirrer at 350 rpm, the catalyst ink became more consistent and the hydrodynamic diameter greatly reduced ($PI = 19.3 \pm 11.3 \%$, $d = 1.45 \pm 0.05 \mu\text{m}$). Figure 2.9c demonstrates how the hydrodynamic diameter only decreased slightly over the initial 200 hours, but then greatly reduced over the next 150 hours, followed by a slight increase over the remaining 115 hours. Although the particle size of the ink greatly reduced over the test time, the ink was not tested with the DMP-2800



(c) Hydrodynamic diameter of Aemion IrO_x Ink 0.1 as a function of ink age (stored on magnetic stirrer between tests, 350 rpm). Error bars indicate the standard deviation in hydrodynamic diameter obtained from conducting 10 DLS repetitions (with the exception of $t = 0$ where 5 tests were used).

Figure 2.9 – Various DLS results obtained for Aemion IrO_x Ink 0.1 over a period of 452 hours. Data obtained using $\eta = 2.17$ mPa·s for a solvent solution containing a 3:1 wt.% ratio of water:methanol with 40 wt.% PG.

printer since it was deemed that waiting hundreds of hours for a catalyst ink to be usable was not acceptable from a practicality standpoint.

In an effort to determine why the particle distributions within Aemion IrO_x Ink 0.1 were relatively large, the IrO_x catalyst and Aemion ionomer, in the same amounts used for the catalyst ink, were separately tested in a 3:1 wt.% ratio of methanol:water. For the Aemion ionomer sample, a 5 wt.% solution of Aemion ionomer in methanol

was added to the methanol-water solution in the same drop-wise manner as it was added to the catalyst ink. Each of the tested solutions were prepared in the same manner as the catalyst ink, but with the absence of PG and either the ionomer or the catalyst. The resulting particle size distributions for the IrO_x catalyst and Aemion ionomer solutions are provided in Figs. 2.10a and 2.10b, respectively. Since the IrO_x distributions in the solution were relatively small ($d = 172 \pm 2$ nm), and the Aemion ionomer was found to be similar to Aemion IrO_x Ink 0.1 after hundreds of hours (1425 ± 54 vs. 1450 ± 51 nm, respectively), it was concluded that the particle size of the IrO_x ink was dominated by the Aemion ionomer. Furthermore, it was hypothesized that the initial particle size of the catalyst ink was greater than that of just the ionomer in the 3:1 wt.% ratio of methanol:water due to either the addition of the PG, or an interaction between the IrO_x catalyst and the Aemion ionomer (or lack thereof). It was thought that the latter was more probable given that the same solvent solution with PG had been used to produce Aemion Pt|C Ink 0.2 with a hydrodynamic diameter of 520 ± 22 nm. As such, it was hypothesized that if the particle size of the ionomer could be reduced, that the particle size of the IrO_x -based ink would also be reduced.

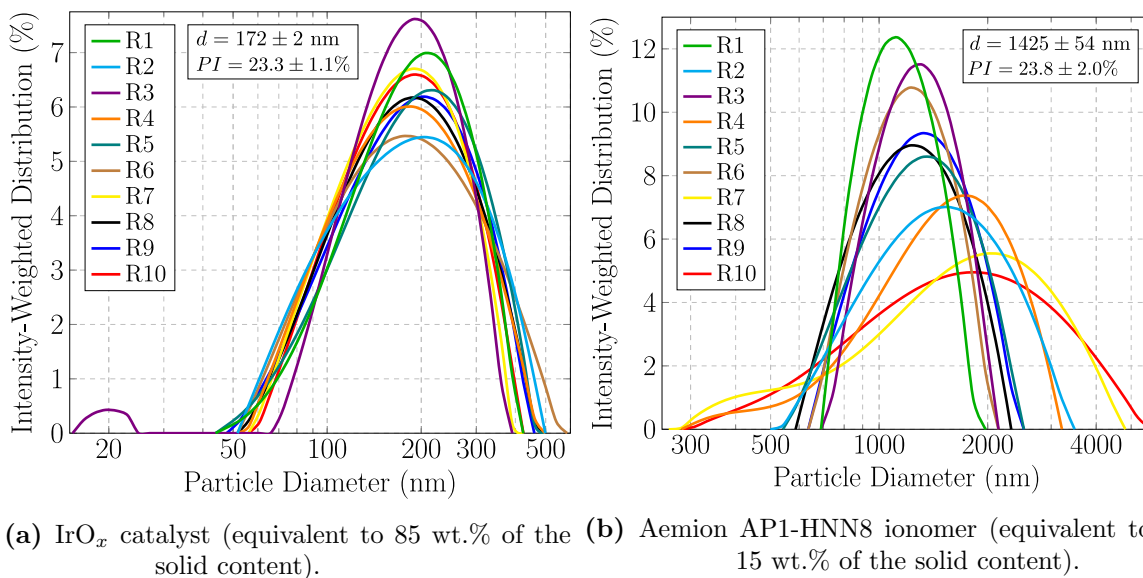


Figure 2.10 – Comparison of intensity-weighted particle distributions of IrO_x and Aemion ionomer in a 3:1 wt.% ratio of methanol:water ($\eta = 0.995$ mPa·s used for both tests).

Aemion IrO_x Ink 0.2

Building on the information obtained from Aemion IrO_x Ink 0.1, a new ink was developed by first studying Aemion AP1-HNN8 ionomer solutions with varying solid content (2–5 wt.%) in methanol. Varying the ionomer wt.% was motivated by the desire to reduce the particle size of the Aemion ionomer solution and the fact that Fortin et al. [57] had utilized a 2.5 wt.% Aemion ionomer solution while Wright et al. [37] used a 10 wt.% solution. Perhaps Fortin et al. had found it beneficial to use a lower wt.% Aemion-based ionomer solution, but did not directly discuss the matter in their work.

DLS data obtained for the various Aemion AP1-HNN8 ionomer solutions is provided in Figure 2.11 where preliminary results obtained using the preset Kalliope settings for a methanol-based sample are provided in Figure 2.11a and updated results with experimentally determined viscosity values are provided in Figure 2.11b. Note that the transmittance data provided in Figure 2.11a is a direct measurement of how much light passes through the sample relative to the incident light. Based upon the increasing transmittance and decreasing apparent particle size with decreasing wt.% in Figure 2.11a, it was initially concluded that the lower the wt.%, the more dissolved and dispersed the ionomer is within the methanol. Moreover, the relatively large hydrodynamic diameters for the ionomer solutions of 2–4 μm were thought to be an apparent particle size representing the size of the Aemion polymer chain. However, upon testing the viscosity of the various ionomer solutions with the

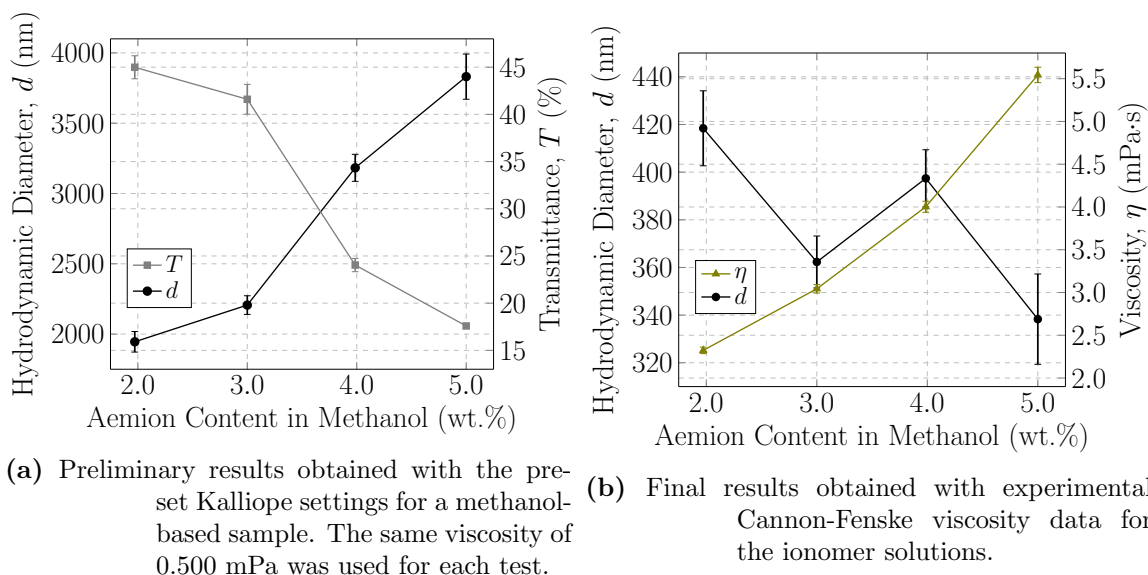


Figure 2.11 – Comparison of DLS results obtained for Aemion AP1-HNN8 ionomer solutions with varying solid content.

Cannon-Fenske viscometer, it was found that the viscosity notably increased from 2.32 ± 0.04 mPa·s for a 2 wt.% solution to 5.54 ± 0.09 mPa·s for a 5 wt.% solution. As seen in Figure 2.11b, the recalculated particle sizes for the ionomer solutions using the experimental viscosities were all relatively similar varying by as little as 50 nm. This result demonstrated the importance of using sample-specific viscosities when performing DLS experiments.

Although the particle size of the Aemion ionomer was not actually reduced by decreasing the solution solid-content, an IrO_x-based catalyst ink with 5 wt.% solid content comprised of 15 wt.% ionomer and a solvent solution with a 3:1 wt.% ratio of methanol:water and 40 wt.% PG was produced using a 2 wt.% Aemion ionomer solution. The solid content of the ink, termed Aemion IrO_x Ink 0.2, was decreased to 5 wt.% from 6 wt.% to match the solid content of the Nafion-based IrO_x catalyst ink commonly used by M. Mandal to produce inkjet printed anodes for PEM-based electrolyzers [33]. The resulting particle distributions for Aemion IrO_x Ink 0.2 after 21 hours atop the magnetic stirrer (350 rpm) is provided in Figure 2.12. Compared to Aemion IrO_x Ink 0.1 with an age of 452 hours, the new ink had a lower hydrodynamic diameter (1320 ± 42 vs. 1451 ± 51 nm, respectively), and was more consistent (*PI* of 15.7 ± 7.2 vs. $19.3 \pm 11.3\%$, respectively). Thus, although the particle size of Aemion IrO_x Ink 0.2 was not reduced to the size of the baseline Nafion Pt|C ink (258 ± 46 nm), or even Aemion Pt|C Ink 0.2 (520 ± 22 nm), the ink was better suited

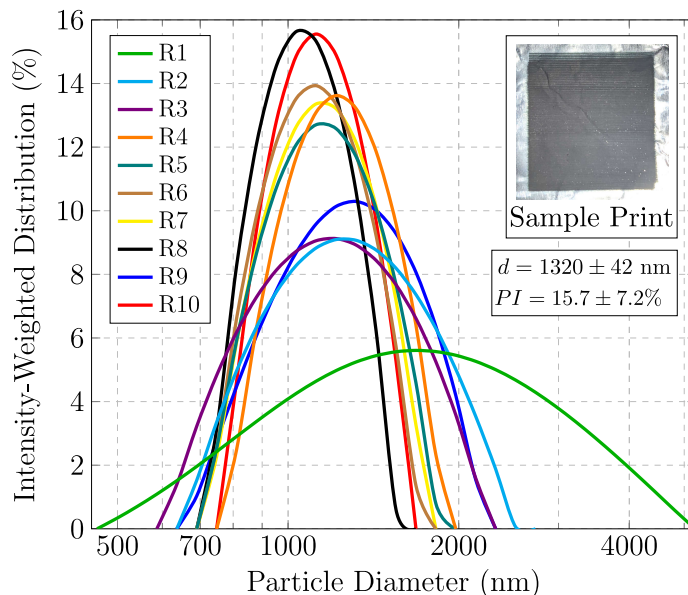


Figure 2.12 – Intensity-weighted particle size distributions obtained from DLS for Aemion IrO_x Ink 0.2. DLS test performed with a viscosity of 2.17 ± 0.04 mPa·s for the ink solvent solution without solid content.

for printing than Aemion IrO_x 0.1 and could be produced in a timely manner. This ink was successfully used to produce a number of Aemion-based CCMs (electrochemical results for the CCMs provided in Chapter 3) with a sample print image provided in the subset of Figure 2.12.

Aemion IrO_x Ink 0.3

Although Aemion IrO_x Ink 0.2 was successfully used to produce a number of CCMs, two primary issues were encountered with the ink:

1. The relatively large particle size of the ink and/or its high solid content resulted in many of the DPM-2800 printer cartridge nozzles being blocked during the printing process.
2. Using a 2 wt.% Aemion ionomer solution resulted in too much methanol in the catalyst ink such that pinholes were observed to form in the Aemion membrane during CCM fabrication (even if the solid content of the ink was < 5% and the methanol in the ink's solvent solution was replaced with IPA).

As such, a new catalyst ink was produced with 3.5 wt.% solid content comprised of 15 wt.% ionomer with a solvent solution containing a 3:1 wt.% ratio of alcohol:water and 54.2 wt.% PG. The ink was produced using a 4 wt.% Aemion ionomer solution such that the overall methanol content in the ink solvent solution was maintained below 15 wt.% (4 wt.% was thought to be preferential to 5 wt.% as it has a lower viscosity). For reference, the Aemion IrO_x catalyst ink that resulted in pinholes in the membrane contained 25 wt.% methanol in the solvent solution. In addition to lowering the ink solid content, increasing the PG content, and using a different wt.% ionomer solution, the primary alcohol in the ink was also changed to IPA as was done for Aemion Pt|C Ink 0.3. Also as with Aemion Pt|C Ink 0.3, the IrO_x-based ink was probe sonicated (10% amplitude, 1 minute on, 1.5 minutes off, 30 minutes total sonication) as it was qualitatively found to decrease the frequency of nozzle blockages with the DMP-2800 printer.

This ink, and slight variations of it, were used to produce a number of inkjet printed anodes for CCM fabrication. For the variations, the ink preparation method and ink recipe primarily remained the same, but the solid content was adjusted ($\pm 1\%$) depending on the printability of the ink. That is, depending on the batch of printer cartridge heads from Fujifilm, a 3.5 wt.% solid content could be used (Figure 2.13a), or a lower wt.% such as 2.5 wt.% (Figure 2.13b) was required.

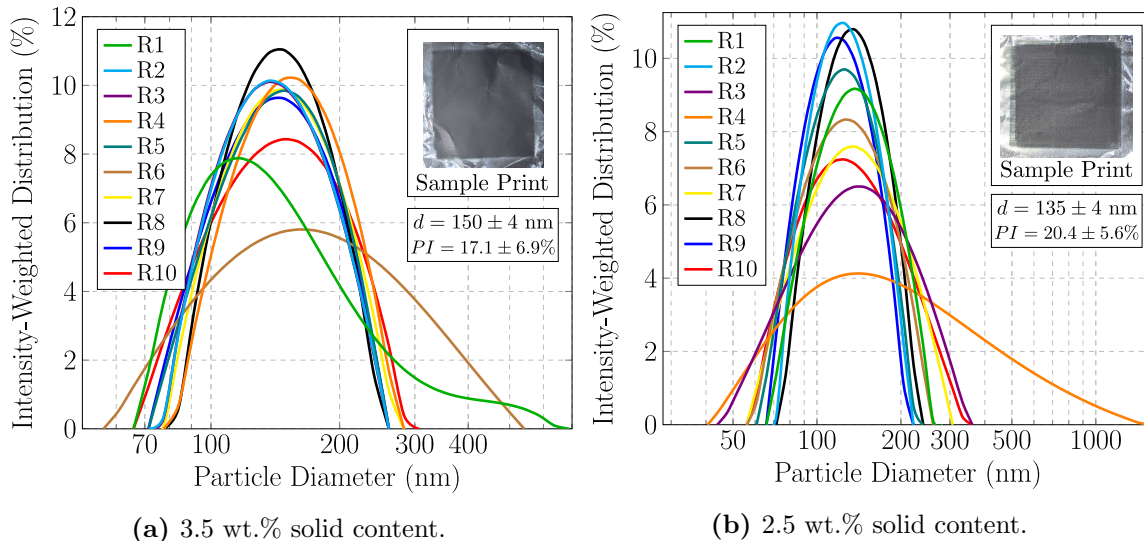


Figure 2.13 – Intensity-weighted particle size distributions for Aemion IrO_x Ink 0.3 ($\eta = 9.47$ mPa·s used for both tests).

2.2.3 Summary of Developed Catalyst Inks

The final recipes and corresponding properties for the catalyst inks developed as part of this work are compared to the Nafion-based baseline ink in Table 2.3. The densities of the developed inks are greater than the Nafion-based baseline owing to the use of a higher PG content and the inclusion of water. The increased viscosity of the Aemion-based inks may be due to the specific properties of the Aemion AP1-HNN8 vs. Nafion ionomers and the use of an increased PG content. By using low wt.% solutions of the Aemion ionomer (< 5 wt.%) and adding PG to the catalyst ink solution after the addition of the ionomer, the average particle size within the developed inks was found to be similar to that of the Nafion-based baseline ink. As such, this work has demonstrated that catalyst ink consistency and particle size reduction may be improved by dispersing the ionomer within a catalyst solution with a relatively low viscosity. Stated otherwise, one should ensure that the viscosity of both the ionomer solution and the catalyst slurry are both as low as possible prior to the addition of the ionomer to the catalyst ink. Lastly, this work has demonstrated the usefulness of DLS as a tool for both catalyst ink characterization and development.

Table 2.3 – Final Pt|C and IrO_x catalyst ink recipes and their corresponding characteristics.

Property	Nafion Baseline	Pt C Ink 0.3	IrO _x Ink 0.3
wt.% of total solid content	1.36	1.25	3.5
wt.% of solid-phase ionomer content	15	15	15
alcohol to water ratio in solvent solution	— ^a	3	3
wt.% of PG in solvent solution	47	54	54
wt.% of ionomer solution used	5	2	4
Density, ρ (g/cm ³) ^b	0.885±0.014	0.936±0.015	0.959±0.023
Dynamic Viscosity, η (mPa·s) ^b	5.31±0.09	9.85±0.16	10.5±0.3
Hydrodynamic diameter, d (nm) ^c	258±46	348±30	150±4
Polydispersity Index, PI (%) ^c	22.9±4.7	25.1±5.7	17.1±6.9
Particle Distribution ^c	Fig. 2.4	Fig. 2.8a	Fig. 2.13a

^a The solvent solution for the Nafion-based baseline Pt|C ink developed by S.Shukla [98] did not contain water, and was instead comprised of 47 wt.% PG, 48 wt.% IPA, and the remaining wt.% was comprised of the solvent solution for the ionomer used

^b The reported density and viscosity values were found using the Zeitfuchs Cross-arm viscometer for the catalyst inks including the solid-content components (catalysts and ionomer)

^c The referenced particle size distributions for the developed Aemion-based Pt|C and IrO_x catalyst inks were found using $\eta = 9.47 \pm 15$ mPa·s, which is the viscosity of the ink solvent solution with 15 wt.% ionomer content

Chapter 3

Electrode Fabrication and Electrolyzer Testing

Following the development of Aemion-based Pt|C and IrO_x catalyst inks usable for inkjet printing electrodes, the remaining secondary goals of the current work were completed herein: the development of a test-station for testing AEM-based electrolyzers, as well as electrode fabrication and cell assembly/testing.

3.1 Methodologies for Electrode Fabrication and Electrolyzer Testing

The development of the test-station for operating AEM-based electrolyzers is separated into a section on the physical hardware (Section 3.1.1) and a section on the in-house developed software used for performing experiments (Section 3.1.2). Information regarding the test-station is followed by sections on CCM fabrication using inkjet printing (Section 3.1.3) and electrolyzer cell assembly (Section 3.1.4). Lastly, the methodologies used for performing polarization curve, stability, and electrochemical impedance spectroscopy experiments are covered in Sections 3.1.5 and 3.1.6, respectively.

3.1.1 Electrolyzer Test-Station Hardware

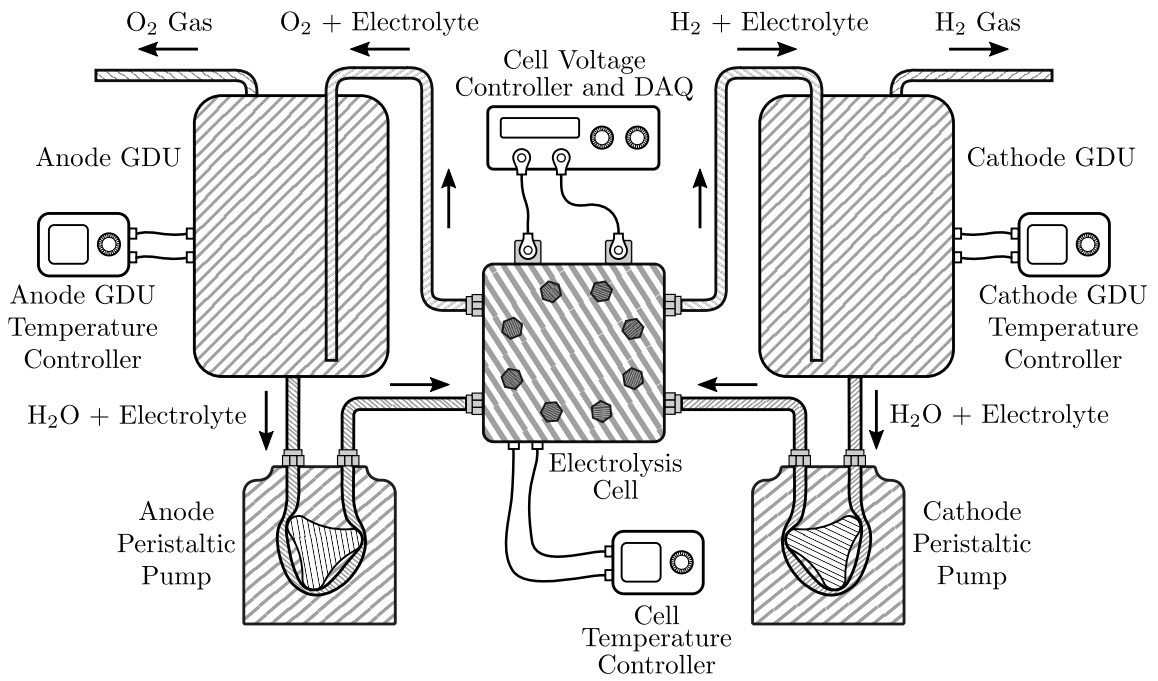
As per the operation of AEM-based electrolyzers discussed in Section 1.3.3, to test an electrolyzer cell there are a number of requirements:

- ◇ the cell must be fed with DI water or a caustic electrolyte such as aqueous KOH,
- ◇ the liquid fed to the cell, as well as the cell itself, must be heated to temperatures < 100°C,

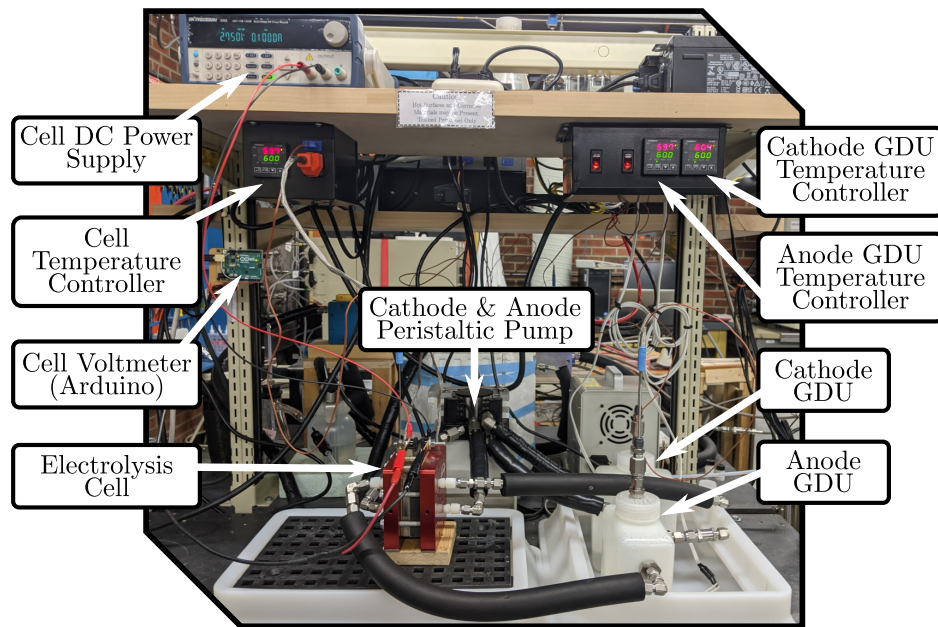
- ◇ the cell must be powered using a direct current (DC) power supply,
- ◇ the cell and cell feed must be isolated from the ambient atmosphere such that CO₂ cannot enter the system,
- ◇ the produced oxygen and hydrogen gases must be separated from the circulated feed liquid, and
- ◇ the current/voltage data must be acquired and recorded.

To satisfy these requirements, a test-station, as shown in Figure 3.1, was developed and built in-house. A schematic of the test-station is provided in Figure 3.1a while an annotated picture is provided in Figure 3.1b.

As an overview, the gas disengagement units (GDUs) function to both store and heat the feed liquid for the test-station, and function as two-phase gas-liquid separation units. The GDUs were designed and assembled in-house with more details on their design provided in Appendix A.3. The liquid stored within the GDUs is circulated to the electrolysis cell via a peristaltic pump. The peristaltic pump utilized (Gilson Minipuls 3) has a multi-channel head configuration such that all three feed methods are possible with the system (anode only, cathode only, or both anode and cathode). The multiphase gas-liquid mixtures leaving the electrolysis cell flow back to the GDU units wherein the gas is bubbled through the liquid in the GDU and leaves the system to ventilation through one-way low pressure differential check valves (1/3 psig cracking pressure). Oxygen from the anode GDU exits the system through the check valve to the ambient atmosphere while hydrogen from the cathode GDU exits the system through the check valve to lab ventilation. A calibration of the peristaltic pump flow rate yielded $\dot{V} = 0.175N_\omega \pm 0.3$ where \dot{V} is the resulting flow rate in mL/min (per electrode stream) and N_ω is the speed of the Gilson Minipuls 3 pump head in rpm. A detailed description of the experiment used to obtain the aforementioned flow rate expression and corresponding uncertainty is provided in Appendix B.5. Heat for the GDUs and electrolysis cell is provided via ohmic heaters controlled with in-house designed temperature control boxes that utilize a PID (more detail provided in Appendix A.1). The type-T thermocouples used for the test-station have a tolerance of $\pm 1^\circ\text{C}$ as per ASTM E230 [99]. Power for the system is provided using a DC power supply (B&K Precision 9202) controlled by an in-house developed software. The in-house developed software also provides current and voltage data acquisition (DAQ) for the system using an Arduino (more detail provided in Section 3.1.2).



(a) Schematic of test-station.



(b) Annotated picture of test-station.

Figure 3.1 – Test-station developed for conducting experiments with AEM-based electrolyzers. GDU = gas disengagement unit used for two-phase gas-liquid separation.

Wetted materials for the test-station were limited to high density polyethylene (HDPE), 316 stainless steel (316 SS), polytetrafluoroethylene (PTFE), EPDM, and nitrile (Buna-N). These materials were selected as they are reported to be stable when in contact with both aqueous KOH [100, 101] and hydrogen gas [102, 103]. Since the PVC-based tubing commonly used with the Gilson Minipuls 3 pump had been noted to mechanically break down when operated with deionized water for performing PEM-based water electrolysis experiments, and PVC is reported to only be stable in 2 mol/L KOH up to a temperature of 60°C [101], the peristaltic pump tubing was changed to a Norprene-based tubing from McMaster-Carr¹ (#51075K21). The two tubing materials were compared by using them to operate a PEM-based water electrolyzer with results provided in Section 3.2.2. In a study of the corrosion behavior of stainless steels in ≈ 6 mol/L KOH, a temperature of 130°C, and a pressure of 2.9 MPa, it was found that steels such as 316 SS generally show poor corrosion resistance. As a result, the report suggested that 316 SS be monitored diligently in long term operation with solutions of aqueous KOH and to ensure the operating temperature does not exceed 120°C. It was hypothesized, however, that since the operating parameters for the current work (≤ 1 mol/L KOH, $\leq 80^\circ\text{C}$, and \approx atmospheric pressure) are well below those for the reported study, that the 316 SS used for the GDU immersion heaters and tubing fittings would be corrosion resistant. For an additional level of safety for operation with solutions of aqueous KOH the electrolyzer cell and GDUs were kept within an HDPE secondary containment in case of a spill. In an effort to maintain the temperature of the feed liquid to the cell from the GDUs, all PTFE tubing connecting the various components was insulated with Buna-N/PVC foam insulation (R-value of 2).

3.1.2 Electrolyzer Test-Station Software

To perform galvanostatic and potentiostatic experiments with the AEM-based electrolyzer test-station a software was developed to control the station’s DC power supply and record current/voltage data. Front-end development for the software’s graphical user interface (GUI) was completed using the Qt Designer application (version 5.9.7) and back-end development was completed with the PyQt5 package (version 5.14.1) within Python (version 3.7.4).

A flow diagram illustrating how the software performs an experiment is provided in Figure 3.2. As indicated in the flow diagram, when an experiment is started the

¹No information regarding the chemical compatibility of Norprene with solutions of aqueous KOH is available in the DECHEMA KOH Corrosion Handbook [101], but it was selected as it “has the chemical resistance to withstand a variety of acids and other harsh substances” [104].

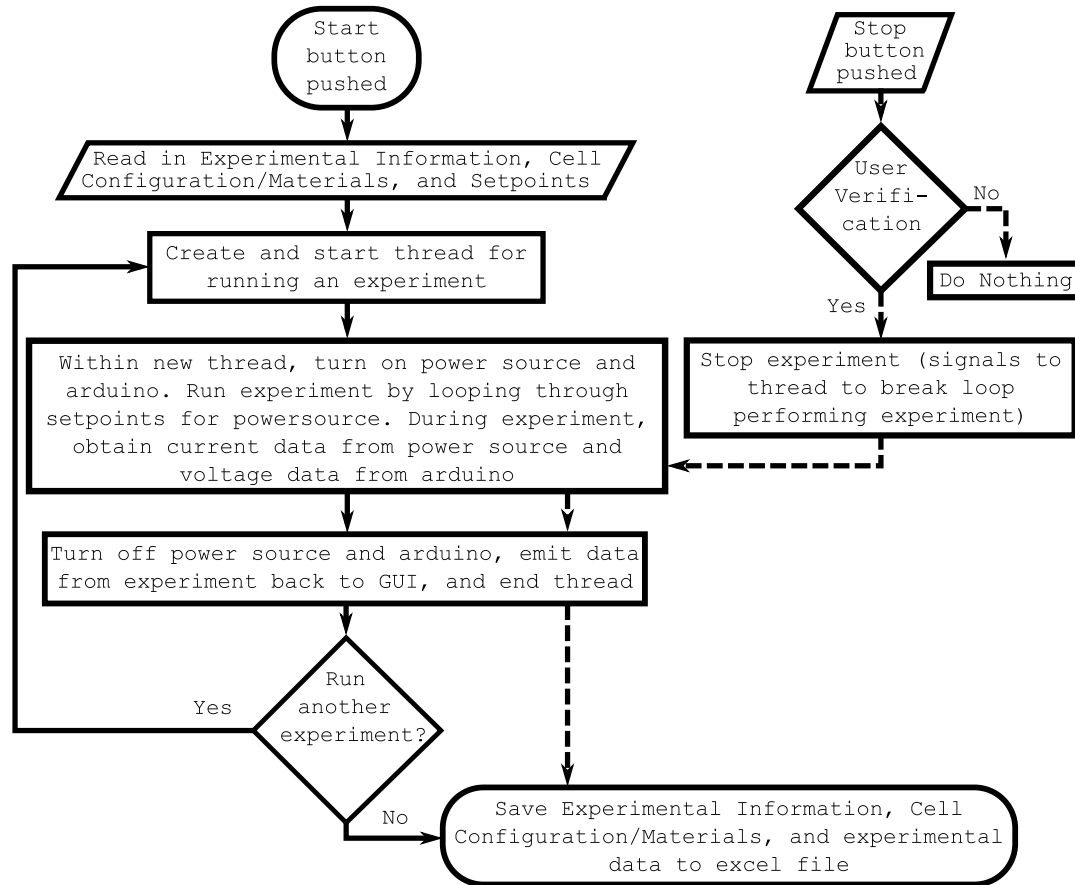


Figure 3.2 – Flow diagram illustrating how the test-station software performs an experiment. Note that the software's main GUI thread runs simultaneously as the process above but is not pictured.

information within the GUI is read and a 'worker' thread is initiated to run the experiment. Within the worker thread, the power source (B&K Precision 9202) and Arduino (Arduino UNO SMD R3) are communicated with and the experiment is conducted by looping through the setpoints passed from the GUI. Throughout the experiment, current values are obtained directly from the power source while voltage values are obtained from the Arduino. Voltage values obtained from the Arduino were verified to be within ± 1 mV using a Fluke true-RMS 287 multimeter. Although voltage data could be obtained from the power source (as is done for the current), the Arduino is used to directly obtain voltage data at the cell to eliminate inaccuracies caused by the voltage drop through the power source current leads connected to the cell. Once all setpoints for the experiment have been looped through, the power source and Arduino are set to non-operational within the worker thread, the worker thread emits the data obtained back to the software's main thread, and the main thread ends the worker thread. The decision is then made whether to conduct another

experimental iteration² or not. In case of the latter, all experimental information obtained from the GUI, as well as the experimental data obtained, is saved to an Excel file. At any time during an experiment the experiment may be terminated and the data obtained up until that point is saved to an Excel file.

3.1.3 Catalyst Coated Membrane Fabrication

Using the Pt|C and IrO_x catalyst inks developed in Chapter 2, AEM-based CCMs were fabricated using inkjet printing. The equipment used for the printing process is demonstrated in Figure 3.3. The printing process used was based upon the work of S. Shukla [98] and Mandal et al. [33]. More specifically, a commercial inkjet material printer (Dimatix DPM-2800 series, Fujifilm) was used with cartridge heads containing 16 nozzles (21 μm diameter) spaced 254 μm apart that produce 10 pL droplets. An



Figure 3.3 – Equipment used for inkjet printing CCMs.

²If, for instance, multiple polarization curve tests are conducted consecutively.

image of the Dimatix printer is provided in Figure 3.3a while the cartridge (1.5 mL volume) and cartridge head are provided in Figure 3.3b. During the printing process the cartridge head prints along the x -axis shown in Figure 3.3c, resets to $x = 0$ once it has traversed the required distance, shifts down the y -axis, prints along the x -axis again, and continues on in the same manner until the desired area has been printed. The catalyst loadings of the CCM CLs, as discussed in Section 1.3.2, were controlled by the number of layers printed onto the membrane. Three CCMs with a geometric area of 5 cm^2 were commonly produced simultaneously with an additional CL printed onto a piece of aluminum foil. The CL printed onto the aluminum foil was used to measure the catalyst loading by measuring its change in mass during the printing process. The catalyst loading was determined using the following formula,

$$\text{catalyst loading (mg}_{\text{catalyst}}/\text{cm}^2) = \frac{\Delta m (1 - wt_{\text{inkInmr}}) wt_{\text{ctlst}}}{A} \quad (3.1)$$

where

Δm is the change in mass measured from the aluminum foil, mg,

wt_{inkInmr} is the ionomer content within the catalyst ink, wt.%,

wt_{ctlst} is the catalyst loading on the support if a supported catalyst, such as Pt|C, is used, wt.%, and

A is the geometric area printed on the aluminum foil, cm^2 .

Note that catalyst inks with IrO_x have no support such that wt_{ctlst} simply becomes unity.

In the work by S. Shukla [98] and Mandal et al. [33], the Nafion membrane and aluminum foil were held in place during the printing process using the printers built-in vacuum platen. For the current work, however, it was found that the swelling of the AEMs was too great to be held in place using the printers vacuum platen. As such, a stainless steel plate, as shown in Figure 3.3c, was developed to hold the AEMs in place during the printing process. The printers platen was also maintained at 60°C during the printing process to increase the evaporation rate of the solvent printed onto the membranes.

Due to the possibility of Pt poisoning from iodide [106], the Aemion AF1-HNN8-50 membrane was converted from its as-received iodide form to chloride form prior to CCM fabrication. The Aemion AF1-HNN8-50 membrane was cut into individual 1.75×1.75 inch square pieces and converted to chloride form by placing them into

a plastic container (HDPE) with a gasketed lid containing 300 mL of 1 mol/L aqueous KCl (Sigma-Aldrich, P3911, $\geq 99\%$). A plastic plate was submerged into the container to lightly sandwich the membrane against the bottom of the container to ensure the membrane remained relatively flat during the conversion process—this was done to ease the handling of the membrane as otherwise it would roll up as it swelled due to the water. With a magnetic stirrer added to the container to help facilitate the exchange of ions, the sealed container was left atop the magnetic stirrer platform (≤ 150 rpm) for a minimum of 20 hours. The complete conversion of the membrane to chloride form from iodide form was not confirmed such that the membrane pieces may have been in a mixed chloride-iodide form. A schematic illustrating how the membrane pieces were loaded into the container setup used for the conversion process is provided in Figure 3.4. Following the conversion of the membrane to the apparent chloride form, the membrane pieces were rinsed using degassed deionized water to remove any excess KCl salt.

After the membrane pieces had been converted and rinsed, they were mounted into the printer as demonstrated in Figure 3.3c, and the cathodes were printed. Due to swelling and dimensional changes of the membrane during the printing process,

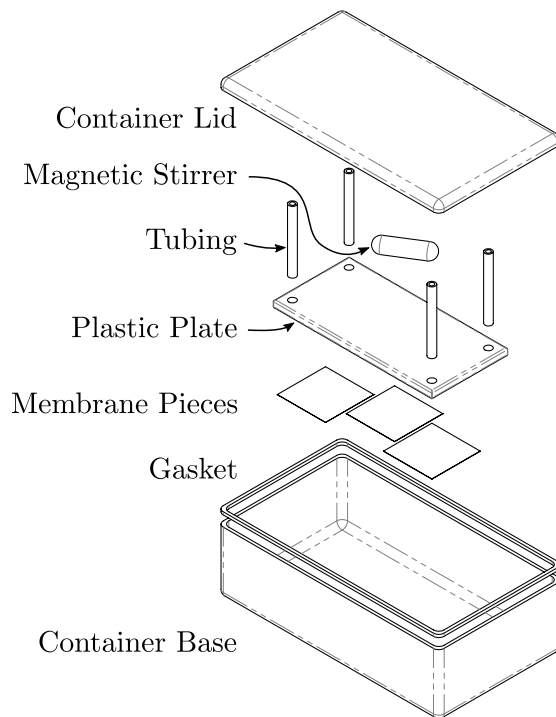


Figure 3.4 – Exploded schematic illustrating how AEMs were held flat during the conversion process. Note that the lid contained built in clips that clamped it to the base (not shown in schematic).

the area printed for the cathodes was increased 15% above 5 cm² (24.0 x 24.0 mm instead of 22.4 x 22.4 mm) so that the anodes, which were printed as 5 cm², could be more easily printed to cover the area of the cathodes—this concept is illustrated in Figure 3.5. Note that this concept is not demonstrated with a photograph because the increased electrode size of 2.56 mm² is difficult to discern as the AEMs commonly wrinkled as a result of the printing process (CCM images are provided in Section 3.2). The cathodes were over printed instead of the anodes since the cathode catalyst loadings were generally much lower than the anode catalyst loadings, and therefore required much less time to print, even with an increased size. Once the desired catalyst loading had been achieved, the CCMs were removed from the printer, covered for protection against debris such as dust, and allowed to dry for a minimum of 12 hours. Following the drying process, the cathode electrodes were imaged using a transmitting optical microscope (Micromaster, BS200, Fisher Scientific) and analyzed for any surface defects. The anodes were then printed on the opposite side of the membrane with the desired loading, allowed to dry in the same manner as the cathodes, and imaged using a stereoscopic microscope (Leica S8 APO). The completed CCMs were then either used for testing, or carefully stored between sheets of paper within a plastic bag with a detailed label for later testing.

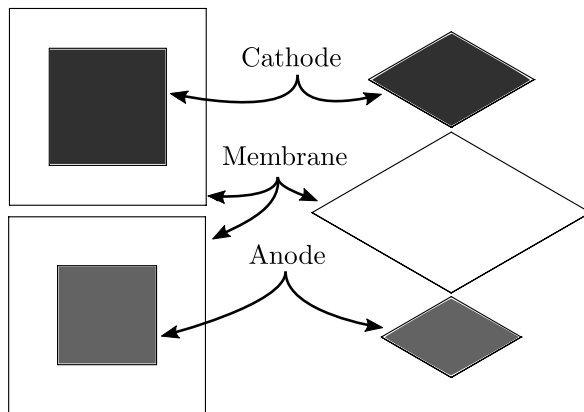
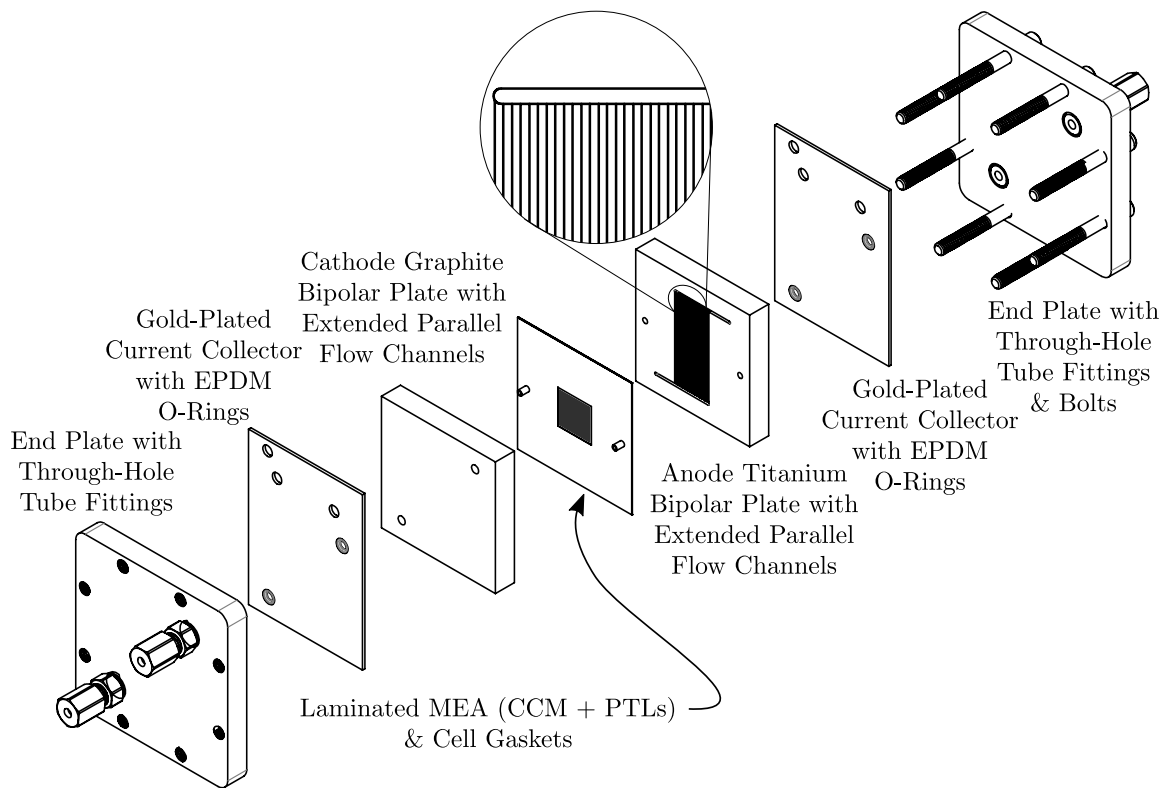


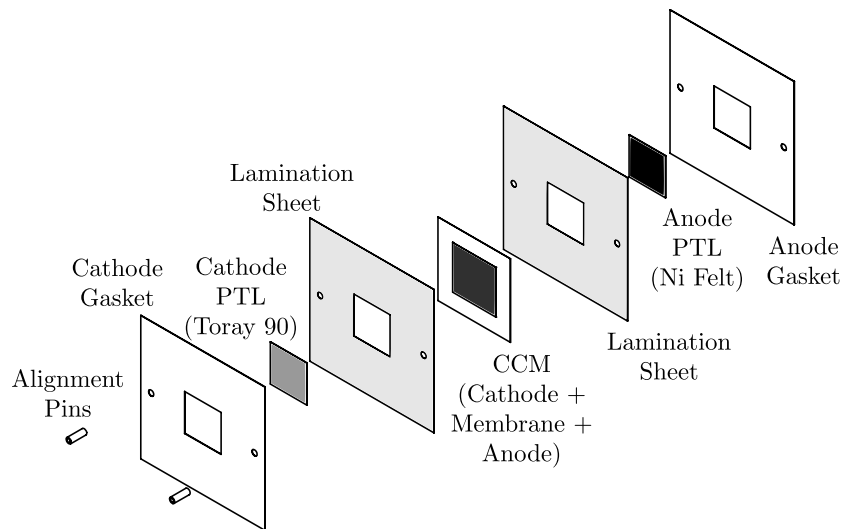
Figure 3.5 – Schematic of a single CCM with an oversized cathode.

3.1.4 Electrolyzer Cell Assembly

The fabricated CCMs were assembled into electrolyzer cells following the arrangement illustrated in Figure 3.6 where Figure 3.6a is an exploded view of the general cell hardware and Figure 3.6b is an exploded view of the MEA and cell gaskets. Unless otherwise stated, the cells were assembled with the components listed in Table 3.1. The bipolar plates used for the current work were fabricated in-house with parallel



(a) General cell hardware with zoomed in view of the bipolar plate's parallel flow channels.



(b) Laminated MEA with gaskets and assembly alignment pins.

Figure 3.6 – Exploded schematics illustrating the assembly of AEM-based electrolyzer.

Table 3.1 – Cell materials used for assembling AEM-based electrolyzers.

Component	Material Used
End Plates	Liquid-Compatible Plates from Scribner Associates
Current Collectors	Gold-Plated Copper from Scribner Associates
Cathode Bipolar Plate	Graphite with Extended Parallel Flow Channels
Anode Bipolar Plate	Titanium with Extended Parallel Flow Channels
Gaskets	Compressible PTFE Sheet
Cathode PTL	Toray 90 from Fuel Cell Store (TGP-H-90)
Anode PTL	Bekipor Nickel from Bekaert (2Ni 18-0.25)

channels extending beyond the active area of the CCM—detailed drawings for the plates are provided in Appendix A.4. The CCMs were laminated using conventional 3 mil ($\approx 75 \mu\text{m}$) thick lamination sheets with a square cutout removed from where the sheets would otherwise overlap the CLs of the CCM. Small $1/8^{\text{th}}$ inch holes added to the laminated CCMs aided in assembling cells as alignment pins passed through holes in the laminated CCMs, cell gaskets, and the bipolar plates for each electrode. Unless otherwise stated, the laminated CCMs were converted to hydroxide form using 0.85 mol/L aqueous KOH (Sigma-Aldrich, #221473, $\geq 85\%$ ($\leq 2\%$ K_2CO_3 and 10–15% water)) following the same procedure used to convert the membrane to chloride form (but with aqueous KOH instead of KCl) as discussed in Section 3.1.3. As with the membranes converted to chloride form, the converted CCMs were rinsed with degassed deionized water to remove any excess salt.

The cell end plates procured from Scribner Associates came fabricated with national pipe thread (NPT) holes such that through-hole tube fittings were added to the plates. The use of the through-hole tube fittings allowed for PTFE tubing to pass directly through the cell end plates and current collectors directly into the bipolar plates. As such, the materials of the end plates and current collectors, which may be susceptible to corrosion from KOH fed to the cell, were not wetted during cell operation.

Liquid and gas transported in and out of the cell through PTFE tubing was sealed into the cell using EPDM rubber o-rings situated in the current collectors and PTFE gaskets sandwiched between the laminated CCM and the bipolar plate of each electrode. As with the lamination sheets, the cell gaskets had 5 cm^2 cutouts removed from the center where they would otherwise overlap with the printed electrodes. The compression of the PTLs and electrodes was controlled by changing the thickness of the gaskets and using a sufficient amount of torque for the cell bolts during cell assembly. Using gaskets of different thicknesses changed the pinch of the cell MEA, which

is defined as the difference between the total gasket + lamination sheet thickness and the cumulative thickness of the CCM and the PTLs,

$$\text{Pinch} = [\text{cathode CL} + \text{anode CL} + \text{cathode PTL} + \text{anode PTL}] - [\text{cathode gasket} + \text{anode gasket} + 2(\text{lamination sheet})]. \quad (3.2)$$

With a positive pinch value, as demonstrated schematically in Figure 3.7, the MEA is compressed the pinch amount during cell assembly as the two total thicknesses are equalized by the planar bipolar plates. For the current work, a pinch of 50 μm was used, the lamination sheets were each 75 μm thick, the electrodes were each assumed to be 2 μm thick based upon Ref. [33], and the cathode and anode PTLs were 280 and 275 μm thick, respectively. As such, gaskets with a thickness of 180 μm (7 mils) were used based upon the calculation from Eq. (3.2).

Based upon the work of others within the Energy Systems Design Laboratory (ESDLab) at the University of Alberta, a torque of 50 in·lb was applied to each of the cell bolts in a star-like pattern. The homogeneous compression of the MEA within the cell was qualitatively checked using a two-sheet pressure measurement film (Prescale LLW, Fujifilm). As explained by J. Kracher [107], the raised edges of the flow field channels should be subtly visible in the pressure film such that the compression of the CLs and PTLs is not too low or too high—this is demonstrated in Figure 3.8. If the compression is too high, then the porosity within the PTLs and CLs may be too low and limit mass transport within the cell. Conversely, if the compression is too low, then higher contact resistances between the MEA components will lead to higher ohmic losses [107].

The PTFE gaskets commonly used were compressible (Rockwell R58 minimum hardness [108]) and made up of two sheets of different thicknesses to obtain the desired overall thickness (for each electrode). Other gasket materials such as Kapton

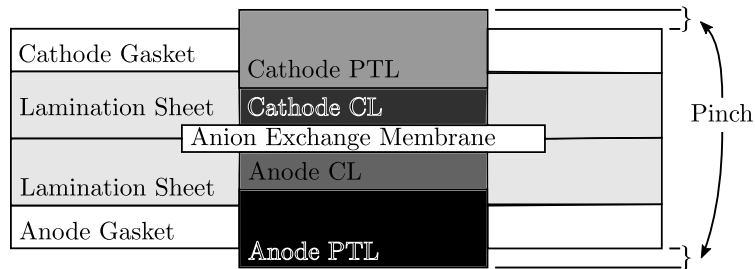


Figure 3.7 – Cross-sectional schematic of gasketed MEA demonstrating the concept of pinch. Note that the pinch calculation, as per Eq. (3.2), does not include the membrane thickness since the membrane is present in both calculated thicknesses.



Figure 3.8 – Pressure film measurement demonstrating proper compression of the MEA and sealant of the cell.

polyimide and PTFE-coated fiberglass were used for select tests. The PTFE-coated fiberglass gaskets were used for limited testing as only select thicknesses were available.

3.1.5 Polarization Curves and Stability Testing

Cell polarization curve and short-term stability experiments (< 10 hours) were conducted using the AEM-based electrolyzer test-station hardware and software described in Sections 3.1.1 and 3.1.2. Polarization curve experiments were conducted first to determine the performance of the cells, and stability experiments were conducted thereafter for select higher performing cells. During the experiments the cells were operated at 60°C and fed with solutions of 0.85 mol/L KOH (also at 60°C) to both the anode and cathode electrodes at a flow rate of 4 mL/min (8 mL/min total).

Polarization curve experiments were conducted galvanostatically (constant current) in a stepwise manner. The first current density step of 1 mA/cm^2 was held for four minutes to allow the cell to begin operating while all subsequent steps, as described in Table 3.2, were held for two minutes. The initial current density of 1 mA/cm^2 was used to judge whether the cell would operate properly, or if there was

Table 3.2 – Description of galvanostatic current densities used for performing a polarization curve experiment. Each step held for two minutes.

j Domain (mA/cm^2)	Δj Step (mA/cm^2)
5–50	5
50–200	25
200–600	50

an issue with the cell/experimental setup. Properly operating cells would commonly begin at low voltages of $\approx 800\text{--}900$ mV and increase to $\approx 1.3\text{--}1.4$ V. In the event that the voltage did not increase to > 1.3 V, it indicated there was an issue with the cell and/or the test-station. Experiments were generally conducted up to a maximum current density of 600 mA/cm² or until the cell reached a potential of 2.2 V, whichever occurred first. Cell performance testing began with a polarization curve, followed by EIS, and then the same procedure was repeated two additional times (3x pol. curves & 3x EIS total). The cell and GDU temperatures, as well as liquid flow through the system, were maintained during the entirety of the testing process. Data acquisition occurred at a frequency of once per second while plotted data points for a given current density step are averaged over the last five seconds of obtained data (a brief discussion on this topic is provided in Section 3.2.2).

Cell stability was generally interpreted from the relative change in performance observed between consecutive polarization curves (the performance almost always worsened). However, a limited number of potentiostatic (constant voltage) experiments were conducted to further assess cell stability. The stability tests were performed approximately 12 hours after the polarization curve experiments and during that time the cell was sealed from its environment using fittings installed into the cell end plates. Prior to being isolated from the test-station, the cell was flushed with deionized and degassed water. Since the cell was disconnected from the test-station it cooled to room temperature prior to stability testing. Furthermore, the KOH solutions (0.85 mol/L) within the GDUs were replaced with newly prepared solutions. For the potentiostatic cell stability tests the cells were operated at 1.8 V for periods of either 30 minutes or one hour with EIS performed before and after with a total cumulative test time of two hours; i.e., the cells were tested with EIS, operated at 1.8 V for the allotted test time (30 minutes or one hour), retested with EIS, and then the same process was repeated until the total potentiostatic operational time was two hours.

3.1.6 Electrochemical Impedance Spectrometry

In an effort to differentiate between the activation, ohmic, and mass transport losses within the tested cells, electrochemical impedance spectrometry (EIS) was utilized. Galvano EIS was used such that a small sinusoidal current perturbation ($j(t) = j_0 \cos(\omega t)$) is applied to the cell resulting in a phase-shifted sinusoidal voltage response ($V(t) = V_0 \cos(\omega t + \phi)$) [7]. Converting to complex notation the impedance may be

written in terms of a real and imaginary component,

$$Z = \frac{V_0 e^{i\omega t + i\phi}}{j_0 e^{i\omega t}} = \frac{V_0}{j_0} e^{i\phi} = Z_0 (\cos \phi + i \sin \phi)$$

$$Z_{re} = Z_0 \cos \phi$$

$$Z_{im} = Z_0 i \sin \phi$$

where Z_0 is the impedance magnitude and ϕ is the phase shift [7]. Plotting Z_{re} and $-Z_{im}$ obtained from many orders of magnitude in frequency (for the perturbation) results in a Nyquist impedance plot. EIS experiments were performed with a potentiostat (SP-300, Biologic) using the parameters outlined in Table 3.3.

Table 3.3 – Primary parameters used for EIS experiments.

Current Density (mA/cm ²)	20	300	600
Amplitude (mA/cm ²) ^a	4 (20%)	30 (10%)	60 (10%)
High Frequency (kHz)	200	200	200
Low Frequency (mHz)	50	500	500
Points/Decade	15	15	15

^a Value in parentheses is the amplitude as a percentage of the tested current density

Nyquist plots obtained from EIS are commonly interpreted using equivalent circuits. A relatively simplistic model of an electrochemical cell may be created using only resistors and capacitors. The equivalent circuit representation of an ohmic process is simply a resistor and since a resistor is frequency (time) independent, and therefore does not contain an imaginary component, manifests itself as a point along the real axis of a Nyquist plot [7]. The equivalent circuit for an electrochemical reaction is more complex, but is commonly approximated as a capacitor and resistor in parallel. If reaction kinetics are approximated by the Tafel equation then the corresponding impedance may be approximated as a resistor (referred to as Faradaic resistance) [7]. The build up of electronic charge in the electrode and ionic charge in the electrolyte at the interface between the electrode and the electrolyte may be approximated as a capacitor (referred to as double-layer capacitance) [7]. The parallel combination of a resistor and capacitor manifests itself as a semicircle in a Nyquist plot with the diameter of the semicircle proportional to the Faradaic resistance. Derived from this information, the equivalent circuit used for the work herein is provided in Figure 3.9. Note that R_Ω accounts for both electronic and ionic ohmic losses. The equivalent circuit was used to determine the cells' total ohmic resistance as the real-axis intercept in the high frequency domain—this is referred to as the high frequency

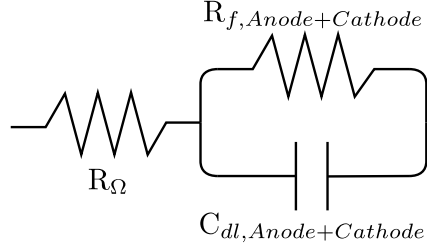


Figure 3.9 – Equivalent circuit used for interpreting Nyquist plots obtained from EIS [7].

resistance (HFR). Similarly, the charge transfer resistance (CTR) of the cells was determined by subtracting the HFR value from the real-axis intercept in the low frequency domain—this yields the aforementioned semicircle diameter for the Faradaic resistance.

3.2 Results and Discussion for Electrode Fabrication and Cell Testing

Contained herein are the results obtained for inkjet printed electrodes for AEM-based water electrolyzers. A focus on the printing process and the CCM electrodes produced therefrom is provided in Section 3.2.1. Section 3.2.2 then covers subtopics related to the validation of the test-station and cell hardware such as gasket materials, gasket thicknesses, membrane materials, and bipolar plate flow patterns. A brief discussion on cell repeatability is provided in Section 3.2.3 followed by proof-of-concept CCM- and CCS-based results in Section 3.2.4. The obtained cell performances are compared to literature in Section 3.2.4 and lastly, stability testing results are briefly discussed in Section 3.2.6.

3.2.1 Electrode Fabrication

A total of 16 CCMs were fabricated for this work following the methodologies discussed in Section 3.1. Images of a sample CCM are provided in Figure 3.10 where the cathode is shown in Figure 3.10a and the anode is shown in Figure 3.10b. To compare the obtained cathode microscopy images to that of a Nafion-based electrode, Pt|C Ink 0.3 (with Nafion ionomer in place of Aemion AP1-HNN8 ionomer) was used to produce a cathode electrode. The Nafion-based ink (which used Liquion solution LQ-1105 1100 EW³, 5 wt.%, Ion Power) was produced in the same manner as Aemion

³The equivalent weight (EW) refers to the grams of polymer per equivalent of sulfonate groups (IEC = 1000/EW) [109].

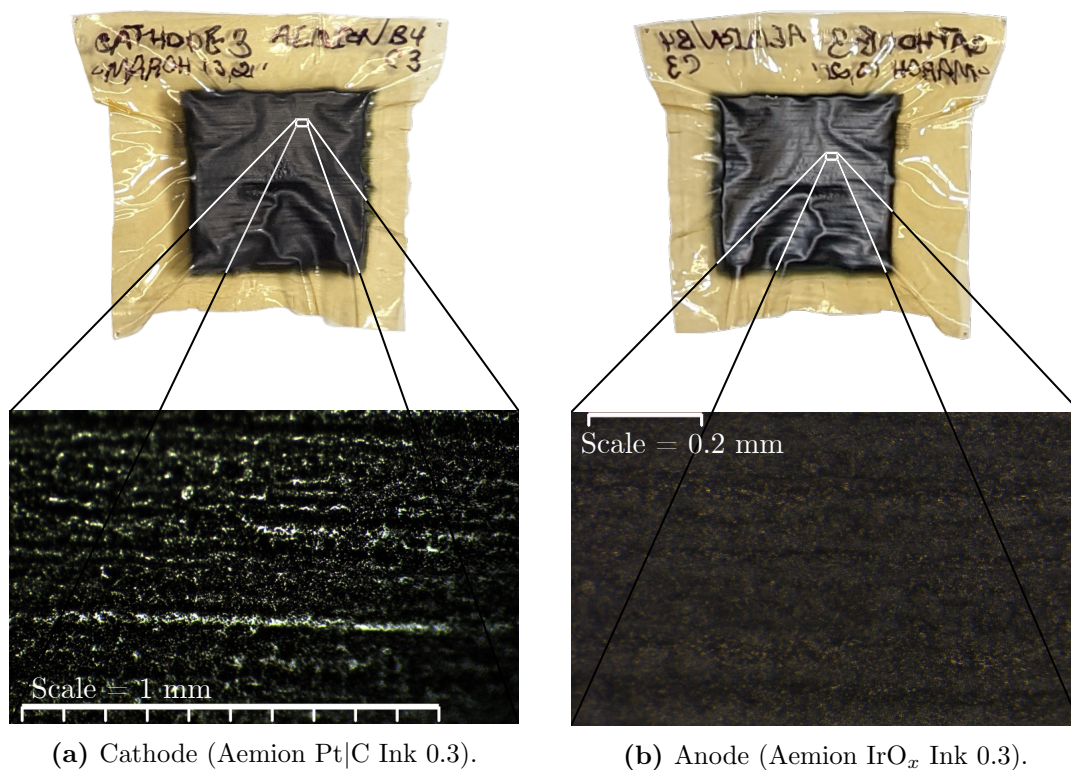
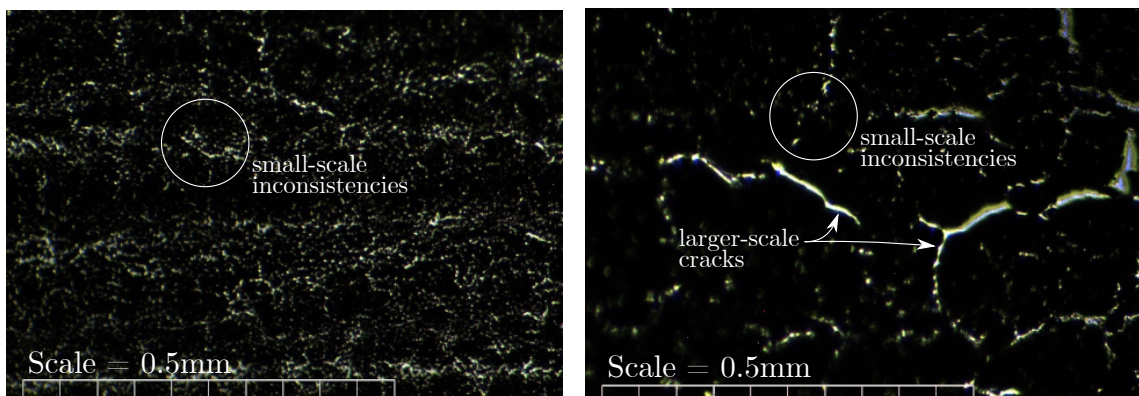


Figure 3.10 – Images of a sample CCM produced using inkjet printing. Membrane = Aemion AF1-HNN8-50.

Pt|C Ink 0.3 with 15 wt.% ionomer content in the solid-phase. Optical transmission microscopy images of both the Aemion- and Nafion-based inks printed onto Aemion AF1-HNN8-50 membrane are provided in Figure 3.11. The Aemion-based electrode (Figure 3.11a) demonstrates numerous so-called small-scale “inconsistencies” while the Nafion-based electrode (Figure 3.11b) contains fewer small-scale inconsistencies, but contains relatively large-scale so-called “cracks”. The cracks contained in the Nafion-based electrode have previously been demonstrated in literature [33, 110], but the smaller-scale inconsistencies have not been. It is hypothesized that the small-scale inconsistencies shown in Figure 3.11 were caused by the swelling and subsequent shrinking of the Aemion AF1-HNN8-50 membrane during the electrode fabrication process. The different frequencies with which the small-scale inconsistencies occurred in Figs. 3.11a and 3.11b may be a result of the different ionomer materials used (Aemion vs. Nafion).

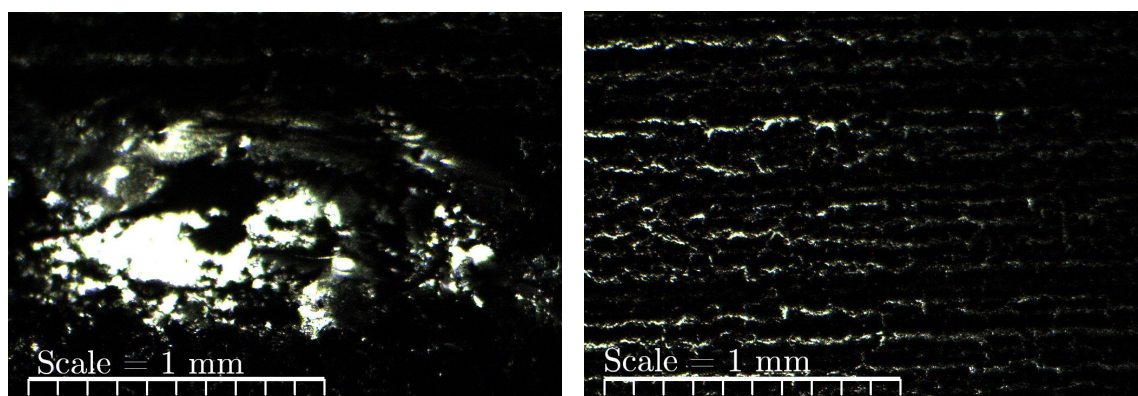
During CCM fabrication a number of issues were encountered that resulted in the failure of CCMs prior to being tested. One of the primary issues that was encountered was the swelling of the membrane during the printing process. While the membrane was observed to swell during both cathode and anode CL fabrication, it was more pro-



(a) Aemion cathode (Aemion Pt|C Ink 0.3). (b) Nafion cathode (Pt|C Ink 0.3 with Nafion).

Figure 3.11 – Comparison of cathodes fabricated using Aemion AF1-HNN8 and Nafion ionomers. The Nafion-based electrode was produced using Pt|C Ink 0.3 with Nafion ionomer in place of Aemion AF1-HNN8 (15 wt.% ionomer within the solid-phase of the ink). Both electrodes were printed onto Aemion AF1-HNN8-50 membrane.

nounced during anode CL fabrication since the anodes had higher catalyst loadings, and subsequently required more ink (and therefore ink solvent), to be printed onto the membrane. The height of the DPM-2800 printer head often had to be adjusted to 5.5 mm above the platen to avoid contacting the membrane as it swelled during the printing process. In one instance the printer head contacted the printed CL on the swelled membrane which resulted in a notable defect in the electrode (Figure 3.12a) compared to a regular CCM CL from the same batch (Figure 3.12b). Since the membrane is 50 microns thick and contacted the printer head at a height of 5.5 mm, the



(a) Electrode contacted by printer head. (b) Regular printed electrode.

Figure 3.12 – Microscopy images demonstrating the difference between a cathode contacted by the printer head and a regular electrode from the same CCM batch.

membrane swelled in excess of 5 mm out-of-plane⁴. Membrane swelling was subsequently managed by delaying the printing process between layers (commonly three minutes) to allow the ink solvent to evaporate from the membrane and thereby reduce swelling. In certain extenuating circumstances (such as using a 2.5 wt.% solid content IrO_x ink) additional heat was imparted to the CCMs between printed layers using two 75 W incandescent lightbulbs placed approximately 20 cm from the CCMs.

Another issue that resulted in the failure of CCMs was the apparent interaction between the catalyst inks and the Aemion AF1-HNN8-50 membrane. As seen in Figure 3.13, the catalyst ink appeared to react with the membrane and result in a notable defect in the CL (Figure 3.13a) compared to a regular CCM CL from the same batch (Figure 3.13b). During the fabrication of anode CLs for another separate batch of CCMs a pinhole was noticed in one of the CCMs, and upon further inspection as shown in Figure 3.14, pinholes were found in each of the three CCMs. The holes were hypothesized to be caused by the high methanol content in the IrO_x ink (Aemion IrO_x

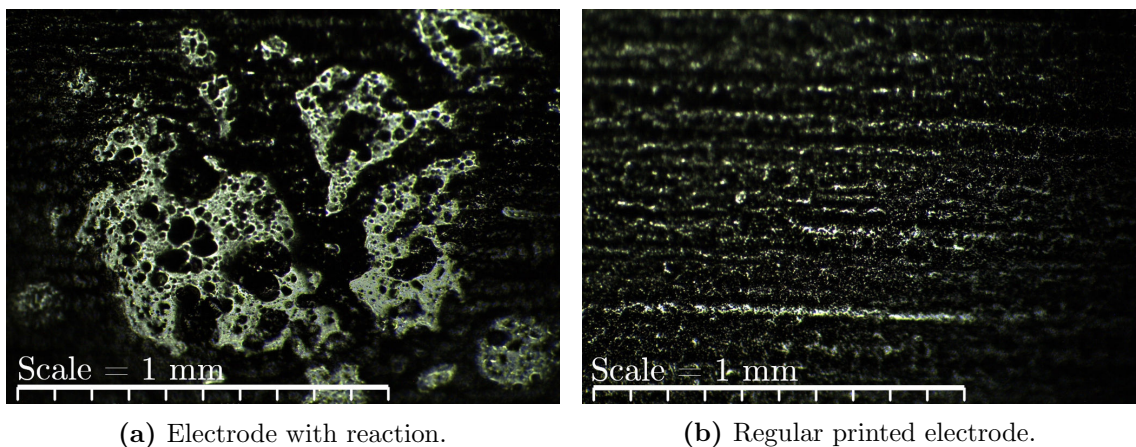


Figure 3.13 – Microscopy images demonstrating the difference between a partially reacted CCM and a regular electrode from the same CCM batch.

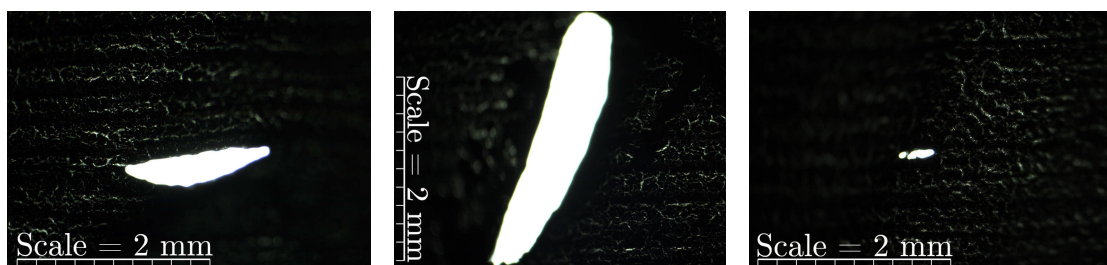


Figure 3.14 – Microscopy images of holes formed during anode fabrication for three separate CCMs from a single batch.

⁴The DPM-2800 printer head can technically be raised to 26.5 mm above the platen, but is typically set between 5.0–5.5 mm in the ESDLab.

Ink 0.2). IrO_x Ink 0.2 was produced using a 2 wt.% solution of Aemion AP1-HNN8 ionomer in methanol, whereas 5 wt.% had previously been used, and as a result, the ink contained a higher methanol content. Due to this observation, Aemion IrO_x Ink 0.3 was produced using a 4 wt.% solution of Aemion ionomer to decrease the methanol content in the final ink, and subsequently no CCMs formed holes during the electrode fabrication process.

The white horizontal lines that appear throughout Figs. 3.10a, 3.12b, 3.13b and 3.14 are hypothesized to be due to either non-operational nozzles within the printer cartridge head and/or cohesive forces within the catalyst ink. More specifically, the cathodes that demonstrate the white lines were imaged using a transmitting optical microscope that shines light through the sample, and therefore the white lines correspond to areas void of the printed electrode. Recalling from Section 3.1.3 that the printer head prints along the x -axis, which is parallel to the horizontal lines, any nozzles that do not print due to blockages may result in unprinted lines in the imaged electrodes. Similarly, the printer head shifts along the y -axis between printed passes, which is perpendicular to the horizontal lines, and if the ink printed during a previous pass cohesively binds together and begins to dry, then subsequently printed passes may not bind together and result in the observed lines.

Both the swelling and catalyst ink/membrane interaction issues encountered during CCM fabrication were observed to be more substantial during anode CL fabrication since the anodes take longer to produce than the cathodes. There was a high degree of variability, but the cathodes typically required ≈ 15 layers to achieve a desired loading of 0.1 mg_{Pt}/cm² while the anodes required roughly twice as many layers (≈ 30) to achieve a desired loading of 1 mg_{IrO_x}/cm². As a result, it is suggested that the anodes are fabricated first for future CCMs such that time and resources are not dedicated to producing cathode CLs for CCMs that ultimately fail due to issues during anode CL fabrication.

Generally, it was found that producing AEM-based CCMs using inkjet printing had a relatively high failure rate of $\approx 30\%$ (5 failures out of 16 CCMs produced for this work), irrespective of cell assembly or resulting cell performance. Since one of the primary issues encountered during CCM fabrication was membrane swelling, CCMs were fabricated using a newly developed membrane by Ionomr Innovations Inc. termed Aemion AF2-HNN8 which has been demonstrated to have a 60% lower area change compared to Aemion AF1-HNN8 when saturated with water [111]. The batch of Aemion AF2-HNN8-50 CCMs was fabricated using Aemion Pt|C Ink 0.3 (using 40 wt.% Pt|C by HyPlat) for the cathode and Aemion IrO_x Ink 0.3 for the

anode. The catalyst inks used contained the AP1-HNN8 ionomer⁵. Note that the Aemion AF2-HNN8-50 membrane was received in a mixed chloride-iodide form and was not converted to a fully chloride form prior to CCM fabrication based upon the work of Koch et al. [59].

Images of a sample CCM fabricated with Aemion AF2-HNN8-50 are provided in Figure 3.15 where, based upon the recommendation provided above, the anode was produced first and imaged with the transmitting optical microscope (Figure 3.15a) and the cathode was printed second and imaged with the stereoscopic microscope (Figure 3.15b). The CCMs produced with the AF2-HNN8 membrane were generally easier to produce compared to CCMs with the AF1-HNN8 membrane as the newly developed membrane swelled very little during the printing process. In fact, the new membrane swelled so little that the printing process was expedited by changing

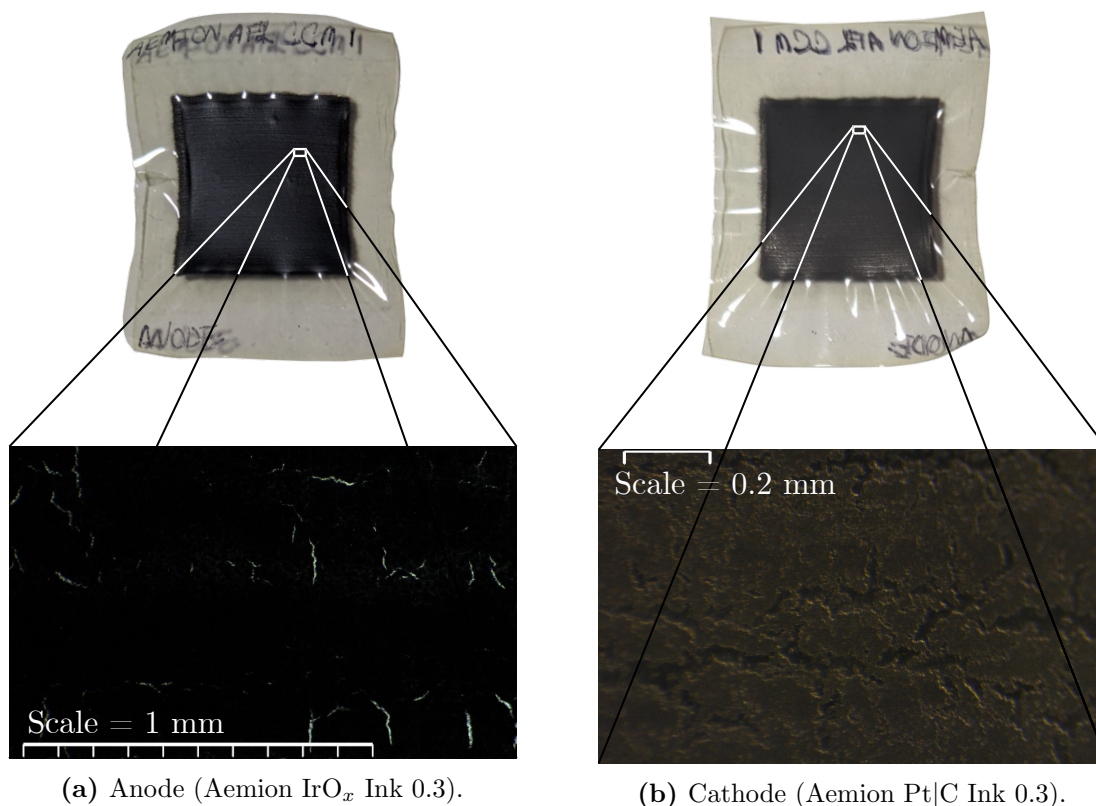


Figure 3.15 – Images of a sample CCM produced using inkjet printing. Membrane = Aemion AF2-HNN8-50.

⁵Ionomr Innovations Inc. produces a corresponding Aemion AP2-HNN8 ionomer that may be used for catalyst inks in the future, but doing so was deemed beyond the scope of the current work since the inks were developed using the AP1 ionomer.

the printing settings⁶ (i.e., more solvent could be continually printed onto the membrane since swelling was not an issue). Changing the printing settings appeared to in turn remove the white lines seen in the electrodes produced onto Aemion AF1-HNN8 (Figure 3.15a vs. Figure 3.10a). The decreased frequency of the previously mentioned small-scale inconsistencies in Figure 3.15a may be due to a combination of the decreased swelling of the Aemion AF2-HNN8 membrane and the changed printing settings. The CCMs produced using the Aemion AF2-HNN8-50 membrane were not tested in-situ as this work focused on the use of Aemion AF1-HNN8-50.

3.2.2 Validation of Test-Station Equipment & Cell Hardware

Since AEM-based water electrolyzers had not previously been operated using the cell hardware and test-station equipment discussed in Section 3.1, a number of experiments were conducted to ensure that the hardware and equipment functioned as required. As an initial validation of the test-station equipment, a PEM-based water electrolyzer was assembled and tested using the methodologies and equipment described in Ref. [33], and then the same cell was tested with the equipment discussed in Sections 3.1.1 and 3.1.2. The intent of this experiment was to verify that the developed AEM-based test-station could be used to reproduce expected polarization curve results. Note that the equipment utilized in Ref. [33] by Mandal et al. is referred to herein as the “PEM-based test-station”. Information for the PEM-based CCM operated with both test-stations is provided in Table 3.4 with additional information regarding CCM fabrication and cell assembly provided in Ref. [33].

Using the PEM-based test-station the cell was first conditioned⁷ at a temperature of 80°C with deionized water fed to the anode (also at 80°C) at a flow rate of

Table 3.4 – Summary of PEM-based CCM properties tested to validate the functionality of the AEM-based water electrolyzer test-station.

Property	Value
Membrane Material	Nafion 211
Cathode Catalyst & Loading	TKK 46.7 wt.% Pt C, 0.11 mg/cm ²
Cathode Ionomer Content	30 wt.% Nafion (1100 EW)
Anode Catalyst & Loading	Umicore Ir, 0.97 mg/cm ²
Anode Ionomer Content	5 wt.% Nafion (1100 EW)

⁶The printing spacing of the cartridge head was adjusted such that there was approximately a 48% overlap of printed passes along the y -axis.

⁷Mandal et al. conditions their PEM-based cells by applying current densities of 0.02, 0.1, 0.2, and 1 A/cm² for 15 minutes and 5 minutes at 2 A/cm² [33].

12.6 mL/min. The polarization curve test was then conducted directly following cell conditioning using the PEM-based test-station with results provided in Figure 3.16. The cell was then disconnected from the PEM test-station, connected to the AEM-based test-station, and the system was heated to 80°C (the cell cooled to $\approx 75^\circ\text{C}$ during the transition). To validate the functionality of the Norprene pump tubing with the Gilson Minipuls pump, polarization curve experiments were conducted using the Gilson PVC peristaltic pump tubing (the tubing used by Mandal et al.) and then the Norprene-based tubing. Since the internal diameters of the tubings were different, the pump speed was adjusted such that the flow rate for both tests was maintained at 8.4 mL/min⁸. This flow rate was lower than that used with the PEM-based test-station, but is similar to the flow rate used by Mandal et al. in their published work (9 ml/min [33]), and is in far excess of the required stoichiometric flow rate at 2 A/cm² (0.06 mL/min as per Faraday’s first law [112]).

As seen from the results provided in Figure 3.16, the three polarization curves obtained for the PEM-based cell are very similar for $j < 800 \text{ mA/cm}^2$, but begin to diverge thereafter. The 20 mV increase at 2 A/cm² between the curve produced

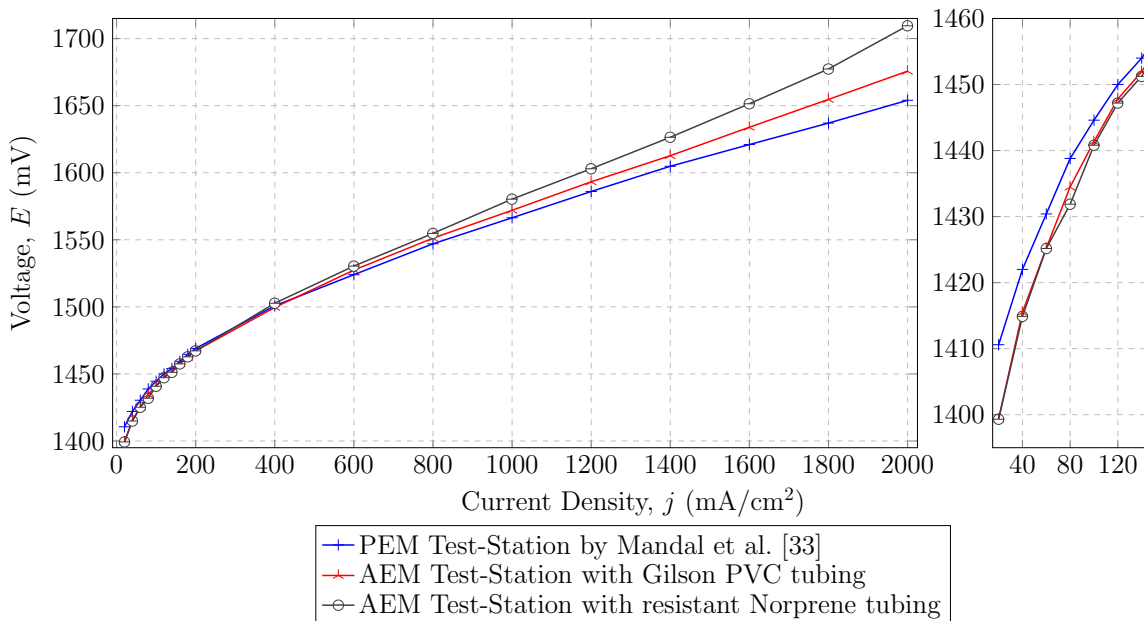


Figure 3.16 – Polarization curves obtained for a PEM-based water electrolysis cell using an existing test-station setup used in Ref. [33] and the test-station developed for this work. Cell was operated at 80°C with deionized water fed to the anode at 8.4 ml/min (AEM Test-Station) or 12.6 mL/min (PEM Test-Station).

⁸This is the maximum flow rate with the Norprene tubing as determined in Appendix B.5.

using the AEM-based test-station with PVC tubing and the PEM-based test-station is not unexpected⁹. Conversely, the decreased performance for the curve obtained using the Norprene-based tubing for $j > 1400 \text{ mA/cm}^2$ is hypothesized to be due to issues regarding the supply of water since none of the PEM-based water electrolyzer results by Mandal et al. demonstrate mass transport losses [33]. The PVC peristaltic pump tubing by Gilson is calibrated with retaining stops on both ends to ensure that the tubing is properly tensioned when fitted into the pump head. Since the Norprene-based tubing was not procured from Gilson, and therefore does not contain the calibrated retaining stops, the tubing may not be properly tensioned within the pump head and consequently not function properly. However, because the maximum operational current density for the AEM-based water electrolyzers tested for this work was only 600 mA/cm^2 , it was deemed that the Norprene tubing would be sufficient for use, but that properly calibrated tubing by Gilson should be used in the future¹⁰, especially if operating at elevated current densities. Apart from the limited issues encountered with the peristaltic pump tubing, the developed test-station functioned as expected and was used to successfully produce results consistent with other test equipment.

Steady-State Operation of AEM-Based Cells for Polarization Curves

To demonstrate that the cell performance (voltage) is steady state at the end of each of the galvanostatic steps used to produce a polarization curve, the complete data for a sample AEM-based water electrolyzer is provided in Figure 3.17. Although some of the steps at higher current densities ($j > 75 \text{ mA/cm}^2$) in Figure 3.17 increase in voltage, it is hypothesized that the increase is not due to transient effects, but is instead due to the instability of the cell's electrodes (refer to Section 3.2.6 for more information on cell stability). As such, the reported voltage values in the polarization curves are given as the average over the last five seconds at a given current density step.

Cell Gasket Material and Thickness

Materials commonly used for cell gaskets in the ESDLab at the University of Alberta include PTFE, PTFE-coated fiberglass, and Kapton polyimide. Due to the avail-

⁹One potential source for the slight decrease in ohmic performance could be due to ions introduced to the system from the ohmic heater within the GDU. The effect of using immersion heaters of this nature is currently under investigation at the ESDLab.

¹⁰Gilson offers a tubing made of polypropylene (PP) and according to the DECHEMA Corrosion Handbook on KOH, variants of PP are permanently resistant to $\leq 50 \text{ wt.}\%$ aqueous KOH up to 100°C [101].

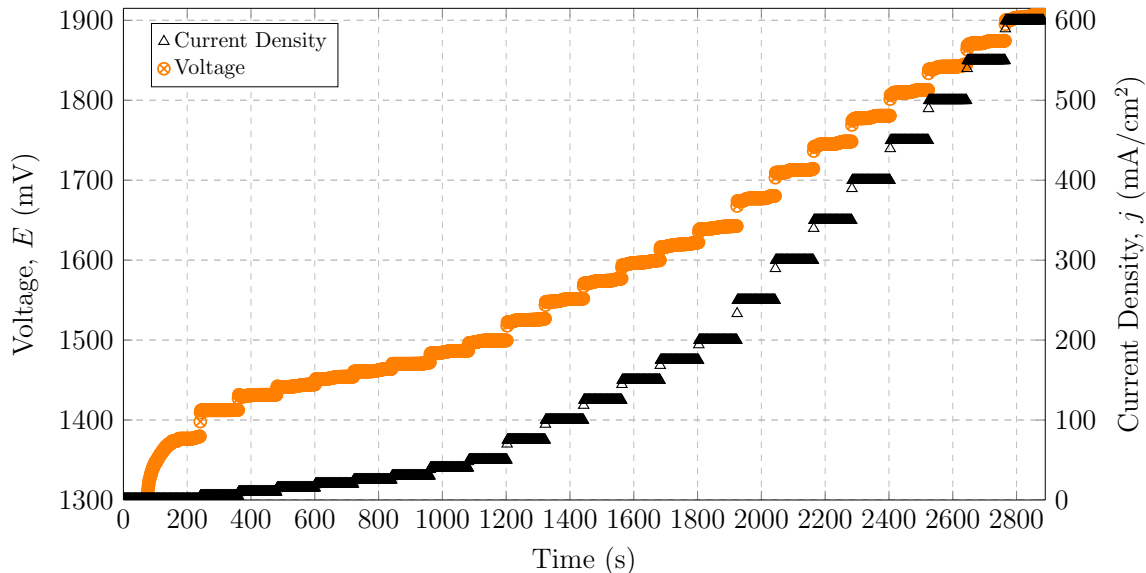


Figure 3.17 – Demonstration of steady state operation at each galvanostatic step used to produce a polarization curve for a sample AEM-based water electrolyzer. Further details for the tested cell provided in Table 3.5 as ‘FAA-3 CCM’.

ability of thicknesses and practical considerations¹¹, cells were initially tested with gaskets composed of 2 mil Kapton polyimide and 5 mil PTFE (the two materials were combined to achieve the desired thickness of 7 mil/electrode). Using three cells, one with a Fumapem FAA-3-based CCM and two with Aemion AF1-HNN8-based CCMs, the mixed Kapton polyimide/PTFE gasket combination was compared to PTFE-only gaskets. For the PTFE-only gaskets, 2 mil and 5 mil thicknesses were again combined to achieve the desired 7 mil thickness/electrode. A summary of the electrode characteristics for the tested cells is provided in Table 3.5.

As seen in Figure 3.18, the FAA-3-based cell assembled with PTFE and Kapton polyimide gaskets was found to have good performance. However, upon reusing the same gaskets for the Aemion-based cell, the performance was found to drastically reduce. Using PTFE gaskets for a cell assembled with an Aemion-based CCM from the same batch as the previously tested Aemion-based cell, the performance improved to, and closely matched, the performance of the FAA-3-based cell. Thickness measurements (No. 227-211 micrometer, Mitutoyo) taken near the edge of the square cutout in the middle of the mixed Kapton polyimide/PTFE gasket combination after cell disassembly indicated that the thickness had reduced by ≈ 2 mil (the thickness of the Kapton polyimide used) for both electrodes. The reduction in gasket material may

¹¹The Kapton polyimide material has an adhesive backing such that it could easily be combined with gaskets of other thicknesses.

Table 3.5 – Summary of CCMs tested for comparing PTFE and Kapton polyimide gasket materials.

Characteristic	Batch of 1 FAA-3 CCM	Batch of 2 Aemion CCMs
Membrane	Fumapem FAA-3-50	Aemion AF1-HNN8-50
Anode Catalyst Loading	1.0 mg _{IrO_x} /cm ²	0.97 mg _{IrO_x} /cm ²
Anode Catalyst Ink	Aemion IrO _x Ink 0.2	Aemion IrO _x Ink 0.2
Anode Ionomer Loading	15 wt.% of CL	15 wt.% of CL
Cathode Catalyst Loading	0.20 mg _{Pt} /cm ²	0.23 mg _{Pt} /cm ²
Cathode Catalyst Ink	Aemion Pt C Ink 0.2	Aemion Pt C Ink 0.25 ^a
Cathode Ionomer Loading	15 wt.% of CL	25 wt.% of CL

^a An uncharacterized ink with the same solvent solution as Aemion Pt|C Ink 0.2, but with 60 wt.% Pt|C (HyPlat). Additionally contained 25 wt.% ionomer as opposed to 15 wt.% used for all other inks

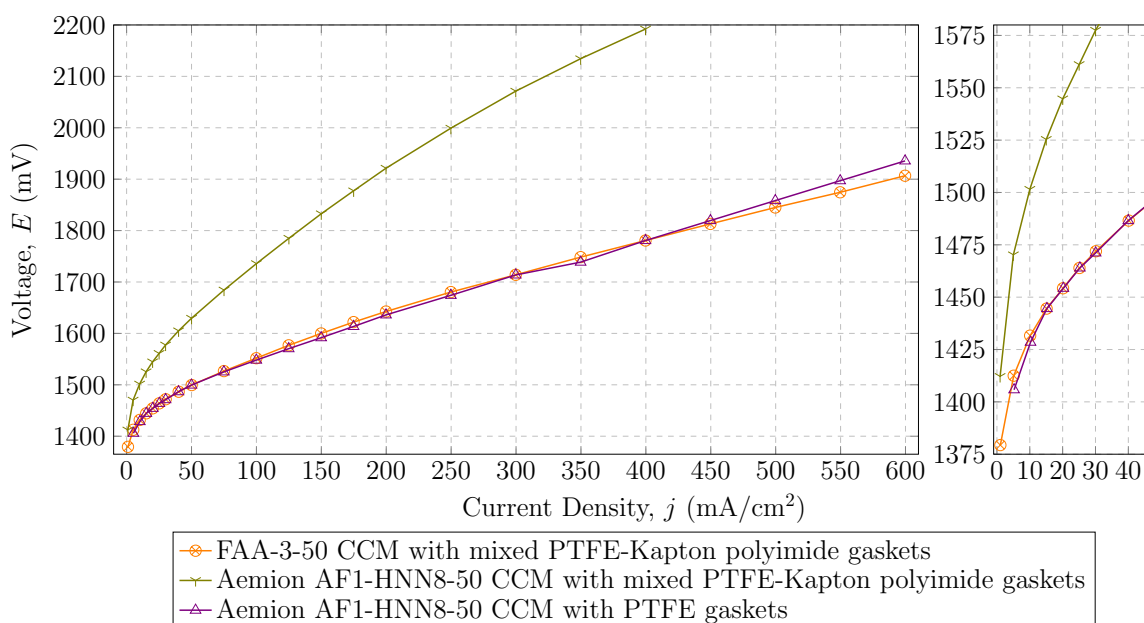


Figure 3.18 – Polarization curves comparing cells assembled with Kapton polyimide and PTFE gaskets (7 mil thickness per electrode). Cells operated at 60°C with 0.85 mol/L KOH fed to both electrodes.

have resulted in the over compression of the MEA or poor cell sealing. The same measurements conducted for the PTFE-only gaskets after cell disassembly indicated no change in the thickness. As such, it was concluded that Kapton polyimide should not be used for testing as it was found to not be stable under the operating conditions of the cell, which may impact the cell in an unknown manner (i.e., possible contamination of the cell). Note that polyimides, such as Kapton, have been documented to have a lack of resistance to 2 mol/L KOH at room temperature [101], and therefore

it is hypothesized that the observed instability of the Kapton polyimide is due to the KOH solution within the cell.

Limited electrolyzer testing was conducted with PTFE coated fiberglass gaskets to analyze how non-compressible 6 mil gaskets would compare to the compressible 7 mil PTFE gaskets discussed above. Note that the PTFE coated fiberglass gasket material was only available in 3, 5, 6, and 10 mil variants such that a direct comparison of 7 mil thick gaskets was not possible. The characteristics of the Aemion AF1-HNN8-50 CCMs tested with the two different gasket thicknesses are provided in Table 3.6 while the resulting cell performance and Nyquist plots are provided in Figure 3.19. As seen in Figure 3.19, the performance of the cell with the thinner gaskets was much poorer, notably in the kinetic region. From the Nyquist plot it is clear that the CTR for the cell with 6 mil gaskets was much greater than the CTR for the cell with 7 mil gaskets (3411 vs. 2319 $\text{m}\Omega\cdot\text{cm}^2$, respectively), which matches the poorer kinetic performance observed in the polarization curves.

The change in porosity of the PTLs due to the compression of the MEA may be estimated using the following relationship [113],

$$\varepsilon_2 = 1 - \frac{t_1}{t_2} (1 - \varepsilon_1) \quad (3.3)$$

where ε and t are the porosity and PTL thickness, respectively, and state 1 is before compression and state 2 is after. Assuming that the pinch of the cell is evenly split between the two electrodes, and the compression is exhibited entirely in the PTLs, then each of the PTLs is compressed 50 and 25 μm when using the 6 and 7 mil gaskets, respectively (recall the pinch is calculated as per Eq. (3.2)). As such, the estimated change in porosities for the Toray 90 and Bekipor Ni PTLs when using the 6 and 7 mil gaskets, as per Eq. (3.3), are provided in Table 3.7. The estimated decrease in PTL porosity when using the thinner 6 mil gaskets is approximately double that of when using the thicker 7 mil gaskets. Although the absolute porosity of the PTLs when

Table 3.6 – Summary of CCMs tested for comparing 6 mil and 7 mil gasket thicknesses.

Characteristic	Batch of 2 Aemion CCMs
Membrane	Aemion AF1-HNN8-50
Anode Catalyst Loading	1.0 $\text{mg}_{\text{IrO}_x}/\text{cm}^2$
Anode Catalyst Ink	Aemion IrO_x Ink 0.3
Anode Ionomer Loading	15 wt.% of CL
Cathode Catalyst Loading	0.11 $\text{mg}_{\text{Pt}}/\text{cm}^2$
Cathode Catalyst Ink	Aemion Pt C Ink 0.3
Cathode Ionomer Loading	15 wt.% of CL

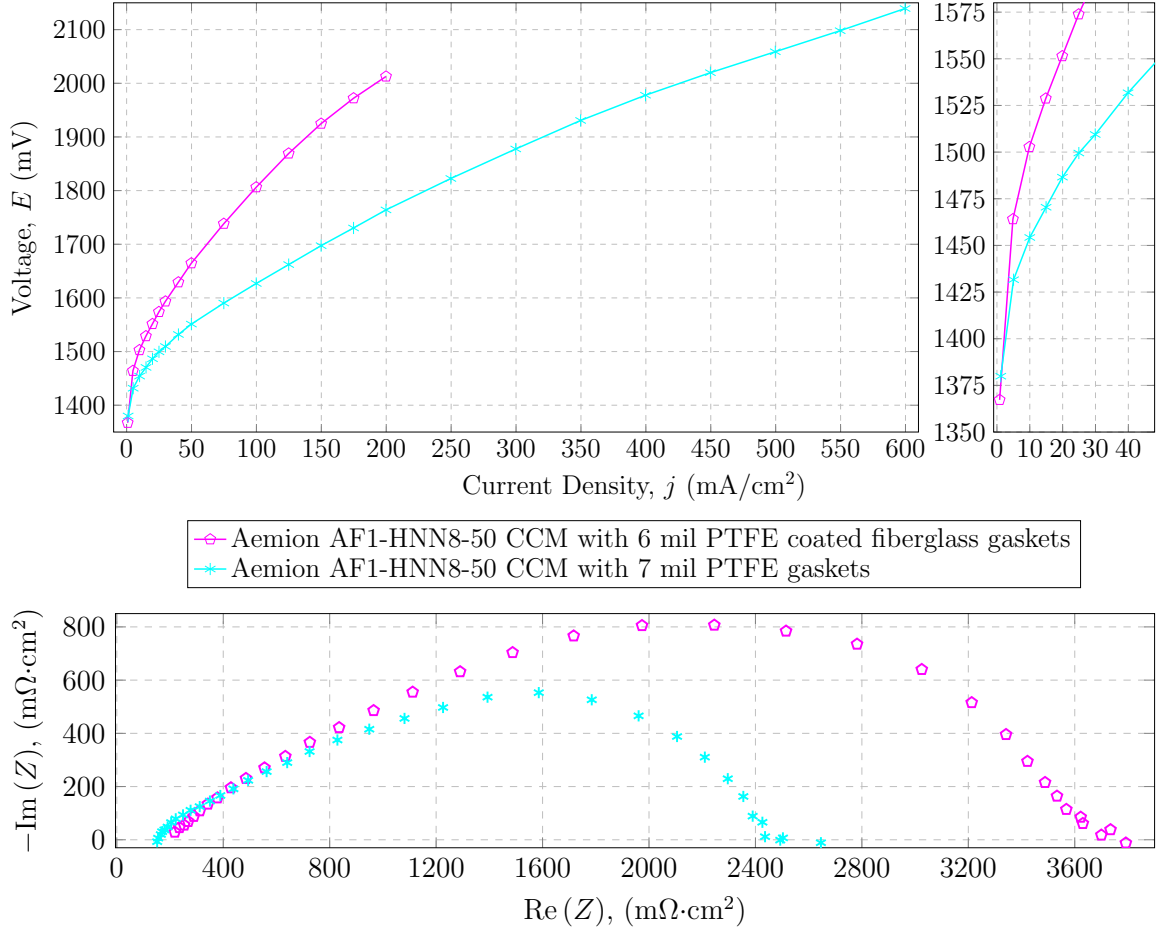


Figure 3.19 – Polarization curves and Nyquist plots for Aemion-based cells assembled with 6 and 7 mil thick gaskets (per electrode). EIS data for Nyquist plots obtained at 20 mA/cm².

Table 3.7 – Summary of PTL thicknesses and estimated porosities with 6 and 7 mil thick gaskets.

State	Toray 90 [62]		Bekipor Ni [114]	
	Thickness (μm)	Porosity (%)	Thickness (μm)	Porosity (%)
Initial (uncompressed)	280	75.0	275	60.0
With 6 mil Gasket	255	69.6 ^a	250	51.1 ^a
With 7 mil Gasket	230	72.5 ^a	225	56.0 ^a

^a Estimated using Eq. (3.3)

using the 6 mil gaskets was estimated to still be > 70% and 51% for the Toray 90 and Bekipor Ni PTLs, respectively, it is hypothesized that the notable change in the relative porosity for the Toray 90 PTL may be significant due to changes in the pore size distribution. That is, Toray 90 contains PTFE (5 wt.% in this case) such that

it is hydrophobic, which is often a desirable attribute for fuel cell gas diffusion layers (GDLs) to help expel produced water. However, in the case of alkaline electrolysis water is a reactant in the cathode, and a change in the pore size distribution will change the water transport properties of the layer which may further result in a lack of reactant in the CL¹². Although Toray 90 was still used for all of the cells tested herein, it is recommended that an alternative cathode PTL material such as AvCarb MGL280 [117], which has the same thickness and porosity as Toray 90, but no PTFE content, is tested in the future.

Although the specific thickness of the gaskets used, 6 mil vs. 7 mil, is not generally applicable for AEM-based electrolyzers since it is dependent upon the MEA components, the results herein demonstrate how important it is to select the proper gasket thicknesses during cell assembly. While the absolute thickness of the gaskets used is not generally applicable, the pinch value is. That is, the MEA components, including the cell gaskets, may be selected such that the MEA is compressed 50 μm during cell assembly. Future tests may be required to analyze how a lower pinch ($< 50 \mu\text{m}$) affects cell performance.

Fumapem FAA-3 and Aemion AF1-HNN8-50 Membranes

Most tests were conducted with Aemion AF1-HNN8-50 membranes, but a single batch of CCMs was produced using Fumapem FAA-3-50 membrane (Fuel Cell Store). During the production of the FAA-3-based CCMs, one CCM failed (tore) while removing the tape used to hold it in place during the printing process. Another CCM from the batch failed during cell assembly as the membrane had wrinkled during the printing process, was left to fully dry, and cracked during cell assembly as the membrane in its dry state was flattened by the cell hardware. It was due to this result that all other CCMs were converted to hydroxide form prior to cell assembly and subsequently assembled into cells while fully hydrated with water (while hydrated the membrane becomes dimensionally flexible (non-brittle)). Of note is that a CCM fabricated with Aemion AF1-HNN8 was also assembled into a cell dry, but did not crack as the FAA-3 membrane did. Similarly, none of the CCMs fabricated with Aemion AF1-HNN8 tore while removing the tape used to hold them in place during the printing process. As such, it was anecdotally concluded that the Aemion AF1-

¹²Using the Young-Laplace equation for relating the invading capillary pressure to pore radii for the PTL [115] ($p_{non-wetting} - p_{wetting} = -2\gamma \cos(\theta)/r$), the required invading pressure will increase if the radii decreases (recall $\theta > 90^\circ$ for hydrophobic materials [116]). If it is assumed that the pressure within the PTL remains constant irrespective of PTL compression (i.e., the PTL remains under ambient conditions), then a reduction in pore size radii will result in fewer pores being infiltrated.

HNN8-50 membrane exhibits better physical properties than the Fumapem FAA-3-50 membrane. This anecdotal conclusion is supported by the physical data for the two materials as Aemion AF1-HNN8 has a lower Young’s modulus (higher flexibility) and higher ultimate tensile strength¹³ [37, 118].

The performance of the only operational FAA-3 CCM from the batch was provided in Figure 3.19 above. As stated, the performance of the FAA-3 cell was very similar to an Aemion AF1-HNN8-based cell with similar catalyst loadings and tested under the same conditions (CCM details provided in Table 3.6). Despite Aemion AF1-HNN8 having a reportedly higher hydroxide conductivity compared to FAA-3 (103 vs. 51 mS/cm at 40°C, respectively [38, 119]), and the same thickness (50 μm), the cells assembled with the two different CCMs had a very similar HFR as seen from the Nyquist plots provided in Figure 3.20 (171 and 167 $\text{m}\Omega\cdot\text{cm}^2$, respectively). The difference in the CTR for the two cells is not hypothesized to be due to the different membrane materials, but other differences in the CCMs such as ionomer content and catalyst loadings (refer to Table 3.5). Further testing is required to confirm that the two materials produce similar performing cells and to analyze how the two different materials behave when subject to longer testing. Note that FAA-3 has demonstrated reasonably high durability for up to 1000 hours of cell voltage cycling, but Aemion membranes have not been tested under the same time durations [73].

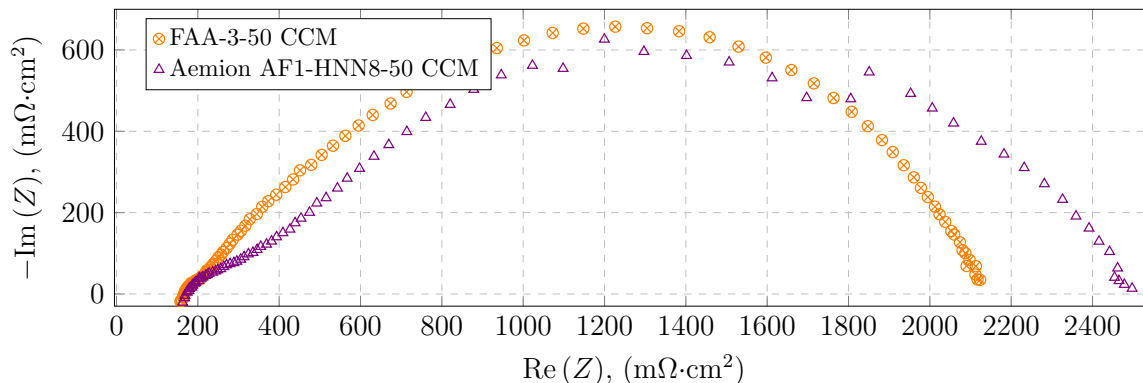


Figure 3.20 – Nyquist plots for CCMs produced using Fumapem FAA-3 and Aemion AF1-HNN8-50 membranes. EIS data obtained at 20 mA/cm^2 .

¹³The Young’s modulus for Aemion AF1-HNN8 (Cl^- form, dry) and FAA-3 (ionic form not stated, 50% relative humidity) are respectively 940 ± 40 MPa and 1400 ± 400 MPa while their ultimate tensile strengths are 50 ± 2 MPa and 32.5 ± 7.5 MPa [37, 118].

Bipolar Plate Flow Pattern

While the majority of cells were tested using the extended parallel channel bipolar plates discussed in Section 3.1.4, bipolar plates with a serpentine flow pattern were also used. Following the observation, as seen in Figure 3.21, that CCMs would notably swell out-of-plane when converted to hydroxide form and rinsed with deionized water, non-laminated CCMs were tested. The non-laminated CCMs were observed to swell in-plane as opposed to out-of-plane, which was hypothesized to have less of an effect on the CCMs CLs. A cell assembled with the extended parallel flow channel plates and a non-laminated CCM was found to be non-operational (could not generate a potential > 1.2 V), which was hypothesized to be due to issues regarding the sealing of the cell. The extended parallel flow channel pattern goes beyond the active area of the CCM and therefore the membrane, which also goes beyond the active area of the CCM, does not have rigid support where the flow channels are situated along the perimeter of the 5 cm^2 area. Of course the membrane would have rigid support if it extended beyond the length of the channels (beyond the horizontal manifolds in Figure 3.22a), but this was not an option for CCMs already fabricated on membrane pieces with a smaller size (1.75×1.75 ”). It was hypothesized that the non-rigid region of the flow channels resulted in the poor sealing of the cell as the membrane could not be firmly supported. In response to this issue, the serpentine flow field plates were used. Images comparing the extended parallel and serpentine flow field plates are provided in Figure 3.22. In contrast to the extended parallel channel flow field pattern, the serpentine flow channel pattern (Figure 3.22b) is primarily restricted to the active area of the CCM, such that the membrane is rigidly supported along the perimeter of the active area by the plates and therefore forms a better seal for the cell. Of note is that plates with a parallel channel (non-extended), could have been

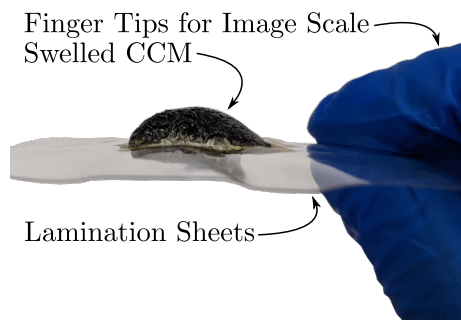


Figure 3.21 – Image demonstrating a CCM swelled out-of-plane following conversion to hydroxide form and rinsed with deionized water.

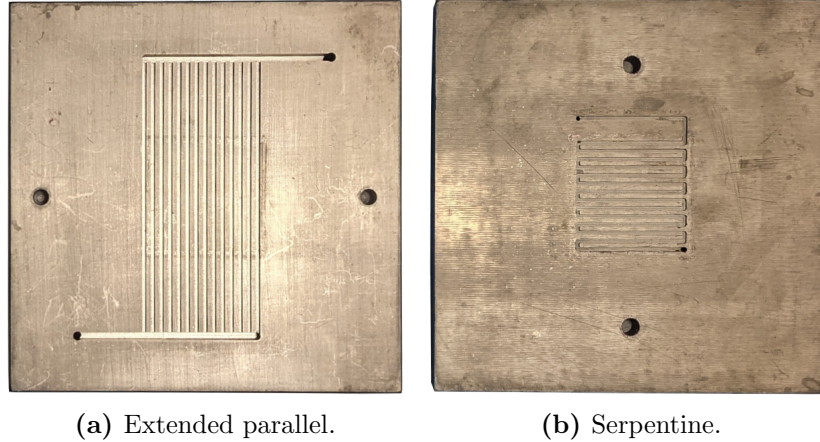


Figure 3.22 – Images of different flow patterns used for cell testing. The graphite plates shown were used for the cathode and respectively complimented by titanium plates with the same flow pattern for the anode.

used for this same purpose, but the serpentine channel plates were used due to their availability.

The cell performances obtained using the parallel extended and serpentine flow pattern bipolar plates are provided in Figure 3.23. The characteristics of the CCM tested with the extended parallel channel plates are provided in Table 3.6 above while the CCM tested with the serpentine channel plates was the exact same, but had catalyst loadings of $0.12 \text{ mg}_{\text{Pt}}/\text{cm}^2$ and $1.0 \text{ mg}_{\text{IrO}_x}/\text{cm}^2$ (the CCM tested with the extended parallel channel plates had loadings of $0.11 \text{ mg}_{\text{Pt}}/\text{cm}^2$ and $1.0 \text{ mg}_{\text{IrO}_x}/\text{cm}^2$). Note that the CCM tested with the extended parallel channel plates was laminated as per the information in Section 3.1.4 and tested with 7 mil PTFE gaskets. Conversely, the CCM tested with the serpentine channel plates was non-laminated and tested with 10 mil PTFE coated fiberglass gaskets. The 10 mil thick gaskets (per electrode) were used such that a pinch of $50 \mu\text{m}$ was maintained in accordance with the results discussed previously regarding gasket thicknesses. As seen from the polarization curves in Figure 3.23, the two cells had a very similar initial performance, especially in the kinetic region. However, subsequent testing for the cell using the serpentine channel plates demonstrated that the cell was unstable (refer to ‘curve three’ in Figure 3.23). It was suspected that the cell was initially stable as it was sealed, but that at elevated current densities, and subsequently higher gas production rates as per Faraday’s first law, the cell became unsealed, and therefore unstable. Snoop® liquid leak detector was used to visually confirm that the cell was sealed from the ambient environment, so it was hypothesized that the cell was unsealed internally, not externally.

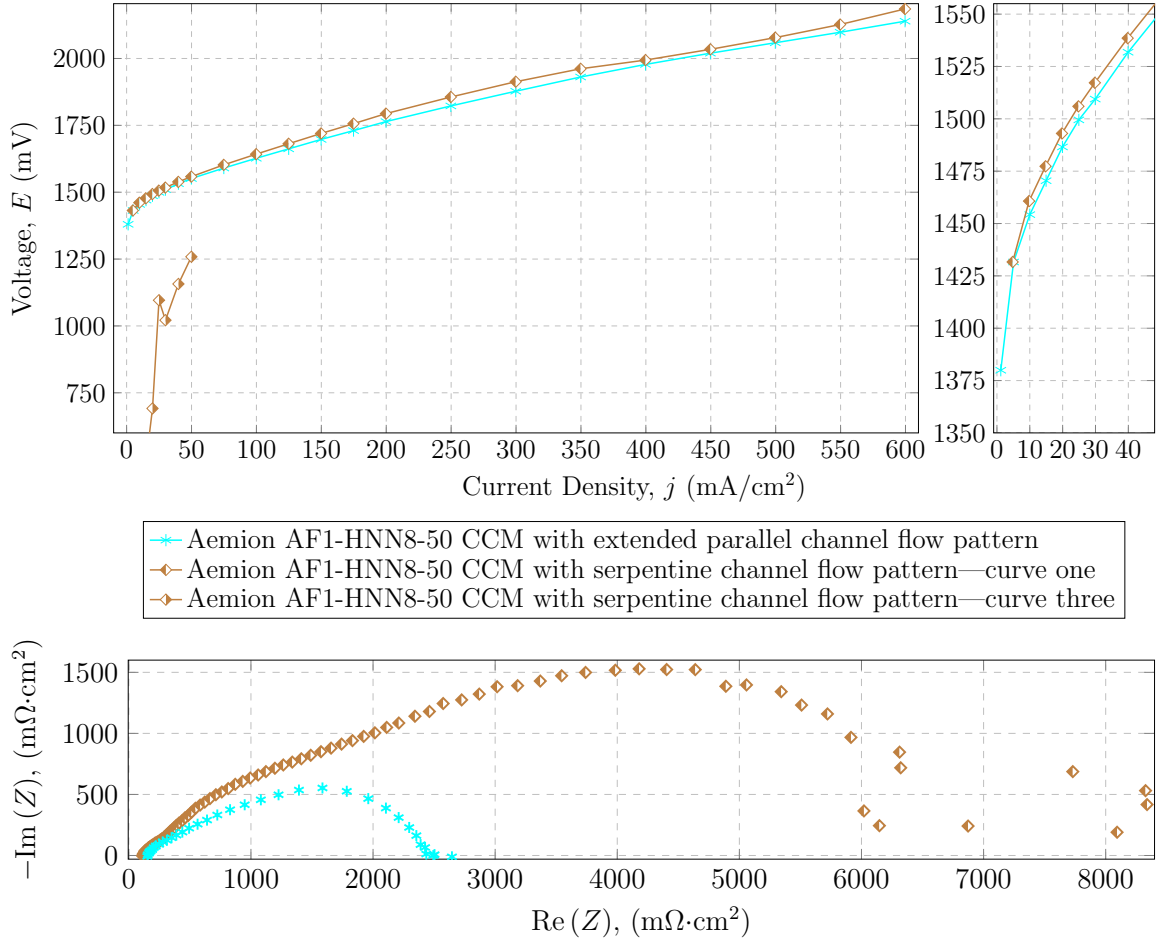


Figure 3.23 – Polarization curves and Nyquist plots (EIS obtained at 20 mA/cm²) for Aemion-based cells assembled with extended parallel and serpentine channel flow patterns. Cells operated at 60°C with 0.85 mol/L KOH fed to both electrodes.

From the Nyquist plots provided in Figure 3.23, the HFR for the cell tested with the extended parallel channel bipolar plates was found to be 25% higher than the HFR for the cell tested with the serpentine channel bipolar plates (153 vs. 116 mΩ·cm², respectively). The CTR data for the two cells could not be compared due to the instability observed for the cell utilizing the serpentine bipolar plates (the EIS data presented in Figure 3.23 was obtained after the first polarization curve). So while there were issues associated with sealing both plate designs with a non-laminated CCM, the serpentine channel plates produced a more viable cell with a lower HFR. As noted, the sealing of the cell was not necessarily directly due to the serpentine flow pattern, but because the flow pattern was restricted to within the 5 cm² perimeter of the active area. Future tests with more stable CCMs will be required to further analyze and validate the two flow patterns. Related to the

sealing of the cells, it is recommended that cells are tested to determine if they are adequately sealed prior to being operated. Tests of this nature, as per the United States Fuel Cell Council (USFCC), may be performed using helium gas and a mass flow controller [120]. Alternatively, the cell may be held at 1 V potentiostatically as electrolysis will not occur, but shunt currents due to crossover will (i.e., the current should remain approximately zero if the cell is properly sealed) [51].

3.2.3 Repeatability of CCM Cell Performance

In response to issues regarding the instability of some of the cell materials used, and the swelling of the CCMs, a number of adaptations, as discussed above in Section 3.2.2, were made to the cell assembly process. Since investigating each of these adaptations regarding gasket materials, gasket thicknesses, removing the lamination sheets, and changing the bipolar plate flow pattern required individually studying new CCMs, the repeatability of these results was not verified. It is important to recall that fabricating the CCMs themselves was not trivial as the failure rate was $\approx 30\%$. Despite the number of changes made to the various cells tested, a number of the resulting polarization curves, as seen in Figure 3.24, did generally demonstrate similar performance. It is for this reason that the results from this work are refereed to only as proof-of-concept as they must be further verified with more testing. Furthermore, it is for this reason that a statistical analysis regarding the uncertainty in the cell performances presented in the polarization curves has not been conducted. It is hypothesized that if the learnings from Section 3.2.2 are used to test future CCMs fabricated with the new Aemion AF2 membrane that demonstrates less swelling, that repeatable results may be obtained.

As an aside, it was observed that the cells tested with a higher cathode catalyst loading of $0.2 \text{ mg}_{\text{Pt}}/\text{cm}^2$ in Figure 3.24 had a similarly better performance compared to the cells tested with a lower loading of $0.1 \text{ mg}_{\text{Pt}}/\text{cm}^2$. This result is unexpected as the OER in the anode has been reported to be the rate-determining reaction for alkaline electrolyzers [18, 31] and therefore the anode IrO_x loading should be limiting, not the Pt loading in the cathode. This result may be due to issues regarding the aforementioned hydrophobicity of the cathode PTL used (Toray 90 with 5 wt.% PTFE) as the higher catalyst loading may yield an electrode that is not as susceptible to water transport issues (the thicker electrode may retain more water content). Although this result was unexpected, it has been deemed relatively inconsequential given that it must be further verified using an alternative cathode PTL, and furthermore, other non-PGM based catalysts, which will require different loadings, will likely be studied

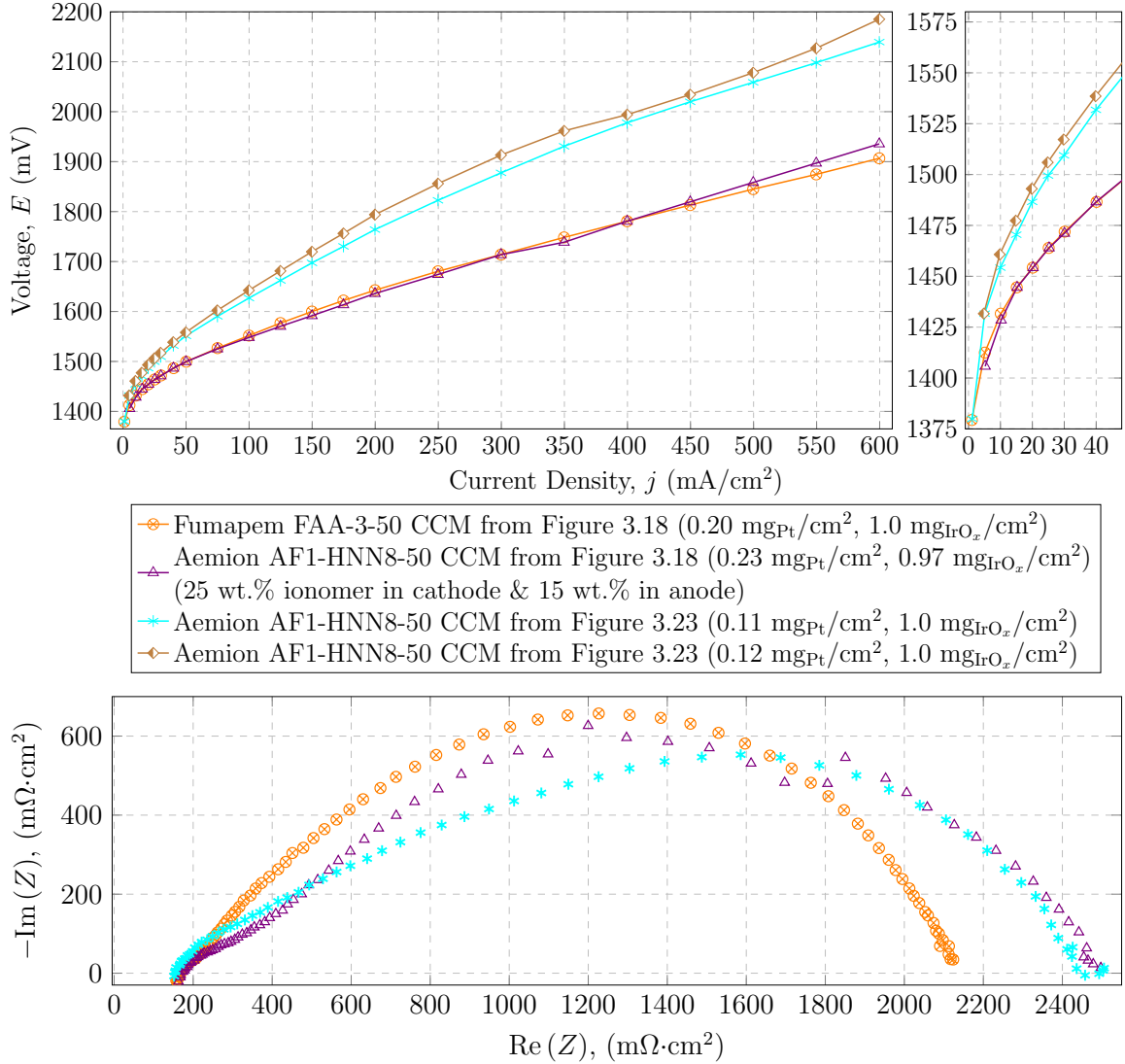


Figure 3.24 – Polarization curves and Nyquist plots (EIS obtained at 20 mA/cm²) for CCM-based cells with similar performances. Unless stated otherwise, all cell electrodes (anode & cathode) contained 15 wt.% ionomer (AP1-HNN8 ionomer). Cells operated at 60°C with 0.85 mol/L KOH fed to both electrodes.

in more detail in the future instead of Pt and Ir.

3.2.4 Proof-of-Concept CCM & CSS Cell Performance

While CCM fabrication and testing was the focus of this work, a single proof-of-concept CCS-based cell was also fabricated using the inkjet printing method to compare to the proof-of-concept CCM-based cell results. It was thought that despite a reduction in the direct contact between the membrane and the CLs compared to

a CCM-based cell, that the active area within the electrodes would be maintained by use of the aqueous KOH. As such, it was hypothesized that the CCS-based cell may have an improved kinetic performance compared to a CCM-based cell since the catalyst inks may enter the PTLs during the fabrication process and thereby increase the effective surface area of the electrodes.

The cathode for the CCS-based cell was produced by printing Aemion Pt|C Ink 0.3 onto Toray 90 with a loading of $0.13 \text{ mg}_{\text{Pt}}/\text{cm}^2$ while the anode was produced by printing Aemion IrO_x Ink 0.3 onto Bekipor Ni with a loading of $1.1 \text{ mg}_{\text{IrO}_x}/\text{cm}^2$. The loadings of the electrodes were measured by printing onto aluminum foil in the same manner as described for CCM fabrication. However, since there was a concern that the catalyst ink may flow through the pores of the PTLs and pass completely through them, the change in mass of the PTLs (after drying overnight) was used to verify the loadings found from the aluminum foil. The catalyst loadings found using the two methods were found to be the same such that it was concluded that the printed inks did not pass through the PTL materials¹⁴. The CCS-based cell was assembled in the same manner as a non-laminated CCM cell with 10 mil PTFE-coated fiberglass gaskets and serpentine flow pattern bipolar plates. The non-laminated 2 x 2 inch square piece of Aemion AF1-HNN8-50 membrane used for the cell was converted to hydroxide form following the procedure outlined in Section 3.1.4 prior to cell assembly.

As seen in Figure 3.25, the CCS-based cell out performed the CCM-based cell produced with the same catalyst loadings and operated with the same cell hardware. Although issues, as discussed above in the section on bipolar plates, were encountered with the CCM-based cell such that the CTR could not be determined from the EIS data, the HFR values of the CCM and CCS cells were found to be similar (116 and $102 \text{ m}\Omega\cdot\text{cm}^2$, respectively). As such, it was concluded that the primary reason for the difference in performance between the CCM- and CCS-based cells was their respective kinetic performances as initially hypothesized. Since the two cells were fabricated using the same materials and loadings, the increased kinetic performance of the CCS-based cell may indicate that the porosity of the CLs for the CCM-based cell may be too low. That is, if the porosity of the CLs is too low, then the reactants and products may not be sufficiently transported within the CL and therefore render some of the electrode underutilized. Note that this result may again be impacted by the use of the Toray 90 with PTFE content since the catalyst coated PTL may exhibit different water transport properties than the native PTL used in the CCM-based cell.

The EIS data for the CCS-based cell at various current densities (20, 300, and

¹⁴This was further verified by visual confirmation of no black catalyst ink material on the printer platen following the fabrication process for both electrodes.

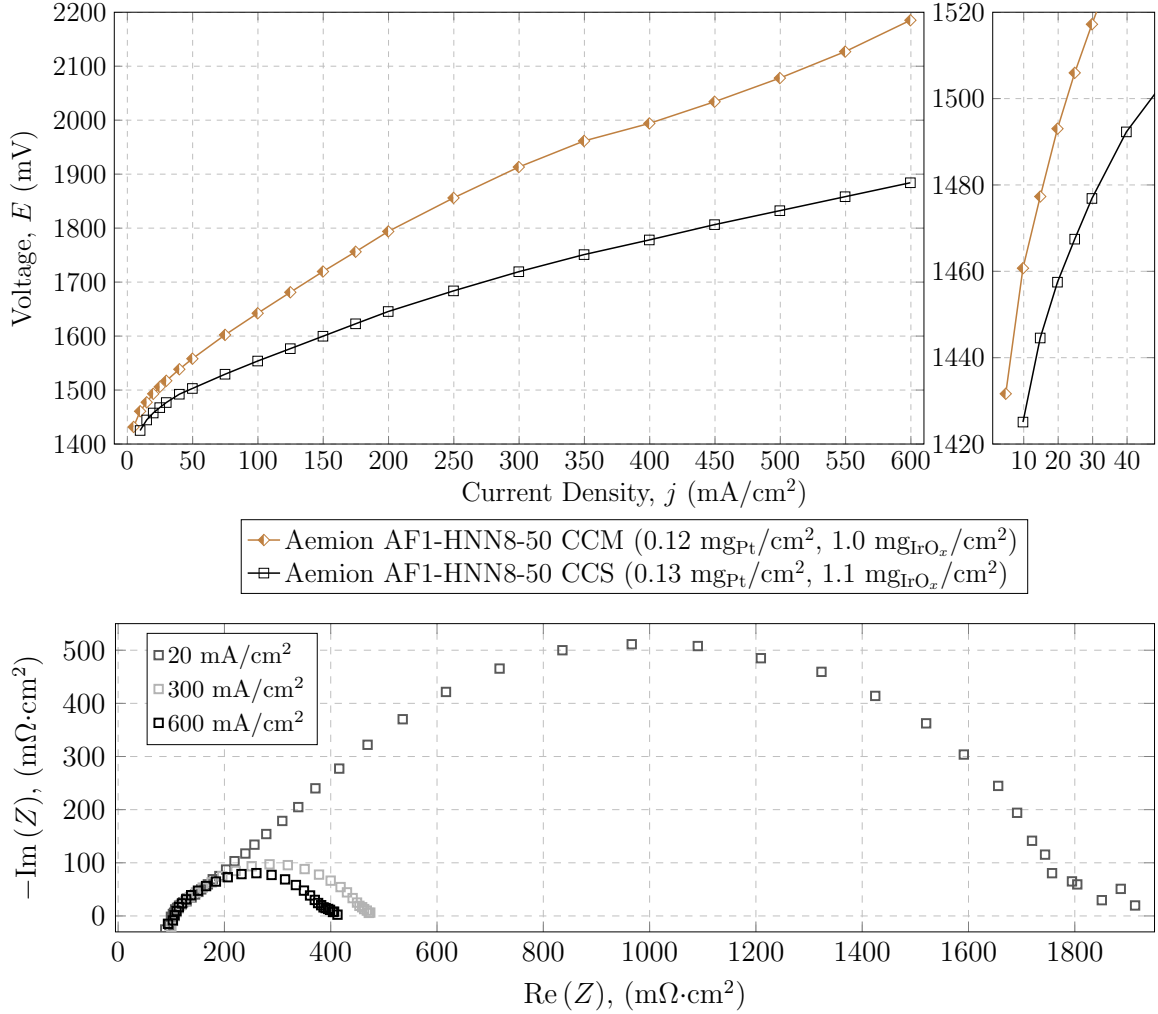


Figure 3.25 – Polarization curves and Nyquist plots for proof-of-concept CCM- and CCS-based Aemion AF1-HNN8-50 cells. Cells operated at 60°C with 0.85 mol/L KOH fed to both electrodes. Note that the EIS data for the CCM-based cell is not provided due to issues with the cell sealing.

600 mA/cm²) is provided in Figure 3.25 to demonstrate the trends in the HFR and CTR with respect to the current density. As expected for the HFR, the values remain approximately constant since the resistance of the cell does not change with respect to current density. Similarly, the CTR decreases with increasing current density as expected based upon the Butler-Volmer equation since the increased overpotential decreases the Faradaic resistance [7].

3.2.5 Comparison of Cell Performance to Literature

Due to practical considerations regarding the time required to produce relatively high catalyst loadings using the inkjet printing method, electrodes were produced with cat-

alyst loadings based upon the work of Mandal et al. for inkjet printed PEM-based CCMs [33]. Mandal et al. printed PEM-based CCMs with catalyst loadings of approximately $0.1 \text{ mg}_{\text{Pt}}/\text{cm}^2$ and $1 \text{ mg}_{\text{IrO}_x}/\text{cm}^2$ for the cathode and anode, respectively. However, compared to AEM-based electrolyzers fabricated using alternative methods such as spray coating, these loadings, especially for the cathode, were quite low. Published work by others using AEM-based materials by Ionomr Innovations Inc. have used anode catalyst loadings of $1\text{--}3.5 \text{ mg}_{\text{IrO}_x}/\text{cm}^2$ and cathode catalyst loadings of $0.5\text{--}1 \text{ mg}_{\text{Pt}}/\text{cm}^2$ [51, 57, 59]. It is for this reason that Figure 3.26 compares the best proof-of-concept cell performances obtained in this work to those obtained by Fortin et al. [57] and Koch et al. [59] based upon both current density, as well as a loading normalized current density. The loading normalized current densities were determined by dividing the current densities by the total catalyst loadings ($\text{mg}_{\text{Pt}}/\text{cm}^2 + \text{mg}_{\text{IrO}_x}/\text{cm}^2$). A comparative summary of the materials and testing conditions used herein and those by Fortin et al. [57] and Koch et al. [59] is provided in Table 3.8.

Based upon the current density polarization curves (non loading normalized) in Figure 3.26, it is clear that the cell performances obtained by Fortin et al. [57] and Koch et al. [59] are better than those obtained herein for both the CCM- and CCS-based cells. From the summary of HFR values provided in Table 3.9, the HFR value for the CCS-based cell from this work ($102 \text{ m}\Omega\cdot\text{cm}^2$) is similar to that obtained by Fortin et al. ($95 \text{ m}\Omega\cdot\text{cm}^2$) while being notably lower than the value obtained by Koch et al. ($270 \text{ m}\Omega\cdot\text{cm}^2$). The CCM-based cell from this work demonstrated in Figure 3.26 had a higher HFR value ($171 \text{ m}\Omega\cdot\text{cm}^2$), but was still lower than the value obtained by Koch et al. Note that the higher HFR value for the CCM-based cell compared to the CCS-based was not necessarily due to the CCM architecture, but because the cell was tested with the lamination sheets and the extended parallel flow channel bipolar plates (CCM details provided in Table 3.5). If the ohmic losses of the cell are approximated using the HFR ($\eta_{ohmic} = j\text{HFR}$), then the cell by Koch et al. had the highest ohmic losses, followed by the cells tested herein, and then the cell by Fortin et al. It is not clear why the HFR for the cell by Koch et al. was so high, but it is hypothesized to be due to the membrane since it contained a porous reinforcement layer which may reduce its ionic conductivity. Nonetheless, it was concluded that the poorer performance for the cells from this work compared to those from literature was not due to the ohmic losses, but due to the activation losses.

Regarding the concentration of KOH used in this work compared to that used by Fortin et al. [57] and Koch et al. [59] (0.85 vs. 1.0 mol/L , respectively), it has been shown that the HFR may decrease by $\approx 20\%$ by increasing the KOH concentration from 0.7 to 1 mol/L [66]. In the same study it was also demonstrated that the CTR

Table 3.8 – Comparative summary of AEM-based electrolyzers containing similar materials to the cells tested herein.

Characteristic	This Work	Fortin et al. [57]	Koch et al. [59]
Membrane	Aemion AF1-HNN8-50	Aemion AF1-HNN8-50	Aemion AF2-HLE7-25 ^a
Anode Catalyst	IrO _x (TKK)	Ir Black (Alfa Aesar)	IrO _x (Alfa Aesar)
Anode Catalyst Loading	1 mg/cm ²	3.5–3.8 mg/cm ²	1 mg/cm ²
Anode Ionomer/Binder	Aemion AP1-HNN8	Fumion FAA-3	Aemion AP2-HNN6
Anode Ionomer Loading	15 wt.% of CL	7 wt.% of CL	7 wt.% of CL
Anode PTL	Ni Felt (Bekaert)	Au Coated Ti (Bekaert)	Ti-felt (Bekaert, 2GDL40-1.0)
Cathode Catalyst	Pt C (60 wt.%, HyPlat)	Pt C (60 wt.%, Alfa Aesar)	Pt C (60 wt.%, Greenerity)
Cathode Catalyst Loading	0.1 mgPt/cm ²	1 mgPt/cm ²	0.5 mgPt/cm ²
Cathode Ionomer/Binder	Aemion AP1-HNN8	Fumion FAA-3	Aemion AP2-HNN6
Cathode Ionomer Loading	15 wt.% of CL	25 wt.% of CL	20 wt.% of CL
Cathode PTL	Toray 90	Toray 90	Carbon-based (H24C5, Freudenberg)
MEA Fabrication	CCM & CCS	CCS	CCM
Operating Temperature	60°C	60°C	60°C
KOH Concentration	0.85 mol/L	1 mol/L	1 mol/L
Cell Feed Method	Cathode & Anode	Cathode & Anode	Cathode & Anode ^b

^a Koch et al. utilized a newly developed membrane by Ionomr Innovations Inc. which includes a porous reinforcement layer infiltrated with Aemion AF2. The membrane had a thickness of 25 μm

^b The feed method used by Koch et al. was not explicitly stated, but was determined through email communication

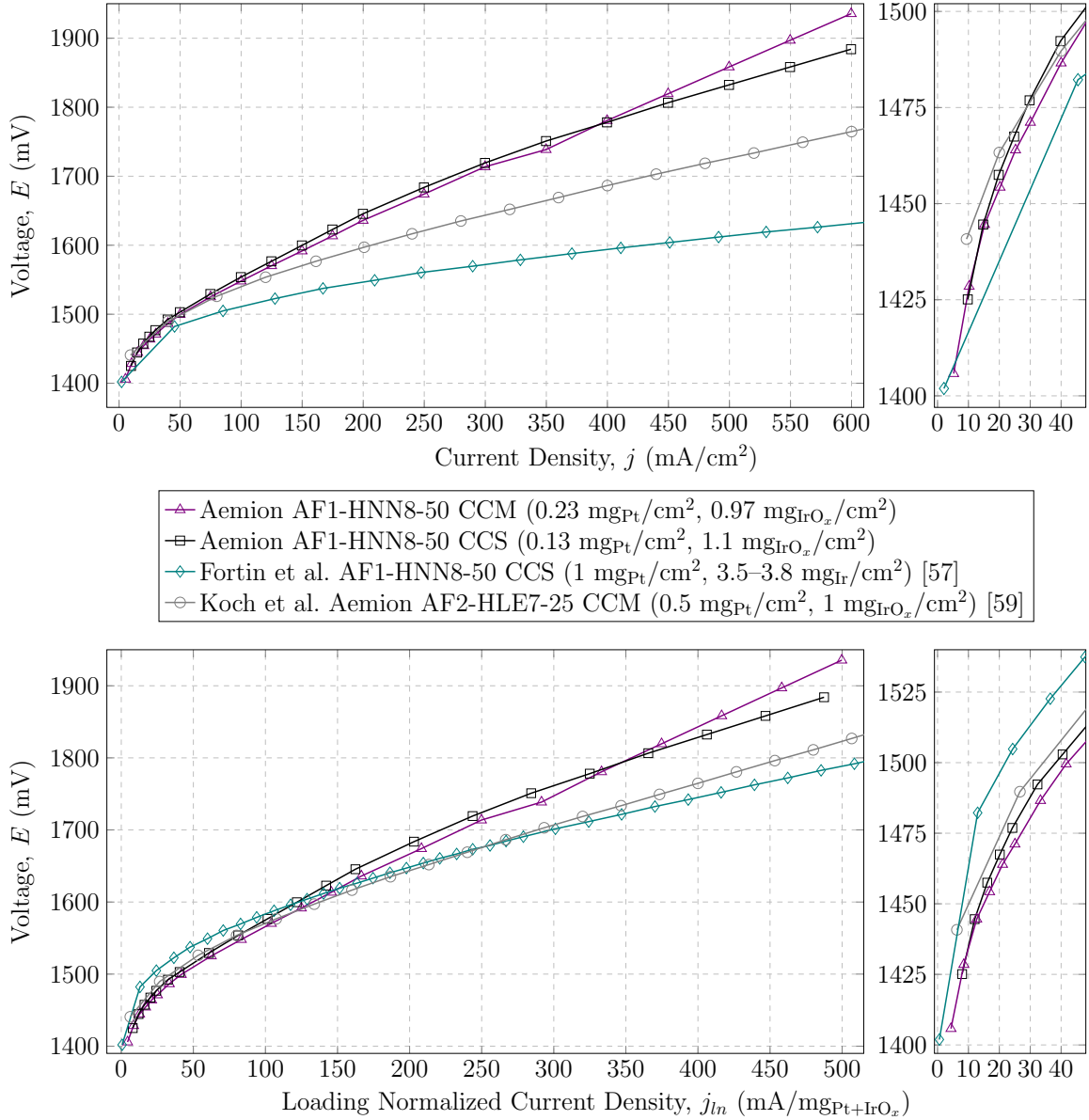


Figure 3.26 – Polarization curves comparing the best proof-of-concept results obtained herein to those from literature using similar materials and operating conditions. For a complete comparison of the materials and operating conditions refer to Table 3.8.

may increase by $\approx 2\%$ for the same change in KOH concentration [66]. As such, it is hypothesized that the HFR values for the cells tested herein may decrease if operated with 1 mol/L KOH, but that the CTR would not notably change.

Based upon the loading normalized cell performances in Figure 3.26, the cells from this work exhibited slightly better performance than cells from literature until 75–150 mA/mg_{Pt+IrO_x}, but are poorer thereafter. Since the poorer performance was

Table 3.9 – Comparison of HFR values for the cells from this work and those from literature.

Cell	HFR ($\text{m}\Omega\cdot\text{cm}^2$)
This work (AF1-HNN8 CCM)	171/116 ^a
This work (AF1-HNN8 CCS)	102
Fortin et al. [57] (AF1 HNN8-50 CCS)	95
Koch et al. [59] (AF2-HLE7-25 CCM)	270

^a The HFR for the CCM-based cell tested with the parallel channel bipolar plates and lamination sheets ($171 \text{ m}\Omega\cdot\text{cm}^2$) was greater than the cell tested with serpentine channel flow pattern bipolar plates and without lamination sheets ($116 \text{ m}\Omega\cdot\text{cm}^2$)

deemed not to be due to ohmic losses, it is hypothesized that the cells from this work exhibit a relatively high exchange current density, which gives them a better initial performance, but a relatively low Tafel slope, such that their performance is lower at higher currents. Note that a thorough Tafel analysis was not conducted since the activation losses could not be isolated to a single electrode (i.e., literature states the anode is limiting [18, 31], but the performance was also found to vary depending on the cathode catalyst loading in Figure 3.24). This hypothesis is supported by the work conducted by Koch et al. as they demonstrated (operating with 0.3 mol/L KOH) that the Tafel slope decreased from 92 to 73 mV/dec by decreasing the anode ionomer content from 15 to 7 wt.% while keeping all other parameters the same [59]. Performing a similar study for the cathode, Koch et al. found that using 10 or 20 wt.% ionomer content had a small effect on the overall cell performance. Fortin et al. also used 7 wt.% ionomer content in their anode and used Fumion FAA-3 ionomer instead of the AP1-HNN8 ionomer as they found the FAA-3 ionomer resulted in a higher performance. In short, the cell performance from this work was found to be poorer than those from literature, which is hypothesized to be related to the composition of the electrode (primarily the anodic ionomer loading), and not due to the electrode fabrication method (inkjet printing vs. spray coating).

3.2.6 Cell Stability

The short term stability of the proof-of-concept CCM- and CCS-based cells was evaluated by operating them potentiostatically at 1.8 V for a period of two hours. As seen in Figure 3.27, both the CCM- and CCS-based cells demonstrated an exponential decay in their operating current densities at 1.8 V. Note that the CCM-based

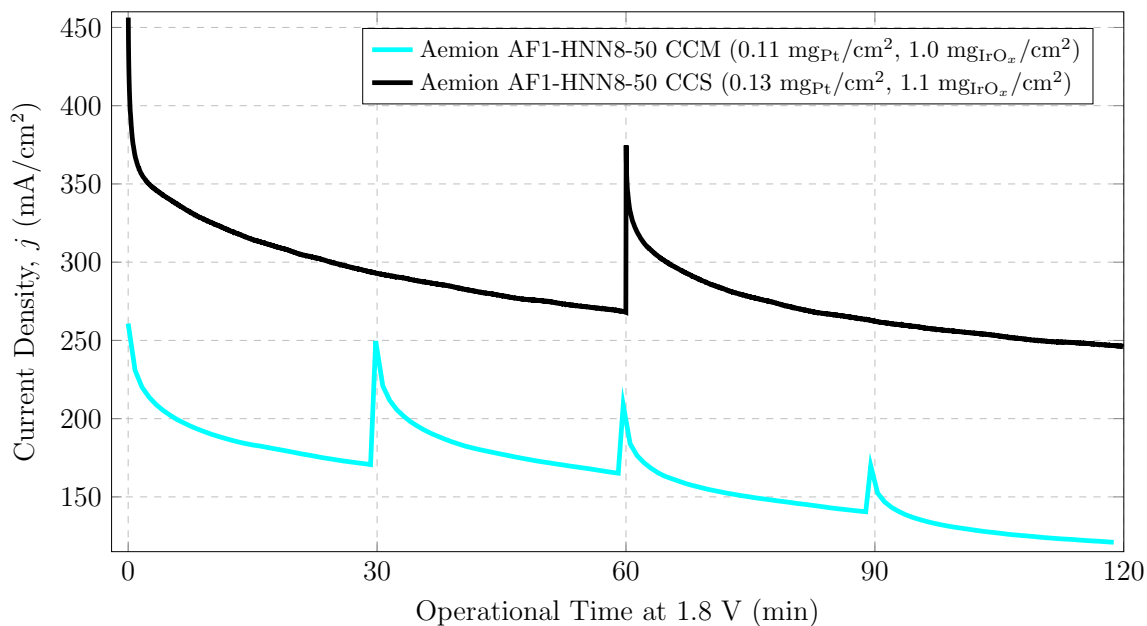
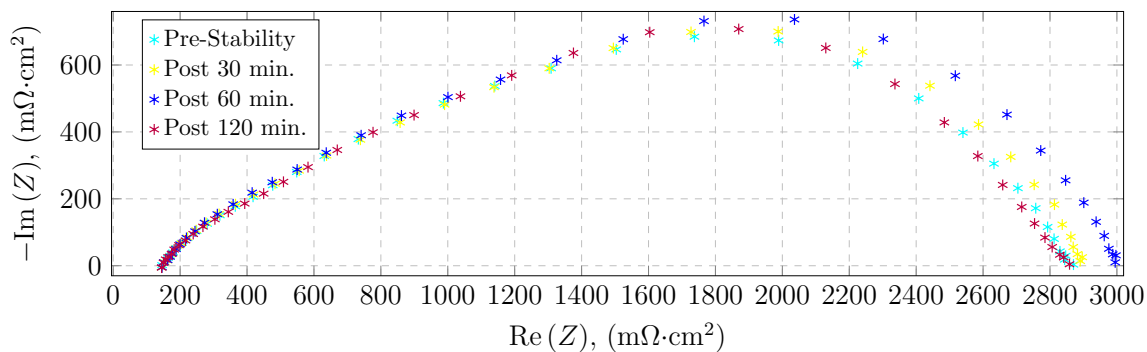


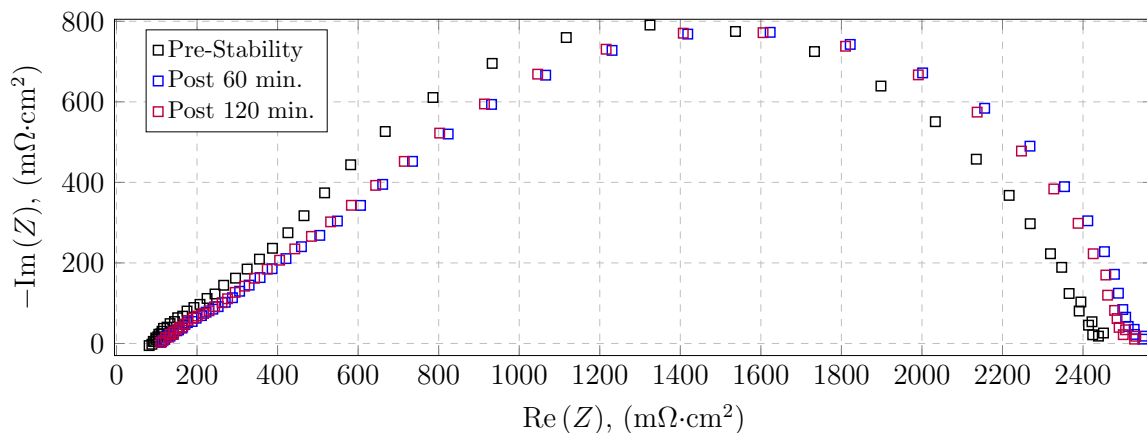
Figure 3.27 – Current densities obtained during potentiostatic testing for select Aemion-based cells. EIS performed every 60 minutes for the CCS-based cell and every 30 minutes for the CCM-based cell.

cell results provided in Figure 3.27 are for a cell tested with the parallel channel bipolar plates and lamination sheets (CCM details provided in Table 3.6). The stark increase in current density every 30 minutes for the CCM-based cell and at 60 minutes for the CCS-based cell correspond to when EIS experiments were conducted. Since the operating current densities partially increased back to their initial values after performing the EIS tests, which required the cells to be disconnected from the test-station power supply and connected to the potentiostat, it is hypothesized that part of the exponential decay in the current density is operationally related and non-permanent. However, because the current densities are not fully regained, it suggests that the cells undergo some form of permanent degradation.

From the Nyquist plots provided in Figure 3.28, the HFR for the CCM-based cell (Figure 3.28a) remained consistent during the short-term stability testing while the HFR for the CCS-based cell (Figure 3.28b) initially increased and then remained consistent as well. As for the CTR for the CCM- and CCS-based cells in Figure 3.28, the values appeared to increase with operating time, with the exception of the last test, in which it decreased for both cells. However, because the CTR requires the low-frequency intercept, which, especially for the CCS-based cell, was prone to drift, it is difficult to make concise conclusions from the EIS results. Note that the drift correction option for the SP-300 Biologic potentiostat was used for the EIS tests, but



(a) For Aemion AF1-HNN8-50 CCM-based cell.



(b) For Aemion AF1-HNN8-50 CCS-based cell.

Figure 3.28 – Nyquist impedance plots for CCM- and CCS-based cells during two hours of potentiostatic stability testing. EIS data obtained at 20 mA/cm².

that results still demonstrate drift, which may be an indication of cell instability (i.e., there is drift in the results because the cells degrade during the EIS tests). From pre- and post-operational microscopy images of the CCM, as seen in Figure 3.29, it was concluded that the decrease in cell performance was due to CL detachment from the membrane. Note that the large black sections observed in Figure 3.29b are sections where the CL did not delaminate from the membrane and correspond to wrinkled portions of the CCM. Conversely, the relatively consistent HFR values, which are relatively unaffected by drift by virtue of being in the high-frequency domain, suggest that the membrane was stable for the short-term potentiostatic testing. Although Fortin et al. conducted their cell stability tests galvanostatically (500 mA/cm², 0.1 mol/L KOH, and 50°C), they observed a similar result where the Aemion AF1-HNN8 membrane was stable (consistent HFR), but the CTR increased as the CLs were found to dissolve/delaminate [57].

Although little was done in this work to further investigate issues regarding the

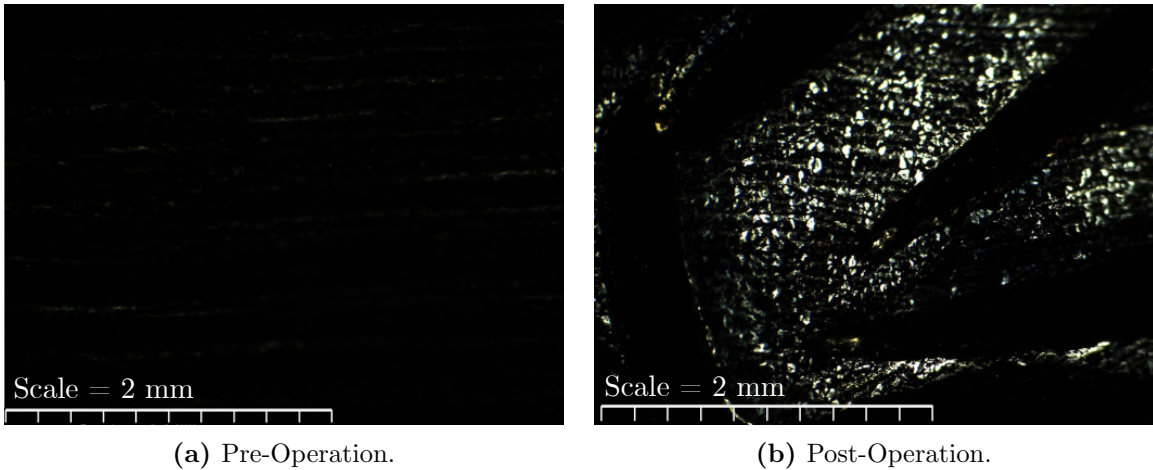


Figure 3.29 – Microscopy images of an Aemion AF1-HNN8-50 CCM before and after water electrolysis operation.

stability of the CLs, a recent publication by Li et al. [73] on AEM-based water electrolyzer durability discussed the following potential issues:

◇ Ionomer detachment:

The low gas permeability of alkaline ionomers makes it difficult to remove the evolved gasses fast enough from the catalyst-ionomer interface at high current densities, which can then lead to the detachment of the ionomer. Another issue is that high IEC ionomers have high water uptake which decreases their adhesion to the catalyst surface.

◇ Ionomer poisoning:

The phenyl groups commonly present in alkaline ionomers may be oxidized by OER catalysts such as IrO_x .

Potential mitigation strategies for the former issue include using less ionomer (which should also improve performance), using low IEC ionomers (at the sacrifice of CL ionic conductivity, and possibly, performance), operating at low temperatures (again, at the sacrifice of performance), or using high IEC ionomers that have low to moderate water uptake (properties commonly at odds with one-another). A mitigation strategy for the latter issue is to use OER catalysts with low phenyl group adsorption energy, which may be done by alloying materials such as Ir [73].

Chapter 4

Conclusions & Future Work

To realize the potential of hydrogen gas as an alternative energy carrier used to displace the use of non-renewable resources such as oil and gas, production technologies such as anion exchange membrane (AEM) water electrolysis must be further developed by increasing performance while concurrently keeping costs low [23, 28]. While the development of AEM-based water electrolyzers is primarily only at the laboratory stage [23], it is important to be able to fabricate electrodes in a controllable and repeatable manner. As such, the principal objective of this work was to test the suitability of inkjet printing as a fabrication method for AEM-based water electrolyzer electrodes. Stemming from this primary objective, three additional secondary goals were identified: catalyst ink development, test-station development, and electrode fabrication/cell testing.

4.1 Conclusions

Regarding the primary and secondary goals for this work, Pt|C- and IrO_x-based catalyst inks containing Aemion AP1-HNN8 ionomer were developed for inkjet printing, the test-station was designed, tested, and validated, and a series of CCM- and CCS-based AEM electrolyzers were tested. However, because the specific anion conducting materials used for this work have more-or-less been deprecated (Ionomr Innovations Inc. has developed an AP2 ionomer and AF2 membrane in place of AP1 and AF1), the contributions from this work primarily stem from the developed methodologies.

From Chapter 2 on catalyst ink development, DLS was demonstrated to be a useful tool for catalyst ink development as it can be used to observe the effect of different ink formulation methodologies. For this work specifically, catalyst ink consistency was improved by minimizing the viscosity of both the ionomer solution and the catalyst slurry prior to their mixing. The use of DLS enables the elucidation of negatively

contributing effects on the catalyst ink consistency (e.g., the ionomer and catalyst solutions may be studied independently or together).

From Chapter 3 on electrode fabrication and cell testing, it was demonstrated that, although electrode fabrication can be challenging when using materials that are dimensionally unstable, the inkjet printing method can be used to produce electrodes that perform similarly to literature (specifically for the catalyst loading normalized results). Comparisons to literature are often difficult due to inconsistencies in cell materials, operation, and testing procedures, however an attempt to generally compare obtained results to published results up until the beginning of 2020 is provided in Figure 4.1. The current densities obtained at 1.8 V for the CCM- and CCS-based cells from this work fall between the 75th and 90th percentile compared to others in literature. Furthermore, the values obtained herein (438 and 424 mA/cm² for CCS and CCM, respectively) are both approximately double the average values. Of note is that the value obtained by Fortin et al. [57] of 1845 mA/cm² at 1.8 V is an extremely high outlier (not pictured in Figure 4.1).

In summary, the main contributions from this work are:

- ◊ The development of Pt|C- and IrO_x-based catalyst inks with an anion conducting ionomer that are suitable for use with inkjet printing.

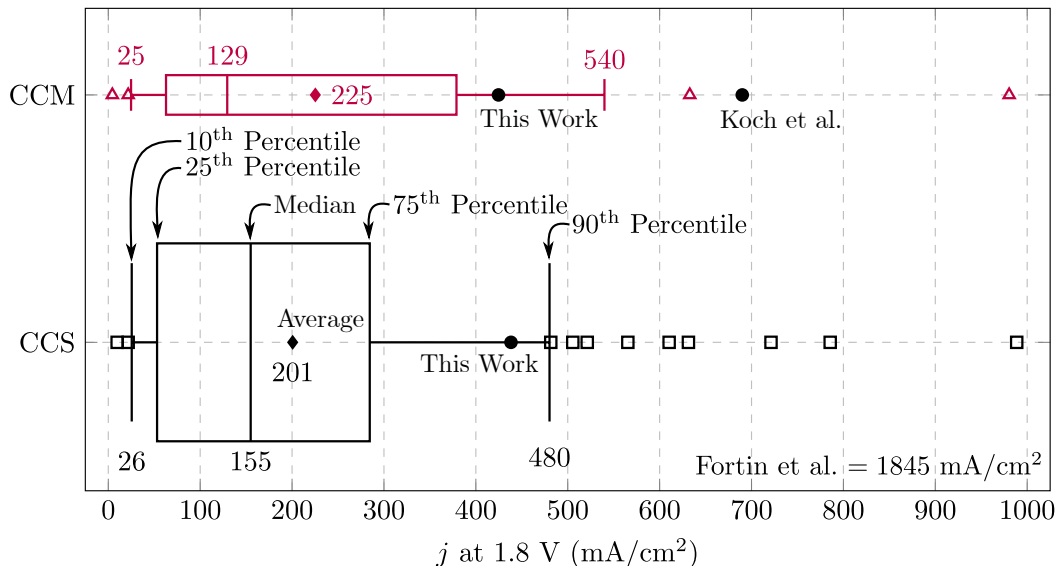


Figure 4.1 – Comparison of AEM-based electrolyzer current densities achieved at 1.8 V. Data for distributions obtained from Miller et al. [28] with 30 citations for CCS data and 17 for CCM data. Distribution values do not incorporate data from Fortin et al. [57], Koch et al. [59], or the results obtained from this work.

- ◇ The development of a test-station and suitable protocols to study the performance of AEM-based water electrolyzers.
- ◇ The demonstration of the first inkjet printed electrodes (CCM- and CCS-based) for AEM-based water electrolyzers.

4.2 Future Work

Since AEM-based water electrolysis is primarily only at the laboratory stage of development, the equipment and methodologies from this work may be used to conduct an immense number of future tests. From a broad perspective, each of the primary literature review sections in Chapter 1 on cell materials (electrocatalysts, AEM membranes and ionomers, PTLs, and bipolar plates), cell assembly and fabrication (CCM or CCS), and operation (liquid electrolyte and feed method), may each be studied as complex research topics. Moreover, the durability of the cells, which is highly correlated with the aforementioned research topics, has also been highlighted by Li et al. [73] to be a subject rife with future work.

From a more narrow perspective related specifically to the future work stemming from Chapter 2:

- ◇ Surface tension measurements for the catalyst inks should be conducted such that the Ohnesorge number may be determined. This may help guide future ink development since the Ohnesorge number may be compared to values from literature.
- ◇ Refractive index (RI) measurements should be further investigated and validated since the RI notably contributes to the uncertainty in the obtained DLS results.
- ◇ Rheology tests of the ionomer solutions should be performed in an effort to determine if the viscosities obtained from glass kinematic viscometers may be used for DLS.

Stemming specifically from Chapter 3, newly developed AEM materials such as Aemion AF2/AP2 or those by W7Energy (PiperION [51]), must be tested in an effort to obtain a repeatable baseline cell performance. Once repeatable results have been obtained, any of the aforementioned research topics may be investigated. To obtain repeatable results, the following experimental parameters are suggested:

- ◇ Utilize Aemion AF2-HNN8-50 membrane and AP2-HNN8 ionomer owing to their reduced swelling ratios.
- ◇ Utilize a non-laminated CCM with bipolar plates that have a flow field restricted to the active area of the cell.
- ◇ Since PTFE in the cathode PTL was hypothesized to introduce issues for the cell, it is recommended that a PTL with no PTFE content is utilized. If AvCarb MGL280 [117] is used, then the same 6 mil PTFE-coated fiberglass gaskets may be used to obtain a pinch value of 50 μm .
- ◇ To stay inline with the work conducted herein, the cell should be operated at 60°C with KOH fed to both the cathode and anode electrodes. To be more inline with the work from literature, a higher KOH concentration of 1 mol/L should be utilized.
- ◇ Polarization curve and EIS experiments may be conducted in the same manner as for this work, but potentiostatic EIS at 1.8 V should be used for the stability tests to match the testing conditions.

Recalling that three CCMs are typically fabricated at a time, both intra- and inter-batch CCM repeatability should be verified by comparing results obtained from CCMs in the same batch, as well as results obtained from CCMs from different batches. Upon doing so, some initial studies that may be conducted include:

- ◇ Anode ionomer content:
It should be verified that using a lower ionomer content of ≈ 7 wt.% improves cell performance.
- ◇ Cathode Pt|C loading:
A study should be performed with varying cathode catalyst loadings to verify that the cathode is not limiting.
- ◇ Cathode PTL PTFE content:
Tests may be conducted with cathode PTLs with varying PTFE content to investigate whether the hydrophobicity in the cathode PTL affects the cell performance.

References

- [1] John S. Rigden. *Hydrogen: The Essential Element*. Cambridge, Mass.: Harvard University Press, 2003. 280 pp. ISBN: 978-0-674-01252-3.
- [2] International Energy Agency. *The Future of Hydrogen: Seizing Today's Opportunities*. 2019. ISBN: 978-92-64-41873-8.
- [3] Julian R.H. Ross. “An Introduction to Heterogeneous Catalysis and Its Development Through the Centuries—Chemistry in Two Dimensions”. In: *Contemporary Catalysis*. Elsevier, 2019, pp. 3–38. ISBN: 978-0-444-63474-0.
- [4] James G. Speight. “Fouling During Hydrotreating”. In: *Fouling in Refineries*. Elsevier, 2015, pp. 303–328. ISBN: 978-0-12-800777-8.
- [5] Valentin Vogl, Max Åhman, and Lars J. Nilsson. “Assessment of Hydrogen Direct Reduction for Fossil-Free Steelmaking”. In: *Journal of Cleaner Production* 203 (Dec. 2018), pp. 736–745. ISSN: 09596526.
- [6] Intergovernmental Panel on Climate Change. *Global Warming of 1.5C. An IPCC Special Report on the Impacts of Global Warming of 1.5C above Pre-Industrial Levels and Related Global Greenhouse Gas Emission Pathways, in the Context of Strengthening the Global Response to the Threat of Climate Change, Sustainable Development, and Efforts to Eradicate Poverty*. 2018.
- [7] Ryan P. O’Hayre et al. *Fuel Cell Fundamentals*. Third edition. Hoboken, New Jersey: John Wiley & Sons Inc, 2016. 1 p. ISBN: 978-1-119-11415-4 978-1-119-11420-8.
- [8] Paul E. Dodds et al. “Hydrogen and Fuel Cell Technologies for Heating: A Review”. In: *International Journal of Hydrogen Energy* 40.5 (Feb. 2015), pp. 2065–2083. ISSN: 03603199.
- [9] Erik Wolf. “Large-Scale Hydrogen Energy Storage”. In: *Electrochemical Energy Storage for Renewable Sources and Grid Balancing*. Elsevier, 2015. ISBN: 978-0-444-62616-5.
- [10] International Energy Agency. *World Energy Outlook 2019*. 2019.
- [11] Environment and Climate Change Canada. *Greenhouse Gas Emissions*. URL: <https://www.canada.ca/en/environment-climate-change/services/environmental-indicators/greenhouse-gas-emissions.html> (visited on 04/16/2020).

- [12] D. G. Bessarabov et al., eds. *PEM Electrolysis for Hydrogen Production: Principles and Applications*. CRC Press, 2016. 389 pp. ISBN: 978-1-4822-5232-3.
- [13] Merit Bodner, Astrid Hofer, and Viktor Hacker. “H₂ Generation from Alkaline Electrolyzer”. In: *Wiley Interdisciplinary Reviews: Energy and Environment* 4.4 (July 2015), pp. 365–381. ISSN: 20418396.
- [14] Agata Godula-Jopek. *Hydrogen Production : By Electrolysis*. 1st ed. Wiley-VCH, 2015. 402 pp. ISBN: 978-3-527-33342-4.
- [15] Marcelo Carmo et al. “A Comprehensive Review on PEM Water Electrolysis”. In: *International Journal of Hydrogen Energy* 38.12 (Apr. 2013), pp. 4901–4934.
- [16] F. Gutmann and Oliver J. Murphy. “The Electrochemical Splitting of Water”. In: *Modern Aspects of Electrochemistry*. Ed. by Ralph E. White, J. O’M. Bockris, and B. E. Conway. Boston, MA: Springer US, 1983, pp. 1–82. ISBN: 978-1-4615-7463-7 978-1-4615-7461-3.
- [17] R Gilliam et al. “A Review of Specific Conductivities of Potassium Hydroxide Solutions for Various Concentrations and Temperatures”. In: *International Journal of Hydrogen Energy* 32.3 (Mar. 2007), pp. 359–364. ISSN: 03603199.
- [18] Congling Hu, Lei Zhang, and Jinlong Gong. “Recent Progress Made in the Mechanism Comprehension and Design of Electrocatalysts for Alkaline Water Splitting”. In: *Energy & Environmental Science* 12.9 (2019), pp. 2620–2645. ISSN: 1754-5692, 1754-5706.
- [19] D. G. Bessarabov et al., eds. *PEM Electrolysis for Hydrogen Production: Principles and Applications*. Boca Raton, Florida: CRC Press, 2016. 389 pp. ISBN: 978-1-4822-5232-3.
- [20] P. Trinke et al. “Hydrogen Crossover in PEM and Alkaline Water Electrolysis: Mechanisms, Direct Comparison and Mitigation Strategies”. In: *Journal of The Electrochemical Society* 165.7 (2018), F502–F513. ISSN: 0013-4651, 1945-7111.
- [21] Katherine Ayers. “The Potential of Proton Exchange Membrane–Based Electrolysis Technology”. In: *Current Opinion in Electrochemistry* 18 (Dec. 2019), pp. 9–15. ISSN: 24519103.
- [22] Muhammad Arif Khan et al. “Recent Progresses in Electrocatalysts for Water Electrolysis”. In: *Electrochemical Energy Reviews* 1.4 (Dec. 2018), pp. 483–530. ISSN: 2520-8489, 2520-8136.
- [23] Immanuel Vincent and Dmitri Bessarabov. “Low Cost Hydrogen Production by Anion Exchange Membrane Electrolysis: A Review”. In: *Renewable and Sustainable Energy Reviews* 81 (Jan. 2018), pp. 1690–1704. ISSN: 13640321.
- [24] Yongjun Leng et al. “Solid-State Water Electrolysis with an Alkaline Membrane”. In: *Journal of the American Chemical Society* 134.22 (June 6, 2012), pp. 9054–9057. ISSN: 0002-7863, 1520-5126.

- [25] Hiroshi Ito et al. “Pressurized Operation of Anion Exchange Membrane Water Electrolysis”. In: *Electrochimica Acta* 297 (Feb. 2019), pp. 188–196. ISSN: 00134686.
- [26] K. E. Ayers et al. “Characterization of Anion Exchange Membrane Technology for Low Cost Electrolysis”. In: *ECS Transactions* 45.23 (Apr. 2, 2013), pp. 121–130. ISSN: 1938-6737, 1938-5862.
- [27] Li Xiao et al. “First Implementation of Alkaline Polymer Electrolyte Water Electrolysis Working Only with Pure Water”. In: *Energy & Environmental Science* 5.7 (2012), p. 7869. ISSN: 1754-5692, 1754-5706.
- [28] Hamish Andrew Miller et al. “Green Hydrogen from Anion Exchange Membrane Water Electrolysis: A Review of Recent Developments in Critical Materials and Operating Conditions”. In: *Sustainable Energy & Fuels* 4.5 (2020), pp. 2114–2133. ISSN: 2398-4902.
- [29] Wenchao Sheng et al. “Correlating the Hydrogen Evolution Reaction Activity in Alkaline Electrolytes with the Hydrogen Binding Energy on Monometallic Surfaces”. In: *Energy & Environmental Science* 6.5 (2013), p. 1509. ISSN: 1754-5692, 1754-5706.
- [30] Charles C. L. McCrory et al. “Benchmarking Hydrogen Evolving Reaction and Oxygen Evolving Reaction Electrocatalysts for Solar Water Splitting Devices”. In: *Journal of the American Chemical Society* 137.13 (Apr. 8, 2015), pp. 4347–4357. ISSN: 0002-7863, 1520-5126.
- [31] Katherine Ayers et al. “Perspectives on Low-Temperature Electrolysis and Potential for Renewable Hydrogen at Scale”. In: *Annual Review of Chemical and Biomolecular Engineering* 10.1 (June 7, 2019), pp. 219–239. ISSN: 1947-5438, 1947-5446.
- [32] Dongyu Xu et al. “Earth-Abundant Oxygen Electrocatalysts for Alkaline Anion-Exchange-Membrane Water Electrolysis: Effects of Catalyst Conductivity and Comparison with Performance in Three-Electrode Cells”. In: *ACS Catalysis* 9.1 (Jan. 4, 2019), pp. 7–15. ISSN: 2155-5435, 2155-5435.
- [33] Manas Mandal et al. “Analysis of Inkjet Printed Catalyst Coated Membranes for Polymer Electrolyte Electrolyzers”. In: *Journal of The Electrochemical Society* 165.7 (2018), F543–F552. ISSN: 0013-4651, 1945-7111.
- [34] Kimberly F. L. Hagesteijn, Shanxue Jiang, and Bradley P. Ladewig. “A Review of the Synthesis and Characterization of Anion Exchange Membranes”. In: *Journal of Materials Science* 53.16 (Aug. 2018), pp. 11131–11150. ISSN: 0022-2461, 1573-4803.
- [35] Shimshon Gottesfeld et al. “Anion Exchange Membrane Fuel Cells: Current Status and Remaining Challenges”. In: *Journal of Power Sources* 375 (Jan. 2018), pp. 170–184. ISSN: 03787753.

- [36] Géraldine Merle, Matthias Wessling, and Kitty Nijmeijer. “Anion Exchange Membranes for Alkaline Fuel Cells: A Review”. In: *Journal of Membrane Science* 377.1-2 (July 2011), pp. 1–35. ISSN: 03767388.
- [37] Andrew G. Wright et al. “Hexamethyl-p-Terphenyl Poly(Benzimidazolium): A Universal Hydroxide-Conducting Polymer for Energy Conversion Devices”. In: *Energy & Environmental Science* 9.6 (2016), pp. 2130–2142. ISSN: 1754-5692, 1754-5706.
- [38] Noga Ziv and Dario R. Dekel. “A Practical Method for Measuring the True Hydroxide Conductivity of Anion Exchange Membranes”. In: *Electrochemistry Communications* 88 (Mar. 2018), pp. 109–113. ISSN: 13882481.
- [39] Scribner Associates. *740 Membrane Test System*. URL: <https://www.scribner.com/products/membrane-conductivity-testing/740-membrane-test-system/> (visited on 05/14/2021).
- [40] Lunyang Liu, Wenduo Chen, and Yunqi Li. “An Overview of the Proton Conductivity of Nafion Membranes through a Statistical Analysis”. In: *Journal of Membrane Science* 504 (Apr. 15, 2016), pp. 1–9. ISSN: 0376-7388.
- [41] Claudiu C. Pavel et al. “Highly Efficient Platinum Group Metal Free Based Membrane-Electrode Assembly for Anion Exchange Membrane Water Electrolysis”. In: *Angewandte Chemie International Edition* 53.5 (Jan. 27, 2014), pp. 1378–1381. ISSN: 14337851.
- [42] Sang Hyun Ahn et al. “Development of a Membrane Electrode Assembly for Alkaline Water Electrolysis by Direct Electrodeposition of Nickel on Carbon Papers”. In: *Applied Catalysis B: Environmental* 154–155 (July 2014), pp. 197–205. ISSN: 09263373.
- [43] Sang Hyun Ahn et al. “Anion Exchange Membrane Water Electrolyzer with an Ultra-Low Loading of Pt-Decorated Ni Electrocatalyst”. In: *Applied Catalysis B: Environmental* 180 (Jan. 2016), pp. 674–679. ISSN: 09263373.
- [44] Immanuel Vincent, Andries Kruger, and Dmitri Bessarabov. “Development of Efficient Membrane Electrode Assembly for Low Cost Hydrogen Production by Anion Exchange Membrane Electrolysis”. In: *International Journal of Hydrogen Energy* 42.16 (Apr. 2017), pp. 10752–10761. ISSN: 03603199.
- [45] Immanuel Vincent, Andries Krüger, and Dmitri Bessarabov. “Hydrogen Production by Water Electrolysis with an Ultrathin Anion-Exchange Membrane (AEM)”. In: (2018).
- [46] I.V. Pushkareva et al. “Comparative Study of Anion Exchange Membranes for Low-Cost Water Electrolysis”. In: *International Journal of Hydrogen Energy* (Nov. 2019), S0360319919341588. ISSN: 03603199.
- [47] Eun Joo Park et al. “Chemically Durable Polymer Electrolytes for Solid-State Alkaline Water Electrolysis”. In: *Journal of Power Sources* 375 (Jan. 2018), pp. 367–372. ISSN: 03787753.

- [48] Min Kyung Cho et al. “Alkaline Anion Exchange Membrane Water Electrolysis: Effects of Electrolyte Feed Method and Electrode Binder Content”. In: *Journal of Power Sources* 382 (Apr. 2018), pp. 22–29. ISSN: 03787753.
- [49] Hiroshi Ito et al. “Investigations on Electrode Configurations for Anion Exchange Membrane Electrolysis”. In: *Journal of Applied Electrochemistry* 48.3 (Mar. 2018), pp. 305–316. ISSN: 0021-891X, 1572-8838.
- [50] Zengcai Liu et al. “The Effect of Membrane on an Alkaline Water Electrolyzer”. In: *International Journal of Hydrogen Energy* 42.50 (Dec. 2017), pp. 29661–29665. ISSN: 03603199.
- [51] Grace A. Lindquist et al. “Performance and Durability of Pure-Water-Fed Anion Exchange Membrane Electrolyzers Using Baseline Materials and Operation”. In: *ACS Applied Materials & Interfaces* (Aug. 10, 2021), acsami.1c06053. ISSN: 1944-8244, 1944-8252.
- [52] Ji Eun Park et al. “High-Performance Anion-Exchange Membrane Water Electrolysis”. In: *Electrochimica Acta* 295 (Feb. 2019), pp. 99–106. ISSN: 00134686.
- [53] Alaa Faid et al. “Highly Active Nickel-Based Catalyst for Hydrogen Evolution in Anion Exchange Membrane Electrolysis”. In: *Catalysts* 8.12 (Dec. 3, 2018), p. 614. ISSN: 2073-4344.
- [54] T. Pandiarajan, L. John Berchmans, and S. Ravichandran. “Fabrication of Spinel Ferrite Based Alkaline Anion Exchange Membrane Water Electrolysers for Hydrogen Production”. In: *RSC Advances* 5.43 (2015), pp. 34100–34108. ISSN: 2046-2069.
- [55] A. Carbone et al. “Assessment of the FAA3-50 Polymer Electrolyte in Combination with a NiMn₂O₄ Anode Catalyst for Anion Exchange Membrane Water Electrolysis”. In: *International Journal of Hydrogen Energy* 45.16 (Mar. 2020), pp. 9285–9292. ISSN: 03603199.
- [56] Emily Cossar et al. “The Performance of Nickel and Nickel-Iron Catalysts Evaluated As Anodes in Anion Exchange Membrane Water Electrolysis”. In: *Catalysts* 9.10 (Sept. 27, 2019), p. 814. ISSN: 2073-4344.
- [57] Patrick Fortin et al. “High-Performance Alkaline Water Electrolysis Using Aemion™ Anion Exchange Membranes”. In: *Journal of Power Sources* 451 (Mar. 2020), p. 227814. ISSN: 03787753.
- [58] Li Wang et al. “High Performance Anion Exchange Membrane Electrolysis Using Plasma-Sprayed, Non-Precious-Metal Electrodes”. In: *ACS Applied Energy Materials* 2.11 (Nov. 25, 2019), pp. 7903–7912. ISSN: 2574-0962, 2574-0962.
- [59] Susanne Koch et al. “The Effect of Ionomer Content in Catalyst Layers in Anion-Exchange Membrane Water Electrolyzers Prepared with Reinforced Membranes (Aemion+™)”. In: *Journal of Materials Chemistry A* 9.28 (2021), pp. 15744–15754. ISSN: 2050-7488, 2050-7496.
- [60] *Enapter: About Us*. Enapter. URL: <https://www.enapter.com/about> (visited on 07/08/2020).

- [61] *NMP, N-Methylpyrrolidone*. URL: <https://www.fishersci.ca/shop/products/nmp-n-methylpyrrolidone-gc-headspace-grade-fisher-chemical/n1401> (visited on 04/12/2021).
- [62] *Toray Carbon Paper 090, Wet Proofed*. URL: <https://www.fuelcellstore.com/toray-carbon-paper-090> (visited on 06/20/2020).
- [63] Ji Eun Park et al. “High-Performance Anion-Exchange Membrane Water Electrolysis”. In: *Electrochimica Acta* 295 (Feb. 2019), pp. 99–106. ISSN: 00134686.
- [64] Sarawalee Thanasilp and Mali Hunsom. “Effect of MEA Fabrication Techniques on the Cell Performance of Pt–Pd/C Electrocatalyst for Oxygen Reduction in PEM Fuel Cell”. In: *Fuel* 89.12 (Dec. 2010), pp. 3847–3852. ISSN: 00162361.
- [65] Haolin Tang et al. “A Comparative Study of CCM and Hot-Pressed MEAs for PEM Fuel Cells”. In: *Journal of Power Sources* 170.1 (June 2007), pp. 140–144. ISSN: 03787753.
- [66] Fatemeh Razmjooei et al. “Elucidating the Performance Limitations of Alkaline Electrolyte Membrane Electrolysis: Dominance of Anion Concentration in Membrane Electrode Assembly”. In: *ChemElectroChem* 7.19 (Oct. 2020), pp. 3951–3960. ISSN: 2196-0216, 2196-0216.
- [67] Silas Towne et al. “Fabrication of Polymer Electrolyte Membrane Fuel Cell MEAs Utilizing Inkjet Print Technology”. In: *Journal of Power Sources* 171.2 (Sept. 27, 2007), pp. 575–584. ISSN: 0378-7753.
- [68] Madhu S. Saha et al. “Electrochemical Activity and Catalyst Utilization of Low Pt and Thickness Controlled Membrane Electrode Assemblies”. In: *Journal of The Electrochemical Society* 158.5 (Mar. 25, 2011), B562. ISSN: 1945-7111.
- [69] S. Shukla et al. “Analysis of Low Platinum Loading Thin Polymer Electrolyte Fuel Cell Electrodes Prepared by Inkjet Printing”. In: *Electrochimica Acta* 156 (Feb. 2015), pp. 289–300. ISSN: 00134686.
- [70] Carlos André Gomes Bezerra, L. Jay Deiner, and Germano Tremiliosi-Filho. “Unexpected Performance of Inkjet-Printed Membrane Electrode Assemblies for Proton Exchange Membrane Fuel Cells”. In: *Advanced Engineering Materials* 21.11 (Nov. 2019), p. 1900703. ISSN: 1438-1656, 1527-2648.
- [71] S. Shukla et al. “Analysis of Inkjet Printed PEFC Electrodes with Varying Platinum Loading”. In: *Journal of The Electrochemical Society* 163.7 (Apr. 28, 2016), F677. ISSN: 1945-7111.
- [72] S Shukla et al. “Characterization of Inkjet Printed Electrodes with Improved Porosity”. In: *ECS Transactions* (2017), p. 12.
- [73] Dongguo Li et al. “Durability of Anion Exchange Membrane Water Electrolyzers”. In: *Energy & Environmental Science* 14.6 (2021), pp. 3393–3419. ISSN: 1754-5692, 1754-5706.

- [74] Jaromír Hnát et al. “Design of a Zero-Gap Laboratory-Scale Polymer Electrolyte Membrane Alkaline Water Electrolysis Stack”. In: *Chemie Ingenieur Technik* 91.6 (June 2019), pp. 821–832. ISSN: 0009-286X, 1522-2640.
- [75] Brian Derby. “Inkjet Printing of Functional and Structural Materials: Fluid Property Requirements, Feature Stability, and Resolution”. In: *Annual Review of Materials Research* 40.1 (June 2010), pp. 395–414. ISSN: 1531-7331, 1545-4118.
- [76] Gerard Cummins and Marc P.Y. Desmulliez. “Inkjet Printing of Conductive Materials: A Review”. In: *Circuit World* 38.4 (Nov. 16, 2012), pp. 193–213. ISSN: 0305-6120.
- [77] Fujifilm Dimatix Inc. *Jetable Fluid Formulation Guidelines*. May 16, 2013.
- [78] D02 Committee. *Standard Specifications and Operating Instructions for Glass Capillary Kinematic Viscometers*. DOI: 10.1520/D0446-12R17. ASTM International.
- [79] D02 Committee. *Standard Test Method for Kinematic Viscosity of Transparent and Opaque Liquids (and Calculation of Dynamic Viscosity)*. DOI: 10.1520/D0445-19A. ASTM International.
- [80] *Wolfram—Alpha Widgets: “Local Acceleration of Gravity”*. URL: <https://tinyurl.com/75d8rbk6> (visited on 06/08/2021).
- [81] Yunus A. Çengel and Michael A. Boles. *Thermodynamics: An Engineering Approach*. Eighth edition. New York: McGraw-Hill Education, 2015. 996 pp. ISBN: 978-0-07-339817-4.
- [82] *ISO 22412:2017 Particle Size Analysis – Dynamic Light Scattering (DLS)*. URL: <http://www.iso.org/cms/render/live/en/sites/isoorg/contents/data/standard/06/54/65410.html> (visited on 07/25/2019).
- [83] William M. Haynes, ed. *CRC Handbook of Chemistry and Physics*. 97th edition. CRC Press, 2017. 2670 pp. ISBN: 978-1-4987-5429-3.
- [84] Engineering ToolBox. *Methanol - Density and Specific Weight*. 2018. URL: https://www.engineeringtoolbox.com/methanol-density-specific-weight-temperature-pressure-d_2091.html (visited on 04/01/2021).
- [85] Anton Paar. *White Paper: Understanding the Concept of Dynamic Light Scattering :: Anton-Paar.Com*.
- [86] Particulate Systems. *NanoPlus Zeta/Nano Particle Analyzer User’s Manual*.
- [87] Anton Paar. *White Paper: Data Acquisition, Processing and Interpretation in the Litesizer™ Series*.
- [88] Barbara Frisken. *Dynamic Light Scattering - Theory and Practice*.
- [89] Nobbmann Ulf. *How Important Is the Refractive Index of Nanoparticles?* Materials Talks. Aug. 5, 2014. URL: <https://www.materials-talks.com/blog/2014/08/05/faq-how-important-are-refractive-index-absorption-for-nanoparticles/> (visited on 06/10/2021).

- [90] R. M. H. Verbeeck, H. P. Thun, and F. Verbeeck. “Refractive Index of the Propyleneglycol - Water System from 15 to 50 °C”. In: *Bulletin des Sociétés Chimiques Belges* 85.8 (July 26, 1976), pp. 531–534. ISSN: 00379646.
- [91] L.W. Tilton and J. K. Taylor. “Refractive Index and Dispersion of Distilled Water for Visible Radiation, at Temperatures 0 to 60 Degrees C”. In: *Journal of Research of the National Bureau of Standards* 20.4 (Apr. 1938), p. 419. ISSN: 0091-0635.
- [92] Ibrahim S. Khattab et al. “Density, Viscosity, Surface Tension, and Molar Volume of Propylene Glycol + Water Mixtures from 293 to 323 K and Correlations by the Jouyban–Acree Model”. In: *Arabian Journal of Chemistry* 10 (Feb. 2017), S71–S75. ISSN: 18785352.
- [93] Bruno G. Pollet and Jonathan T.E. Goh. “The Importance of Ultrasonic Parameters in the Preparation of Fuel Cell Catalyst Inks”. In: *Electrochimica Acta* 128 (May 2014), pp. 292–303. ISSN: 00134686.
- [94] Michael Adamski et al. “Does Power Ultrasound Affect Hydrocarbon Ionomers?” In: *Ultrasonics Sonochemistry* 75 (July 2021), p. 105588. ISSN: 13504177.
- [95] Young-Chul Park et al. “Effects of Carbon Supports on Pt Distribution, Ionomer Coverage and Cathode Performance for Polymer Electrolyte Fuel Cells”. In: *Journal of Power Sources* 315 (May 2016), pp. 179–191. ISSN: 03787753.
- [96] *Iridium Oxide — IrO₂ — ChemSpider*. URL: <http://www.chemspider.com/Chemical-Structure.10605808.html> (visited on 02/06/2020).
- [97] R. P. Rossman and W. R. Smith. “Density of Carbon Black by Helium Displacement”. In: *Industrial & Engineering Chemistry* 35.9 (Sept. 1943), pp. 972–976. ISSN: 0019-7866, 1541-5724.
- [98] Shantanu Shukla. “Experimental Analysis of Inkjet Printed Polymer Electrolyte Fuel Cell Electrodes”. University of Alberta, 2016.
- [99] Omega Engineering. *ANSI and IEC Color Codes for Thermocouples, Wire and Connectors*.
- [100] *Pamphlet 94: Sodium Hydroxide Solution and Potassium Hydroxide Solution (Caustic) Storage Equipment and Piping Systems*. Edition 5. The Chlorine Institute, Jan. 2018, p. 76.
- [101] Gerhard Kreysa and Michael Schutze. *Corrosion Handbook : Corrosive Agents and Their Interaction with Materials*. 2nd, completely rev. and extended ed. Vol. 9. 13 vols. Wiley-VCH, 2004. ISBN: 978-3-527-31125-5.
- [102] *ISO/TR 15916:2015: Basic Considerations for the Safety of Hydrogen Systems*.
- [103] Rachel Reina Barth, Kevin L. Simmons, and Christopher W. San Marchi. *Polymers for Hydrogen Infrastructure and Vehicle Fuel Systems*. SAND2013-8904, 1104755. Oct. 1, 2013.
- [104] *Abrasion-Resistant Soft Rubber Tubing for Chemicals*. URL: <https://www.mcmaster.com/> (visited on 11/08/2021).

- [105] *Dimatix Materials Printer DMP-2850: Support* — Fujifilm [United States]. URL: <https://www.fujifilm.com/us/en/business/inkjet-solutions/deposition-products/dmp-2850/support> (visited on 05/25/2021).
- [106] Gaoping You, Wei Zhu, and Zhongbin Zhuang. “Impacts of Anions on the Electrochemical Oxygen Reduction Reaction Activity and Stability of Pt/C in Alkaline Electrolyte”. In: *International Journal of Hydrogen Energy* 44.26 (May 2019), pp. 13373–13382. ISSN: 03603199.
- [107] James Richard Kracher. “Experimental Analysis of Transient Water Fluxes in PEM Fuel Cells”. Edmonton, Alberta: University of Alberta, 2018.
- [108] *PTFE Shim Stock*. URL: <https://www.mcmaster.com/shims/shim-stock-6/material-plastic/> (visited on 01/21/2021).
- [109] Kenneth A. Mauritz and Robert B. Moore. “State of Understanding of Nafion”. In: *Chemical Reviews* 104.10 (Oct. 1, 2004), pp. 4535–4586. ISSN: 0009-2665, 1520-6890.
- [110] Naomi Kumano et al. “Controlling Cracking Formation in Fuel Cell Catalyst Layers”. In: *Journal of Power Sources* 419 (Apr. 2019), pp. 219–228. ISSN: 03787753.
- [111] Brian Shanahan et al. “Performance and Stability Comparison of Aemion™ and Aemion+™ Membranes for Vanadium Redox Flow Batteries”. In: *RSC Advances* 11.22 (2021), pp. 13077–13084. ISSN: 2046-2069.
- [112] Rudolf Holze. *Experimental Electrochemistry: A Laboratory Textbook*. 2., completely revised and enlarged edition. Weinheim: Wiley-VCH, 2019. 268 pp. ISBN: 978-3-527-33524-4.
- [113] Hao Xu. “Experimental Measurement of Mass Transport Parameters of Gas Diffusion Layer and Catalyst Layer in PEM Fuel Cell”. University of Alberta.
- [114] Bekaert. *Bekipor Nickel Specifications*.
- [115] Jie Zhou. “Analyzing Multiphase Flow in Membrane Electrode Assembly Using a Mixed Wettability Mathematical Model”. University of Alberta.
- [116] Kock-Yee Law. “Definitions for Hydrophilicity, Hydrophobicity, and Superhydrophobicity: Getting the Basics Right”. In: *The Journal of Physical Chemistry Letters* 5.4 (Feb. 20, 2014), pp. 686–688. ISSN: 1948-7185, 1948-7185.
- [117] *AvCarb MGL280*. URL: <https://www.fuelcellstore.com/fuel-cell-components/gas-diffusion-layers/carbon-paper/avcarb-carbon-paper/avcarb-molded-graphite-laminate/avcarb-mgl280> (visited on 09/17/2021).
- [118] *Fumasep FAA-3-50*. URL: <https://www.fuelcellstore.com/fumasep-faa-3-50> (visited on 06/11/2021).
- [119] Avital Zhegur-Khais et al. “Measuring the True Hydroxide Conductivity of Anion Exchange Membranes”. In: *Journal of Membrane Science* 612 (Oct. 2020), p. 118461. ISSN: 03767388.

- [120] US Fuel Cell Council Materials and Components Working Group. *Fuel Cell Leak Testing Requirements and Procedure*. Nov. 4, 2005.
- [121] Rocco Pagliara. *Type K Thermocouple - GrabCAD*. URL: <https://grabcad.com/library/type-k-thermocouple> (visited on 02/16/2020).
- [122] J Bravo. *Square Bottle - GrabCAD*. URL: <https://grabcad.com/library/200ml-100ml-square-bottle-1> (visited on 02/16/2020).
- [123] Anthony J. Wheeler. *Introduction to Engineering Experimentation*. 3rd ed. Upper Saddle River, N.J. : Pearson Higher Education, c2010. ISBN: 978-0-13-174276-5.
- [124] John R. Taylor. *Introduction To Error Analysis: The Study of Uncertainties in Physical Measurements*. University Science Books, July 14, 1997. 356 pp. ISBN: 978-0-935702-75-0.
- [125] Steven C. Chapra. *Applied Numerical Methods with MATLAB for Engineers and Scientists*. 3rd ed. New York: McGraw-Hill, 2012. 653 pp. ISBN: 978-0-07-340110-2.

Appendix A

Equipment Information

A.1 Temperature Control Box Design

Temperature control boxes equipped with PIDs were assembled to control the temperature of the water bath used during viscosity experiments, as well as the electrolyzer cell and liquid within the gas disengagement units (GDUs) for the AEM-based electrolyzer test-station. The electrolyzer cell and GDUs were each controlled by their own temperature control box. A bill of materials for a single temperature control box is provided in Table A.1 while a general schematic of the box’s internal configuration is provided in Figure A.1. The PID controller was used as-received without altering the controllers operational parameters.

Table A.1 – Bill of materials for temperature control boxes used for AEM electrolyzer test-station.

Description	QTY. ^a	Supplier	Part No. ^b
5.99”x4.99” Black Aluminum Box	1	Digikey	HM2554-ND
10A Circuit Breaker Power Receptacle	1	Digikey	486-2254-ND
10A Snap-in Panel Mount Power Receptacle	1	Digikey	Q338-ND
Temperature PID	1	Omega	CN7823
Solid-State Relay 10A	1	Omega	SSRL240DC10
Thermocouple Female Connector	1	Omega	MPJ-T-F

^a Quantity required to assemble *one* temperature control box

^b Part number given by supplier



2139 High Tech Road
 State College, PA 16803
 814-353-8000 • 800-676-6232 • Fax 814-353-8007
 cannon@canoninstrument.com
 www.canoninstrument.com

Certificate of Calibration

ZEITFUCHS CROSS-ARM VISCOMETER		
Size	Serial Number	B562
Constant mm ² /s, (cSt/s)	Expanded Uncertainty* (n=2) %	Kinematic Viscosity Range mm ² /s, (cSt)
0.009463	0.16	2 - 10

* In alignment with the Calibration and Measurement Capabilities of National Metrology Institutes, the expressed uncertainty is relative to the viscosity of water, and therefore the uncertainty of the viscosity of water (ISO/TR 3666 (1998), 0.17%) is not taken into account.

CALIBRATION DATA AT 40°C - The viscometer constant is the same at all temperatures.

Viscosity Standard	Kinematic Viscosity mm ² /s, (cSt)	Efflux Time		Constant mm ² /s, (cSt/s)
		Seconds	Seconds	
I2	2.418	255.54	404.56	0.009460
I3	3.829	404.56		0.009465

Average = 0.009463

Kinematic viscosities of the standards used in calibrating were established in Master Viscometers as described in Ind. Eng. Chem. Anal. Ed., 16:708(1944), ASTM D 2162, and the Journal of Research of the National Bureau of Standards, Vol. 52, No. 3, March 1954, Research Paper 2479.

Kinematic viscosities are traceable to the viscosity of water ISO 3666, at 20°C (ITS-90). Temperature measurements are traceable to NIST fixed-point calibration of SPRTs.
 The gravitational constant, g, is 980.1 cm/sec² at the Cannon Instrument Company. The gravitational constant varies up to 0.1% in the United States. To make this small correction in the viscometer constant, multiply the above viscometer constant by the factor Ig (at your laboratory) / 980.1).

Calibrated by DLH on 3/15/2021
 Issue Date 3/15/2021

under supervision of
 D. T. Trowbridge Ph.D
 J. T. Mastropiero
 M. T. Zubler
 Laboratory Technical Director
 Deputy Laboratory Technical Director
 Director of Quality Assurance

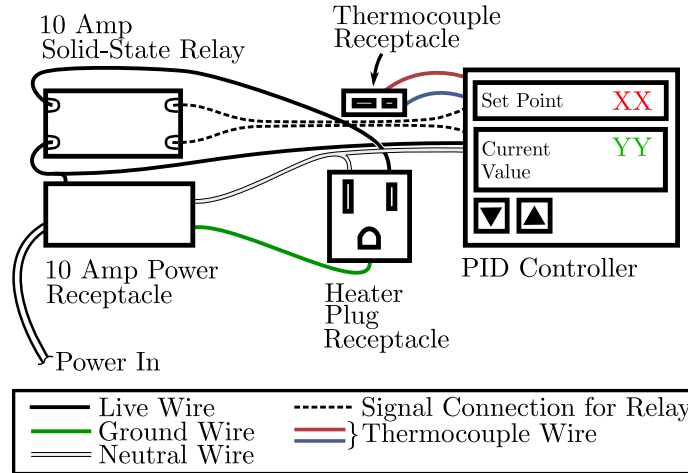


Figure A.1 – General schematic of PID temperature control box. Based upon the temperature obtained from the thermocouple, the PID triggers the heater on or off via the solid-state relay.

A.2 Zeitfuchs Cross-Arm Calibration Documentation

A.3 Gas Disengagement Unit Design

As discussed in Section 3.1.1, the anode and cathode GDUs used for the AEM-based electrolyzer test-station function as two-phase gas-liquid separation units. Additionally, the units store and heat the liquid fed to the electrolyzer cell (deionized water or aqueous KOH). The stored liquid is isolated from the ambient atmosphere such that CO_2 does not enter the system. A schematic of the in-house designed GDU is provided in Figure A.2 with a corresponding bill of materials provided in Table A.2. As seen in the bill of materials, the materials selected are limited to high density polyethylene (HDPE), 316 stainless steel (316 SS), polytetrafluoroethylene (PTFE), and nitrile (Buna-N). These materials were selected as they have been reported to be resistant against both aqueous KOH [101] and hydrogen gas [102, 103]. Following the assembly of the units, they were verified to be pressure tight up to 5 psig (well beyond the 1/3 psig cracking pressure of the check valves used) by filling the units with nitrogen gas, immersing them in a bath of water, and ensuring no gas bubbles appeared in the water.

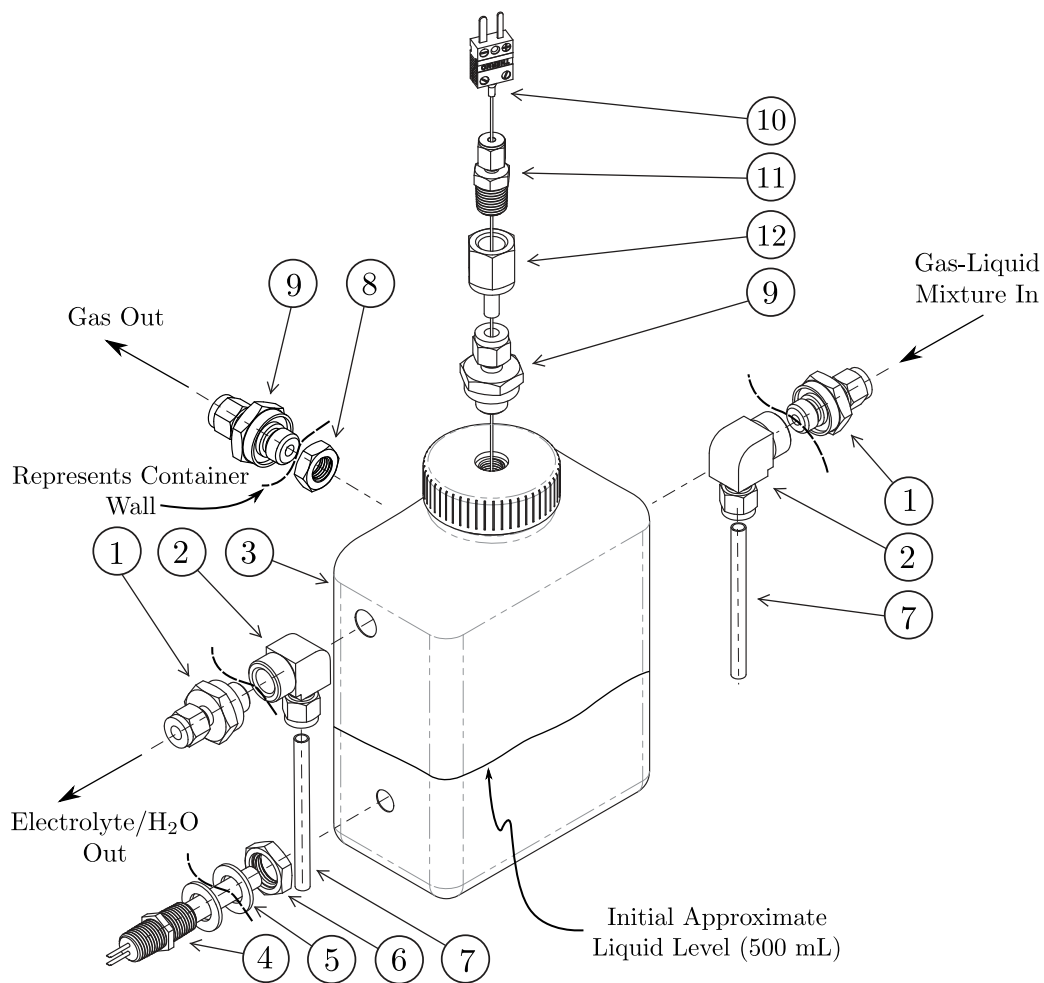


Figure A.2 – Isometric exploded view of GDU design used for AEM electrolyzer test station. Component numbers correspond to bill of materials in Table A.2. All solidmodel components obtained from McMaster-Carr with the exception of the thermocouple and HDPE plastic jar obtained from Refs. [121, 122], respectively.

Table A.2 – Bill of materials for GDU corresponding to Figure A.2.

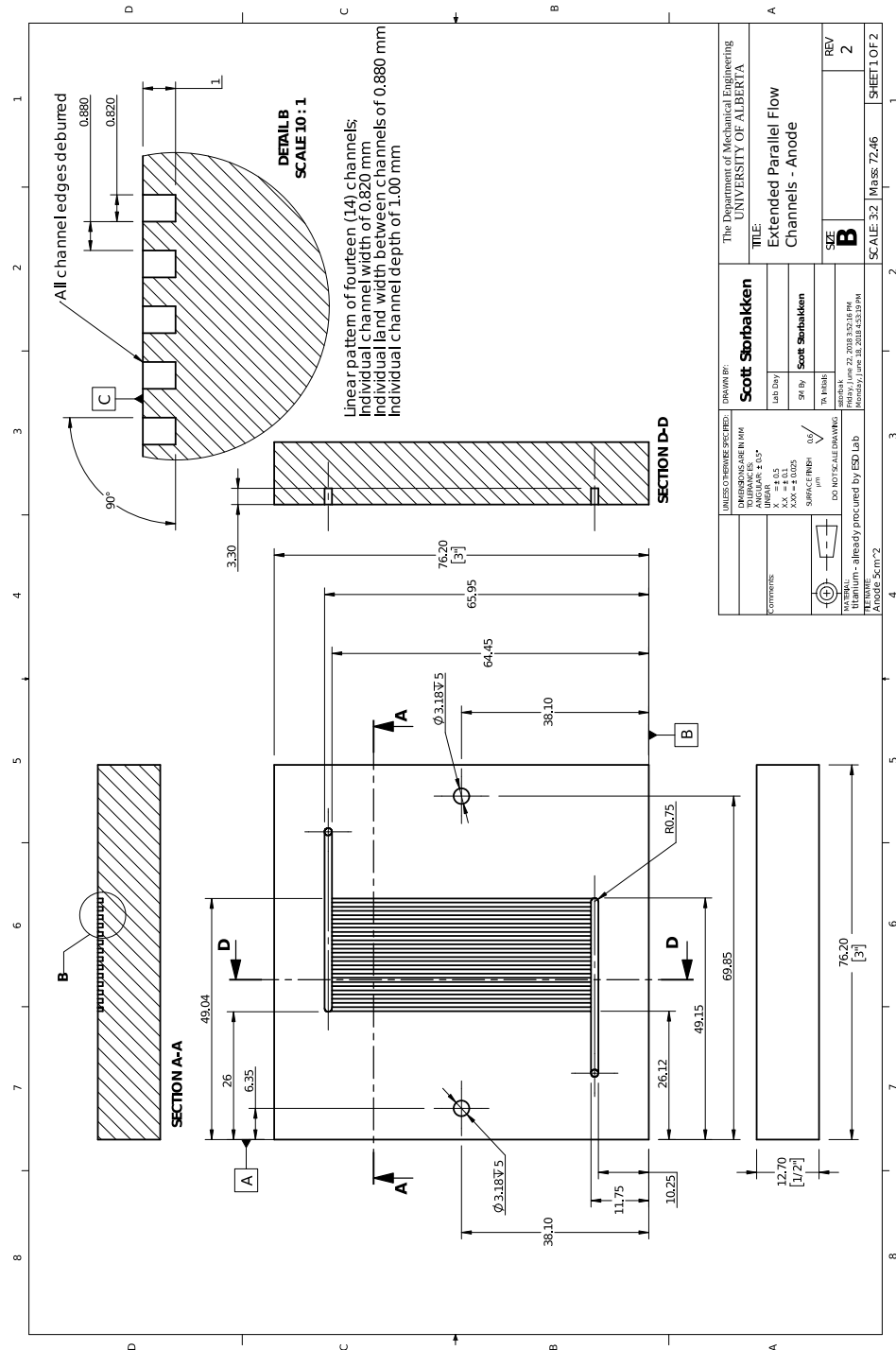
Item	Description	QTY. ^a	Supplier	Part No. ^b
1	Female 1/4" Tube OD to Male 1/4" NPT w/ Buna-N O-Ring Seal	2	Swagelok	SS-400-1-4-OR
2	Female 1/4" NPT to Female 1/4" OD Tube Elbow	2	Swagelok	SS-400-8-4
3	HDPE Plastic Jar, 950 mL Capacity (5" wd. 2-7/8" dp. 7-1/8" ht.)	1	McMaster-Carr	4293T79
4	316 SS 75W 120V Heating Element (1-9/16" lg. with 1/4" NPT)	1	McMaster-Carr	4668T53
5	PTFE 1/4" Sealing Washer	2	McMaster-Carr	95630A475
6	316 SS Threaded Pipe Locknut (1/4" NPSL)	1	McMaster-Carr	4452K672
7	PTFE 1/4" Tubing	2	McMaster-Carr	5033K31
8	316 SS Thin Hex Nut (7/16"-20 Thread Size)	2	McMaster-Carr	94805A221
9	Female 1/4" Tube OD to Male 7/16"-20 Thread Size w/ Buna-N O-Ring	2	Swagelok	SS-400-1-ORBT
10	316 SS Type T Thermocouple (1/8", 12" lg.)	1	Omega	TMT 316 SS-125U-12
11	316 SS Thermocouple Compression Fitting w/ PTFE Ferrule (1/4" NPT)	1	Omega	SSLK-18-14
12	Female 1/4" NPT to Male 1/4" OD Tube Adapter	1	Swagelok	SS-4-TA-7-4

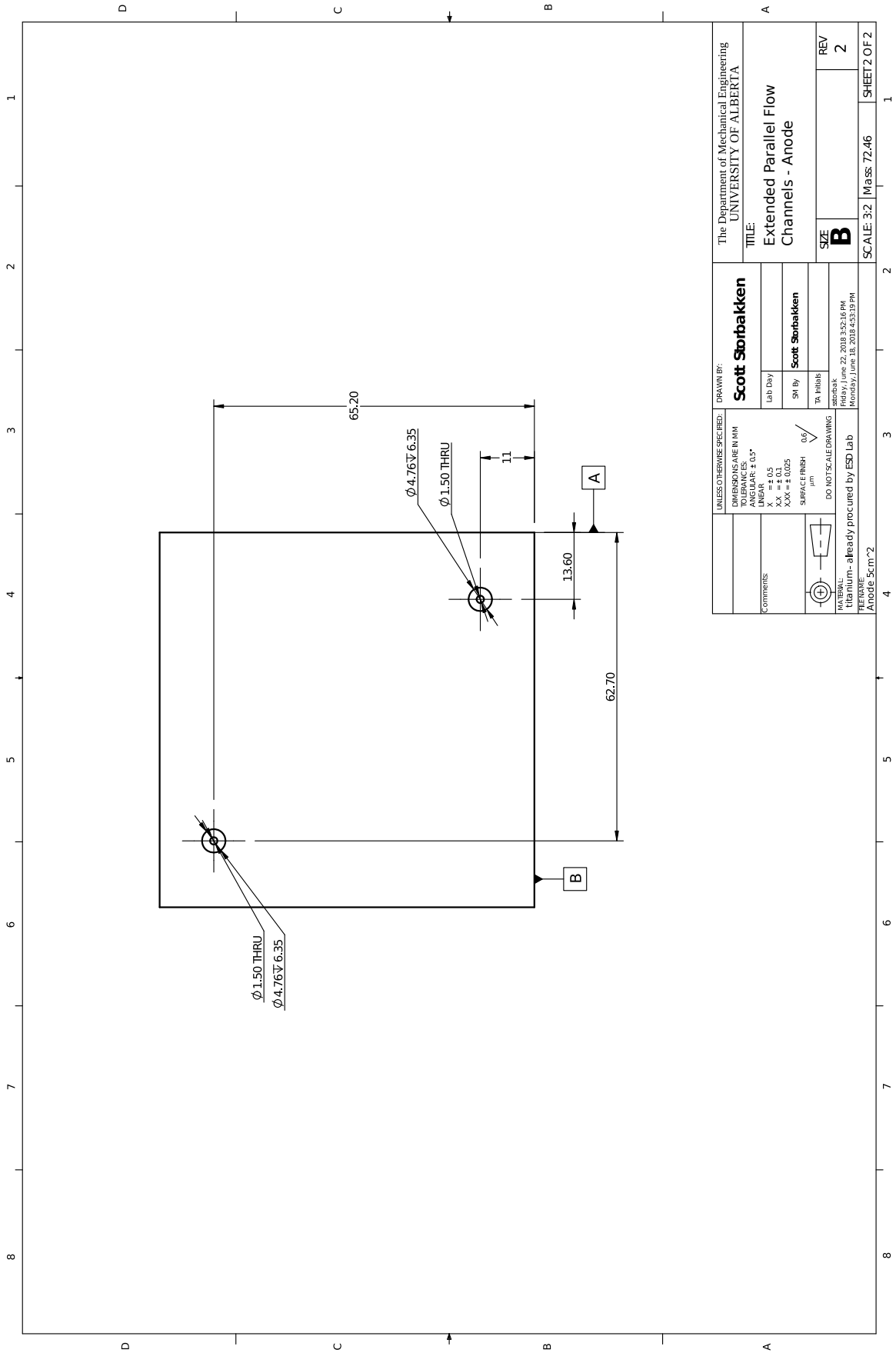
^a Quantity required to assemble *one* GDU

^b Part number given by supplier

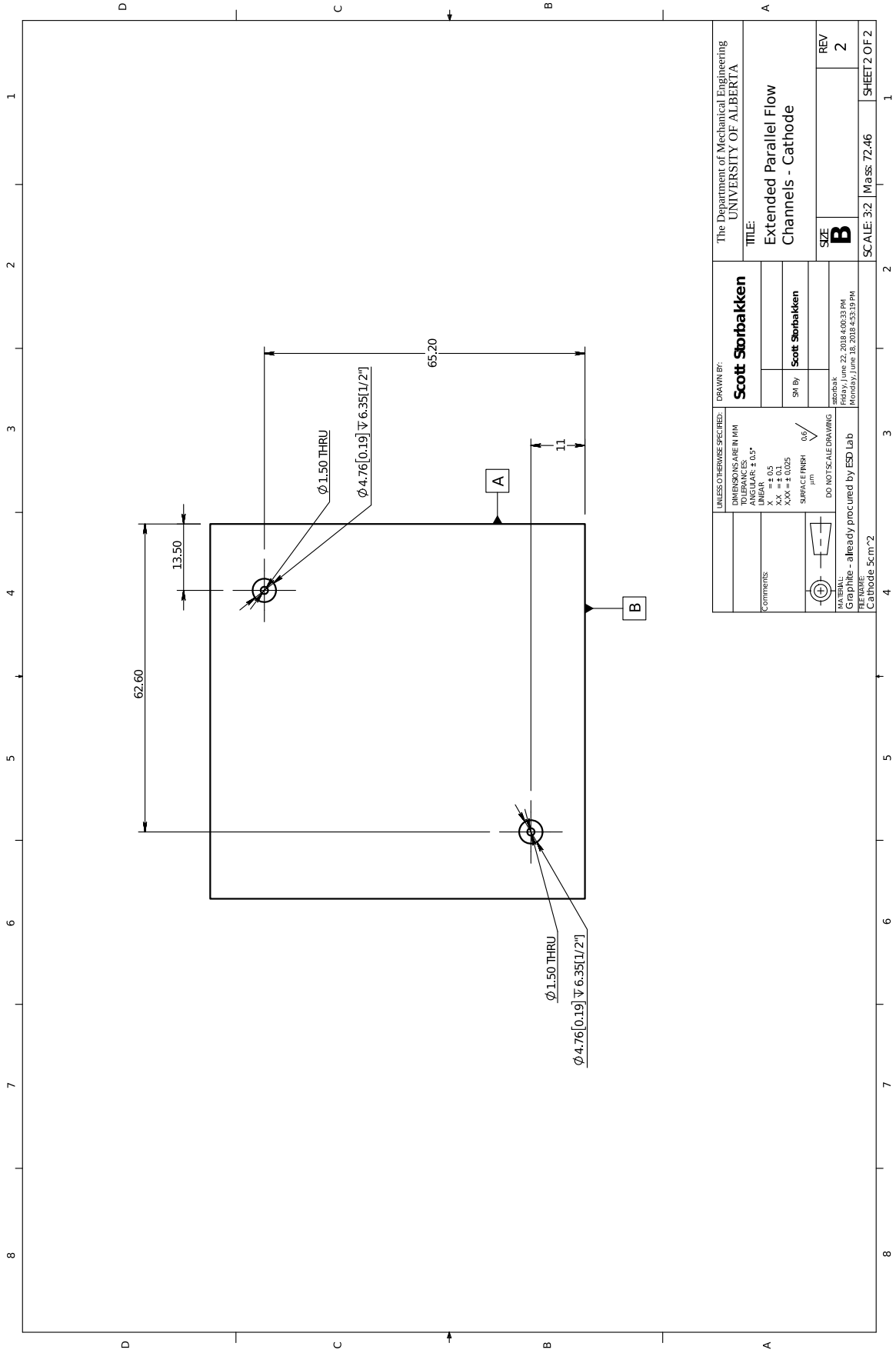
A.4 Extended Parallel Channel Flow Field Bipolar Plate Drawings

Contained herein are the drawings used to produce the anode and cathode extended parallel flow channel bipolar plates. The anode was manufactured from titanium while the cathode was manufactured from graphite.





UNLESS OTHERWISE SPECIFIED:		DRAWN BY:		The Department of Mechanical Engineering UNIVERSITY OF ALBERTA	
DIMENSIONS ARE IN MM		Scott Storbakken		TITLE:	
ANGULARS ± 0.5°		Lab Day		Extended Parallel Flow Channels - Anode	
LINEAR ± 0.5		SN by	Scott Storbakken	SIZE	REV
XX ± 0.1		TR IN/OUT		B	2
XXX ± 0.025		SURFACE FINISH		SCALE: 3:2 Mass: 72.46	
0.6/		DO NOT SCALE DRAWING		SHEET 2 OF 2	
MATERIAL: titanium- alloyed procured by ESD Lab		DATE: 23, 2018 3:53:16 PM			
REFERENCE: Anode 5cm²		DATE: Monday, June 18, 2018 4:53:19 PM			



UNLESS OTHERWISE SPECIFIED:		DRAWN BY:	
DIMENSIONS ARE IN MM		Scott Storbakken	
ANGULARS ± 0.5°			
LINEAR			
XX = ± 0.1			
XXX = ± 0.025			
SURFACE FINISH		SM by Scott Storbakken	
μm			
0.6/√			
DO NOT SCALE DRAWING			
MATERIAL:		DATE: June 23, 2018 4:00:33 PM	
Graphite - already procured by ESD Lab		Monday, June 18, 2018 4:53:19 PM	
REFERENCE:			
Cathode 5cm ²			
SCALE: 3:2	Mass: 72.46	SIZE B	REV 2
		SHEET 2 OF 2	

Appendix B

Uncertainty Analysis

Measurement uncertainties may be broadly categorized into two forms; namely, bias uncertainty associated with the measurement system and precision uncertainty associated with the randomness of multiple measurements. If an arbitrary variable (x) is subject to both bias (Δx_{bias}) and precision ($\Delta x_{\text{precision}}$) uncertainties, then the total uncertainty (Δx_{total}) may be resolved by taking the L2 norm of the precision and bias uncertainties as follows,

$$\Delta x_{\text{total}} = \sqrt{\Delta x_{\text{precision}}^2 + \Delta x_{\text{bias}}^2}. \quad (\text{B.1})$$

Furthermore, uncertainties of both kinds propagate through calculations made with raw data and must be accounted for. For a value (X) calculated from a general function of the form $f(x_i) = X$, the propagation of uncertainty may be resolved by employing the following [123],

$$\Delta X = \sqrt{\sum_i \left(\frac{\partial f}{\partial x_i} \Delta x_i \right)^2}, \quad (\text{B.2})$$

where:

x_i are the dependent variables of X ,

Δx_i is the uncertainty associated with the i^{th} dependent variable, and

∂ is partial differentiation.

If $f(x_i)$ is strictly a multiplicative expression, then Eq. (B.2) simplifies to

$$\Delta X = X \sqrt{\sum_i \left(\lambda_i \frac{\Delta x_i}{x_i} \right)^2}, \quad (\text{B.3})$$

where λ is the exponent of variable x_i within $f(x_i)$.

B.1 Viscometer Calibration

In the case of calculating the constant for the Cannon-Fenske routine style glass capillary viscometer the following multiplicative equation was used,

$$C_{\text{CF}} = \frac{C_{\text{ZC}} t_{\text{ZC}}}{t_{\text{CF}}}, \quad (\text{B.4})$$

where:

C_{CF} is the calculated viscometer constant for the Cannon-Fenske viscometer, mm^2/s^2 ,

C_{ZC} is the known constant of the Zeitfuchs Cross-Arm viscometer, mm^2/s^2 ,

t_{CF} is the average flow time of EG for the Cannon-Fenske viscometer, s, and

t_{ZC} is the average flow time of EG for the Zeitfuchs Cross-Arm viscometer, s.

Applying Eq. (B.3) to Eq. (B.4) yields the following,

$$\Delta C_{\text{CF}} = C \sqrt{\left(\frac{\Delta C_{\text{ZC}}}{C_{\text{ZC}}}\right)^2 + \left(\frac{\Delta t_{\text{ZC}}}{t_{\text{ZC}}}\right)^2 + \left(\frac{\Delta t_{\text{CF}}}{t_{\text{CF}}}\right)^2}. \quad (\text{B.5})$$

The relative uncertainty of the constant for the Zeitfuchs Cross-Arm viscometer is taken as 0.16% as per the calibration documentation provided in Appendix A.2. For the time measurements, a repeatability test was completed using ethylene glycol (EG) and the Cannon-Fenske viscometer at 30 °C—the precision uncertainty associated with these measurements may be determined using the following general equation,

$$\Delta \bar{X} = \pm \tilde{t} \frac{S_X}{\sqrt{n}}, \quad (\text{B.6})$$

where:

\bar{X} is the average of the measured values (830.298 s),

\tilde{t} is the students t -value,

S_X is the standard deviation of the measurements, and

n is the number of measurements conducted.

For the experiments conducted with EG, the sample standard deviation was found to be 1.584 s and the t -value for a 95%¹ confidence interval is 2.571 (5 degree of freedom), and as such,

$$\Delta \bar{t} = 2.571 \frac{1.584}{\sqrt{6}} = \pm 1.663 \text{ s.}$$

¹As per Wheeler and Ganji, a 95% confidence interval is commonly used for uncertainty analysis [123]

Note that the bias uncertainty associated with the stopwatch used to obtain the times was half a hundredths of a second, and as such, is neglected as it is much smaller than the precision uncertainty. It is assumed that the precision uncertainty in time measurements using the Zeitfuchs Cross-Arm viscometer is the same as that obtained for the Cannon-Fenske viscometer.

Using the obtained value for C_{CF} of $0.01452 \text{ mm}^2/\text{s}^2$ using EG (refer to Section 2.1.1), as well as the uncertainty values for time and the Zeitfuchs Cross-Arm viscometer constant, Eq. (B.5) is used to determine the uncertainty in $C_{CF,EG}$,

$$\Delta C_{CF,EG} = (0.01452 \text{ mm}^2/\text{s}^2) \sqrt{(0.0016)^2 + 2 \left(\frac{1.663}{830.298} \right)^2} = 4.7 (10^{-5}) \text{ mm}^2/\text{s}^2,$$

where the subscript EG has been used to indicate that the resolved uncertainty is specific to the calibration constant obtained using EG. Following the same calculation, the calibration constant obtained using silicone oil was found to be $0.01468 \pm 4.8 (10^{-5}) \text{ mm}^2/\text{s}^2$. The final calibration constant for the Cannon-Fenske viscometer was taken as the average between the values obtained using EG and silicone oil. As such, the final uncertainty in the calibration constant is determined as follows,

$$\Delta C_{CF} = \sqrt{\frac{1}{4} (\Delta C_{CF,EG}^2 + \Delta C_{CF,SO}^2)}. \quad (\text{B.7})$$

Note that Eq. (B.7) was derived by applying Eq. (B.2) to the equation for the average of two values and the subscript SO denotes silicone oil. Finally,

$$\Delta C_{CF} = \sqrt{\frac{1}{4} \left[(4.7 (10^{-5}) \text{ mm}^2/\text{s}^2)^2 + (4.8 (10^{-5}) \text{ mm}^2/\text{s}^2)^2 \right]} = 3.4 (10^{-5}) \text{ mm}^2/\text{s}^2.$$

The reported value for the Cannon-Fenske calibration constant is therefore $0.01460 \pm 3.4 (10^{-5}) \text{ mm}^2/\text{s}^2$.

B.2 Solvent and Catalyst Ink Density

The density of a fluid is the mass per unit volume at a given temperature. The density may be determined experimentally by measuring the mass (m) of a known volume (V) of fluid and dividing the two values as follows,

$$\rho = \frac{m}{V}. \quad (\text{B.8})$$

In an effort to minimize the uncertainty associated with determining the density, the mass was recorded as the volume of the fluid was increased from 2–10 mL in 1 mL

increments (9 measurements total). Performing a linear regression on the obtained volume and mass data yields the density as the slope (mass along the y -axis and volume along the x -axis).

As per Taylor, the measurement of each mass may be assumed to be normally distributed about its true value described by the line of $A + \rho V_i$ where A is the zero-intercept, ρ is the fluids density, and V_i is the volume of the i^{th} measurement [124]. Thus, the deviations of $m_i - A - \rho V_i$ are normally distributed, and if the intercept and density are replaced by best estimates obtained from performing a linear regression, then Taylor states that the uncertainty in the y -axis values, or mass in this case, is as follows,

$$\Delta m = \sqrt{\frac{1}{N-2} \sum_i^N (m_i - A - \rho V_i)^2}, \quad (\text{B.9})$$

where N is the total number of measurements conducted. Note that the uncertainty in the mass found from Eq. (B.9) is effectively precision based, but may be compared to the measurement device's bias uncertainty. The raw data obtained for measuring the density of water, along with the bracketed calculation described in Eq. (B.9), is provided in Table B.1. The linear regression for the data was performed using Microsoft Excel to yield a density of 1.001 g/mL and an intercept of -0.1735 g. Using the information provided in Table B.1, it is possible to calculate the uncertainty in mass as per Eq. (B.9),

$$\Delta m_{\text{water}} = \sqrt{\frac{1}{9-2} (9.64693) (10^{-4})} = \pm 0.0117394 \text{ g} = \pm 11.7 \text{ mg}.$$

This value is relatively high given that the resolution of the weigh scale used to

Table B.1 – Data obtained for measuring the density of water at room temperature.

V (mL)	m (g)	V^2 (mL ²)	$(m_i - A - \rho V_i)^2$
2	1.8388	4	0.000113
3	2.8357	9	4.49E-05
4	3.8273	16	6.42E-06
5	4.8039	25	0.000716
6	5.8364	36	2.4E-05
7	6.8321	49	5.44E-08
8	7.8308	64	5.6E-06
9	8.8369	81	8.41E-06
10	9.8416	100	4.58E-05
54		384	0.000965

conduct the measurement was 0.1 mg. Nonetheless, as per Taylor, this uncertainty may be further used with the following equations to determine the uncertainty in the resolved intercept and best fit slope², respectively,

$$\Delta A = \Delta m \sqrt{\frac{\sum V_i^2}{N \sum V_i^2 - (\sum V_i)^2}}, \quad (\text{B.10})$$

$$\Delta \rho = \Delta m \sqrt{\frac{N}{N \sum V_i^2 - (\sum V_i)^2}}. \quad (\text{B.11})$$

However, since the volume measurements have an uncertainty of 0.1 mL associated with them, an equivalent uncertainty in the mass, defined as per Eq. (B.12) needs to be used in Eqs. (B.10) and (B.11) in place of Δm [124].

$$\Delta m_{\text{equiv.}} = \sqrt{(\Delta m)^2 + (\rho \Delta V)^2} \quad (\text{B.12})$$

Substituting values obtained for water into Eq. (B.12) yields the following,

$$\Delta m_{\text{equiv.}} = \sqrt{(0.0117394)^2 + ((1.001) 0.1)^2} = \pm 0.10078 \text{ g},$$

Note that this equivalent uncertainty in mass is nonphysical, but is used to account for the uncertainties in both the mass and volume measurements. Finally, utilizing the calculated equivalent mass uncertainty, along with the values in Table B.1, Eqs. (B.10) and (B.11) yield the following,

$$\Delta A_{\text{water}} = 0.10078 \sqrt{\frac{384}{9(384) - 54^2}} = 0.08499 \text{ g} = \pm 85.0 \text{ mg},$$

$$\Delta \rho_{\text{water}} = 0.10078 \sqrt{\frac{9}{9(384) - 54^2}} = \pm 0.0130 \text{ g/mL}.$$

Thus, the density of water was found to be 1.001 ± 0.013 g/mL with a zero-intercept of -0.17 ± 0.08 g. For analysis purposes, the intercept was not forced through zero, and instead it may be concluded that there is an error with the presented data and/or experiment since zero is not within the bounds of the intercept and its uncertainty (of course the mass should be zero when there is no water). Note that if the zero-intercept is forced through zero and a similar uncertainty analysis is conducted that a density of 0.970 ± 0.006 g/mL is obtained.

For density tests conducted for catalyst inks using only 5 mL, the process of measuring the mass for volumes of 1–5 mL in 1 mL increments was the same as for

²Eqs. (B.10) and (B.11) are derived using the principals of uncertainty propagation and the equations used for performing a linear regression.

when 10 mL was used, but the entire experiment was repeated four times. As such, the uncertainty in each of the individual density values was obtained using the same process provided above and the uncertainty in final averaged density was found using the following formula (derived using Eq. (B.2)),

$$\Delta\rho = \frac{1}{4} \sqrt{\sum_i^4 \rho_i^2} \quad (\text{B.13})$$

where ρ_i is the density obtained from each experimental iteration.

B.3 Litesizer 500 Bias Uncertainty Validation

To validate the uncertainty of the Anton Paar Litesizer 500 by Anton Paar for particle size analyses, a solution of particles with a known diameter was tested and analyzed. As per ISO Standard 22412, the bias uncertainty of the Litesizer may be determined by measuring the particle diameter of a certified suspension of polystyrene latex. ISO 22412 states the following [82],

To assess potential bias, the uncertainty for the mean value of the CRM [certified reference material] should be combined with a tolerance for the measurement uncertainty and expanded with a factor of 2 to obtain an expanded uncertainty. The absolute difference between the certified value and the average of 5 results shall be smaller than this combined uncertainty.

Data for the CRM used for testing the bias uncertainty of the Litesizer is provided in Table B.2 while experimental results obtained from the Litesizer for the CRM are provided in Table B.3. Following the example provided in ISO 22412:

1. Convert the expanded uncertainty of the CRM to a standard uncertainty by dividing by the specified k -factor:

$$\Delta_{\text{CRM}} = 3 \text{ nm}/2 = 1.5\text{nm}$$

Table B.2 – Physical data for CRM used to test bias uncertainty of Anton Paar Litesizer 500.

Material Composition:	Polystyrene
Certified Mean Diameter:	215 nm
Expanded Uncertainty:	$\pm 3 \text{ nm}$, $k = 2$

Table B.3 – Experimental DLS results for CRM obtained from Anton Paar Litesizer 500.

Number of Measurements:	5
Measured Diameter:	218.34 ± 1.96 nm
Polydispersity Index:	$2.19\% \pm 2.35$
Fit Error ^a :	$1.17\text{E-}05 \pm 2.77\text{E-}06$
Average Intensity Trace ^b :	300 ± 5

^a Average fit error for the measurements between $G^{(2)}(\tau)$ and the least squares fit used to determine $\bar{\Gamma}$ and μ_2 (refer to Section 2.1.3). Note that this process is completed by the Kalliope software

^b Each measurement yields an average intensity trace; this is an *average of those averages*

2. Calculate the tolerance for the measurement uncertainty for the measured average. ISO 22412 states that the tolerance for the measurement uncertainty is 1.5% for particles ‘about’ 100 nm in diameter. Proceeding with this tolerance, even though the particles are larger than 100 nm:

$$\Delta_{\text{measurement}} = 218 \text{ nm} \cdot 0.015 = 3.27 \text{ nm}$$

3. Take the Euclidean norm of the results from the steps above and expand by the k -factor of 2 to obtain the expanded uncertainty:

$$\Delta_{\text{expanded}} = k\sqrt{\Delta_{\text{CRM}}^2 + \Delta_{\text{measurement}}^2} = 2\sqrt{1.5^2 + 3.27^2} = 7.19 \text{ nm}$$

4. The absolute difference between the measured average diameter and the certified diameter is,

$$218.34 \text{ nm} - 215 \text{ nm} = 3.34 \text{ nm}.$$

Since this difference is less than Δ_{expanded} , the Litesizer fulfills the test for bias.

5. Further, ISO 22412 states that “for suspensions of particles of about 100 nm in diameter... the standard deviation of 5 repeats shall be better than 2%; the PI shall be smaller than 0.1 [10%].” From the data presented in Table B.3, it is clear that even though the particle size is larger, these requirements are fulfilled (maximum PI for all measurements was 7.34% and the standard deviation of the diameter was 0.9%). Thus, for a suspension of particles that is ideal for DLS, the Litesizer is capable of producing sufficient (arguably excellent) results.

B.4 Solvent and Catalyst Ink Viscosity

For the current work, the kinematic viscosity (ν , mm²/s) of catalyst inks and their solvent solutions were obtained using glass capillary kinematic viscometers using the following,

$$\nu = Ct, \quad (\text{B.14})$$

where C is the calibration constant of the viscometer (mm²/s²) and t is the average flow time (s) obtained experimentally for the test sample. However, to perform dynamic light scattering (DLS) experiments, the dynamic viscosity is required. The kinematic viscosity may be converted to the dynamic viscosity (η) using the samples density (ρ) with the following relationship,

$$\eta = \rho\nu, \quad (\text{B.15})$$

where ρ and η have units of g/cm³ and mPa.s, respectively. Combining Eqs. (B.14) and (B.15),

$$\eta = \rho Ct. \quad (\text{B.16})$$

The uncertainty of Eq. (B.16) may be found by applying Eq. (B.3) as it is a multiplicative equation,

$$\Delta\eta = \eta \sqrt{\left(\frac{\Delta\rho}{\rho}\right)^2 + \left(\frac{\Delta C}{C}\right)^2 + \left(\frac{\Delta t}{t}\right)^2}. \quad (\text{B.17})$$

To calculate the uncertainty in the dynamic viscosity the uncertainty in density ($\Delta\rho$) is obtained from Appendix B.2, the uncertainty in the viscometer constant (ΔC) is provided in Appendix B.1 for the Cannon-Fenske Routine viscometer and Appendix A.2 for the Zeitfuchs Cross-arm viscometer, and lastly, the uncertainty in the time ($\Delta t/t$) has been taken as 0.2% as discussed in Appendix B.1.

B.5 Test-Station Pump Flow Rate

To determine an expression for the test-station's pump flow rate as a function of pump head speed, the time required to fill a 100 mL volumetric flask (#5580, Pyrex) was recorded at various pump speeds. The resulting pump flow rate expression, $\dot{V}(N_\omega)$, was then determined from the line of best fit from the corresponding linear curve between the resolved flow rates and pump speeds (N_ω). The individual flow times ($t_{\omega,i}$) were converted to flow rates using the following relationship,

$$\dot{V}_i = \frac{100 \text{ mL}}{t_{\omega,i}},$$

where $t_{\omega,i}$ was measured in seconds and converted to minutes. The resulting flow rate data obtained from testing various pump head speeds is provided in Figure B.1. From the plot of flow rates vs. pump head speeds the pump flow rate expression was determined using a linear regression to be the following,

$$\dot{V} = 0.175N_{\omega} + 0.003 \text{ mL/min} \quad (\text{B.18})$$

Note that the zero-intercept of Eq. (B.18) was not forced to be zero since an uncertainty analysis of the intercept can be used as partial validation for the data since zero should be within the uncertainty range (at a pump speed of zero the flow rate must also be zero).

The uncertainty for the line of best fit in Figure B.1 was analyzed in the same manner as the line of best fit for the density data in Appendix B.2. That is, each volumetric flow rate (\dot{V}_i) was assumed to be normally distributed about its true value described by $A + BN_{\omega,i}$ where A and B are the zero intercept and slope, respectively, estimated from the aforementioned linear regression. The uncertainty in \dot{V} is then taken as [124],

$$\Delta\dot{V} = \sqrt{\frac{1}{N-2} \sum_i^N (V_i - A - BN_{\omega,i})^2}, \quad (\text{B.19})$$

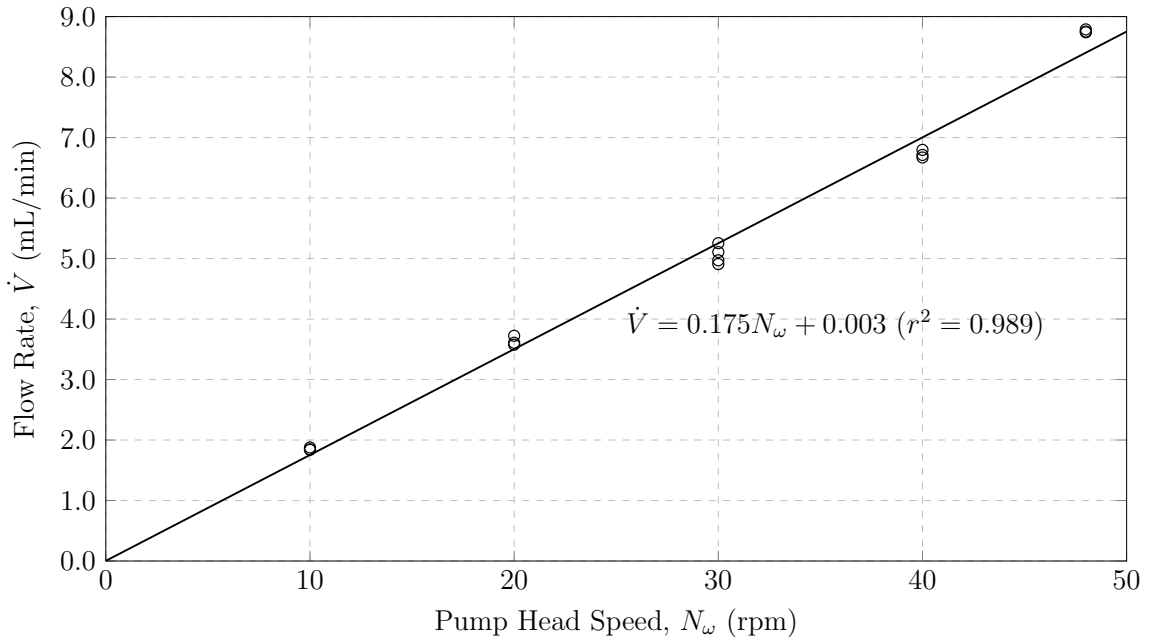


Figure B.1 – Experimentally determined relationship between peristaltic pump head speed and resulting flow rate for AEM-based electrolyzer test-station. Results obtained for a single pump stream.

where N is the total number of measurements conducted—16 in this case. Using the data in Figure B.1, Eq. (B.19) yields $\Delta\dot{V} = \pm 0.2587$ mL/min. The uncertainty in the resolved best fit intercept and slope are then respectively given as [124],

$$\Delta A = \Delta\dot{V} \sqrt{\frac{\sum N_{\omega,i}^2}{N \sum N_{\omega,i}^2 - (\sum N_{\omega,i})^2}} = \pm 0.159 \text{ mL/min},$$

$$\Delta B = \Delta\dot{V} \sqrt{\frac{N}{N \sum N_{\omega,i}^2 - (\sum N_{\omega,i})^2}} = \pm 0.005 \text{ mL/min/rpm}.$$

An equivalent uncertainty in \dot{V} , as was done for the density data in Appendix B.2, was not used for this work since the uncertainty in the pump speed was considered negligible since it is selected as an integer value. As expected, zero is within the uncertainty domain of the resolved intercept ($-0.156 < A < 0.162$). As such, the intercept is dropped from Eq. (B.18) and the final flow rate relationship is given as,

$$\dot{V} = 0.175 N_{\omega} \pm 0.3 \text{ mL/min}.$$

Appendix C

Linear System of Equations for Calculating Catalyst Ink Recipes

To convert general catalyst ink recipes based upon relative wt.-%s to specific gravimetric based recipes, a system of linear systems was developed. A summary of the input and output parameters for the developed system of linear equations is provided in Table C.1. With the exception of wt_{inmr} , each of the wt.-% ratios provided in Table C.1 may be used to write an equation linking the wt.-% ratios to the absolute mass values required to make the ink. The first of said ratios, $wt_{inkInmr}$, may be used

Table C.1 – Description of variables for a system of linear equations for converting generalized catalyst ink recipes based upon relative wt.-%s to absolute gravimetric-based recipes.

Variable	Classification ^a	Description
wt_{inmr}	Input	wt.-% of ionomer polymer in solution ^b
$wt_{inkInmr}$	Input	wt.-% of ionomer (solid-phase) to all solid-phase constituents
$wt_{alch:water}$	Input	wt.-% of alcohol to water within ink
wt_{PG}	Input	wt.-% of PG to all liquid-phase constituents
wt_{inkStd}	Input	wt.-% of all solid-phase constituents to the total ink mass
V_{ink}	Input	total volume of resulting ink
m_{inmr}	Output	mass of ionomer solution required
m_{ctlst}	Output	mass of catalyst required
m_{water}	Output	mass of water required
m_{alch}	Output	mass of alcohol required
m_{PG}	Output	mass of PG required

^a Variables may either be an input that generally classify the ink, or an output that is used to specifically create the ink using a mass balance

^b This is the wt.-% of ionomer content within the ionomer solution added to the catalyst ink (created separately)

to create the following relationship,

$$\begin{aligned} wt_{inkInmr} &= \frac{\text{mass of ionomer (solid-phase)}}{\text{total mass of all solid-phase constituents}} \\ &= \frac{wt_{inmr}m_{inmr}}{wt_{inmr}m_{inmr} + m_{ctlst}}, \end{aligned} \quad (C.1)$$

where $wt_{inmr}m_{inmr}$ has been used to find the total amount of solid-phase ionomer present within the ionomer solution. The wt.% ratio of alcohol to water may then be used for the following relationship,

$$wt_{alch:water} = \frac{\text{total mass of alcohol}}{\text{mass of water}} = \frac{(1 - wt_{inmr})m_{inmr} + m_{alch}}{m_{water}}, \quad (C.2)$$

where $(1 - wt_{inmr})m_{inmr}$ accounts for the alcohol present within the ionomer solution (note that this may become substantial if the solid wt.% of the ink/ionomer content is sufficiently high). Following a similar format, the ratio of PG to all liquid constituents may then be used for the following relationship,

$$\begin{aligned} wt_{PG} &= \frac{\text{mass of PG}}{\text{mass of all liquid-phase constituents}} \\ &= \frac{m_{PG}}{(1 - wt_{inmr})m_{inmr} + m_{water} + m_{alch} + m_{PG}} \end{aligned} \quad (C.3)$$

Using the wt.% of the solid-phase constituents and the total mass of the ink yields the following,

$$\begin{aligned} wt_{inkStd} &= \frac{\text{mass of solid-phase constituents}}{\text{total mass of ink}} \\ &= \frac{wt_{inmr}m_{inmr} + m_{ctlst}}{m_{inmr} + m_{ctlst} + m_{water} + m_{alch} + m_{PG}}. \end{aligned} \quad (C.4)$$

Lastly, the densities of the alcohol, water, and PG may be used to create an expression for the total volume of ink as follows,

$$\begin{aligned} V_{ink} &= \text{volume of ionomer solution} + \text{volume alcohol} + \text{volume water} + \text{volume PG} \\ &= \frac{(1 - wt_{inmr})m_{inmr} + m_{alch}}{\rho_{alch}} + \frac{m_{water}}{\rho_{water}} + \frac{m_{PG}}{\rho_{PG}}. \end{aligned} \quad (C.5)$$

Note that the above expression neglects the solid-phase content in the total volume of the ink as it is assumed negligible. Further note that the density of the solvent used for the ionomer solution and the density of the alcohol within the ink have been assumed the same.

Cross multiplying the left-hand and right-hand components of Eqs. (C.1) to (C.5) and bringing all terms related to mass to the left-hand side yields Eqs. (C.6) to (C.10)

$$wt_{inmr} (wt_{inkInmr} - 1) m_{inmr} + wt_{inkInmr} m_{ctlst} = 0 \quad (C.6)$$

$$(wt_{inmr} - 1) m_{inmr} + wt_{alch:water} m_{water} - m_{alch} = 0 \quad (C.7)$$

$$wt_{PG} (1 - wt_{inmr}) m_{inmr} + wt_{PG} m_{water} + wt_{PG} m_{alch} + (wt_{PG} - 1) m_{PG} = 0 \quad (C.8)$$

$$(wt_{inkSld} - wt_{inmr}) m_{inmr} + (wt_{inkSld} - 1) m_{ctlst} + wt_{inkSld} m_{water} + wt_{inkSld} m_{alch} + wt_{inkSld} m_{PG} = 0 \quad (C.9)$$

$$\frac{(1 - wt_{inmr}) m_{inmr}}{\rho_{alch}} + \frac{m_{water}}{\rho_{water}} + \frac{m_{alch}}{\rho_{alch}} + \frac{m_{PG}}{\rho_{PG}} = V_{ink} \quad (C.10)$$

The linear system described by Eqs. (C.6) to (C.10) may then be written in matrix form as follows,

$$\begin{bmatrix} wt_{inmr} (wt_{inkInmr} - 1) & wt_{inkInmr} & 0 & 0 & 0 \\ (wt_{inmr} - 1) & 0 & wt_{alch:water} & -1 & 0 \\ wt_{PG} (1 - wt_{inmr}) & 0 & wt_{PG} & wt_{PG} & (wt_{PG} - 1) \\ (wt_{inkSld} - wt_{inmr}) & (wt_{inkSld} - 1) & wt_{inkSld} & wt_{inkSld} & wt_{inkSld} \\ \frac{(1 - wt_{inmr})}{\rho_{alch}} & 0 & \frac{1}{\rho_{water}} & \frac{1}{\rho_{alch}} & \frac{1}{\rho_{PG}} \end{bmatrix} \begin{bmatrix} m_{inmr} \\ m_{ctlst} \\ m_{water} \\ m_{alch} \\ m_{PG} \end{bmatrix} = \begin{bmatrix} 0 \\ 0 \\ 0 \\ 0 \\ V_{ink} \end{bmatrix}$$

Finally, the system in matrix form may be solved numerically with Gaussian elimination (forward elimination followed by back substitution) [125], or by any alternative linear system solver.